



Virginia Commonwealth University  
VCU Scholars Compass

---

Theses and Dissertations

Graduate School


---

2015

## Diaza-*b*orole Linked Porous Polymers: Design, Synthesis, and Application to Gas Storage and Separation

Zafer Kahveci

Follow this and additional works at: <https://scholarscompass.vcu.edu/etd>

 Part of the [Materials Chemistry Commons](#), [Organic Chemistry Commons](#), and the [Polymer Chemistry Commons](#)

© The Author

---

Downloaded from

<https://scholarscompass.vcu.edu/etd/3916>

This Dissertation is brought to you for free and open access by the Graduate School at VCU Scholars Compass. It has been accepted for inclusion in Theses and Dissertations by an authorized administrator of VCU Scholars Compass. For more information, please contact [libcompass@vcu.edu](mailto:libcompass@vcu.edu).

© COPYRIGHT BY

**Zafer Kahveci**

**2015**

**All Rights Reserved**

# **Diaza borole Linked Porous Polymers: Design, Synthesis, and Application to Gas Storage and Separation**

A dissertation submitted in partial fulfillment of the requirements for the degree of Doctor of  
Philosophy at Virginia Commonwealth University

by

**Zafer Kahveci**

Bachelor of Science

Hacettepe University, 2008

Director: Hani M. El-Kaderi,

Associate Professor, Department of Chemistry

Virginia Commonwealth University

Richmond, Virginia

July, 2015

## **Acknowledgement**

I would like to acknowledge the continued support, encouragement and guidance of Prof. Hani El-Kaderi whose ideas and constructive recommendations helped me to make this work possible. I would also like to express my sincere appreciation for my committee members Prof. Scott Gronert, Prof. Indika U. Arachchige, and Prof. James T. McLeskey for their input in pursuit of my doctorate. I am very thankful to the members of the El-Kaderi Group whom have been a pleasure to work beside. Special thanks should be given to the Department of Chemistry at Virginia Commonwealth University; faculty, staff and people who helped me conduct my research. I would also like to thank my wonderful wife, Emine Feride Kahveci, for her encouragement and support during the rough times over the past years. She is my other half and my better half. Without her by my side, I would not be close to the man that I am today. Finally, I would like to thank my caring, loving, and supportive family and parents.

## Table of Contents

### Table of Contents

List of Tables .....	vi
List of Schemes.....	vi
List of Figures.....	vii
List of Abbreviations .....	v
Abstract.....	xiii

### Chapter 1-Introduction

1.1 Introduction.....	1
<b>1.1 Existing Technologies for CO<sub>2</sub> Separation.....</b>	<b>4</b>
1.1.1 Porous Polymers as Solid Sorbents for CO <sub>2</sub> Capture .....	7
1.1.2 Diazaborole.....	14
1.1.2.1 Synthesis of monocyclic 1, 3, 2-diazaboroles.....	17
1.1.2.2 Synthesis of 1, 3, 2-benzodiazaboroles.....	18
1.1.3 Pore Characterization of Solid Sorbents .....	21
1.4 Dissertation Problem.....	26

### Chapter 2-Targeted Synthesis of a Mesoporous Triptycene-Derived Covalent Organic Framework

2.1 Introduction .....	29
2.2 Experimental Section .....	30
2.2.1 Materials and Methods.....	30
2.2.2 Synthesis of 2, 3, 6, 7, 12, 13-hexabromotriptycene.....	31

2.2.3 Synthesis of 2, 3, 6, 7, 12, 13-hexamethoxytriptycene .....	32
2.2.4 Synthesis of 2, 3, 6, 7, 12, 13-hexahydroxytriptycene.....	33
2.2.5 Synthesis of Triptycene-Derived Covalent Organic Framework (TDCOF-5) .....	33
2.3 Results and Discussion .....	34
2.3.1 Synthesis and Characterization of TDCOF-5 .....	34
2.3.2 Porosity Studies of TDCOF-5.....	40
2.3.3 Gas Storage Studies of TDCOF-5.....	45
2.3.3.1 Calculation of Isosteric Heats of Adsorption for TDCOF-5.....	51
2.3.4 Structural Models and Atomic Coordinates for TDCOF-5.....	52
2.4. Conclusion .....	60

### Chapter 3-Synthesis and Characterization of Porous Diazaborole-Linked Polymers

3.1 Introduction.....	61
3.2 Experimental Section.....	62
3.2.1 Materials and Methods.....	62
3.1.2 Synthesis of 2, 3, 6, 7, 12, 13-hexabromotriptycene.....	64
3.1.3 Synthesis of N <sup>2</sup> ,N <sup>3</sup> ,N <sup>6</sup> ,N <sup>7</sup> ,N <sup>14</sup> ,N <sup>15</sup> Hexakis(diphenylmethylene)triptycene- 2,3,6,7,14,15 hexamine .....	65
3.1.4 Synthesis of 2, 3, 6, 7, 14, 15-Hexaaminotriptycene (HATT).....	65
3.1.5 Synthesis of DBLP-3 .....	66
3.1.6 Synthesis of DBLP-4 .....	67
3.1.7 Synthesis of DBLP-5 .....	67
3.3 Results and Discussion .....	69
3.3.1 Synthesis and Characterization of DBLPs.....	69

3.3.2 Porosity Studies of DBLPs .....	77
3.3.3 Gas Storage Studies of DBLPs .....	86
3.4 Conclusion .....	103
<b>Chapter 4-Post-synthesis modification of diazaborole-linked polymers for enhanced chemical stability and CO<sub>2</sub> capture</b>	
4.1 Introduction.....	104
4.2 Experimental Section .....	105
4.2.1 Materials and Methods.....	105
4.2.2 Synthesis of DBLP-4 .....	106
4.2.3 Synthesis of DBLP-4-F.....	107
4.3 Results and Discussion .....	108
4.3.1 Synthesis and Characterization .....	108
4.3.2 UV-VIS Studies .....	120
4.4 Conclusion .....	125
<b>Chapter 5-Concluding Remarks .....</b>	<b>126</b>
List of References .....	130
Vita.....	143

## List of Abbreviations

DBLP .....	Diaza borole-Linked Polymer
COF.....	Covalent Organic Framework
ILCOF.....	Imine-Linked Covalent Organic Framework
DFT.....	Density Functional Theory
IAST.....	Ideal Adsorbed Solution Theory
IR.....	Infrared Spectroscopy
LDA .....	Local Density Approximation
MOF.....	Metal Organic Framework
NLDFT.....	Non-Local Density Functional Theory
NMR .....	Nuclear Magnetic Resonance Spectroscopy
SEM .....	Scanning Electron Microscopy (Microscope)
XRD.....	X-Ray Diffraction



## List of Tables

<b>1.1:</b> Typical gas composition in post- and pre-combustion process.....	3
<b>2.1:</b> Fractional atomic coordinates for the refined unit cell parameters for <i>TDCOF-5</i> calculated from GSAS and EXP-GUI software packages.....	57
<b>2.2:</b> Fractional atomic coordinates for the staggered conformation of <i>TDCOF-5</i> calculated from <i>Materials Studio</i> modeling.....	58
<b>2.3:</b> Fractional atomic coordinates for the eclipsed conformation of <i>TDCOF-5</i> calculated from <i>Materials Studio</i> modeling.....	59
<b>3.1:</b> Gas uptakes of most known boron containing porous polymers.....	99
<b>3.2:</b> Gas Uptake and Selectivity (CO <sub>2</sub> /N <sub>2</sub> and CO <sub>2</sub> /CH <sub>4</sub> ) for DBLPs.....	100

## List of Schemes

<b>1.1:</b> Syntheses of monocyclic 1, 3, 2-benzodiazaboroles .....	18
<b>1.2:</b> Syntheses of 1, 3, 2-benzodiazaboroles by cyclocondensation and by organo/bromine exchange .....	19
<b>1.3:</b> Examples of 1, 3, 2-benzodiazaboroles synthesized by using organolithiums. Compound 1 is described in Scheme 1.2 .....	19
<b>1.4:</b> Syntheses of 1, 3, 2-benzodiazaboroles by condensation reaction.....	20
<b>3.1:</b> Overall synthesis of hexahydroxytryptcene and hexaaminotriptycene (HCl salt) .....	64
<b>3.2:</b> Synthesis of DBLP-3, DBLP-4, and DBLP-5 .....	68
<b>4.1:</b> Synthetic route for DBLP-4.....	109
<b>4.2:</b> Synthetic route for DBLP-4-F .....	110

## List of Figures

<b>1.1:</b> Materials for CO <sub>2</sub> capture.....	4
<b>1.2:</b> Examples of building units used in the construction of inorganic/hybrid/organic materials ...	7
<b>1.3:</b> Components of coordination polymers and possible structural frameworks that can be constructed by using different combinations .....	8
<b>1.4:</b> Representation of a typical MOF and POP.....	10
<b>1.5:</b> Schematic illustrations of the error correction step.....	11
<b>1.6:</b> Formation of the COFs .....	12
<b>1.7:</b> General synthetic method of the reported BILP-2.....	13
<b>1.8:</b> Boronate-ester, imidazole, and diazaborole building blocks.....	15
<b>1.9:</b> Borazine moiety.....	16
<b>1.10:</b> Synthesis of BLP-1(H) and BLP-12(H) from in situ thermal decomposition of arylamine-borane adducts .....	17
<b>1.11:</b> Six types of isotherms as identified by Brunauer-Emmett-Teller and Sing. Blue line is adsorption and red desorption.....	22
<b>1.12:</b> Formation of monolayer (Langmuir) and multilayer (BET) theory .....	24
<b>2.1:</b> FT-IR spectra were obtained as KBr pellets using a Nicolet Nexus 670 FT-IR spectrometer. The formation of the BC <sub>2</sub> O <sub>2</sub> ring is supported by the following IR-bands (cm <sup>-1</sup> ): B-O (1352), B-C (1270), and C-O (1024). FT-IR results are in line with previous reported COFs.....	36
<b>2.2:</b> Solid-state <sup>11</sup> B multiple quantum MAS (MQMAS) NMR spectrum of TDCOF-5; asterisks denote spinning-side bands .....	37
<b>2.3:</b> TGA for an activated sample of TDCOF-5 .....	37
<b>2.4:</b> Solid-State <sup>13</sup> C CP-MAS NMR spectrum for TDCOF-5 .....	38

<b>2.5:</b> SEM images of as-prepared TDCOF-5 .....	39
<b>2.6:</b> Argon adsorption isotherm for TDCOF-5 measured at 87 K. The filled circles are adsorption points and the empty circles are desorption points .....	40
<b>2.7:</b> Experimental Ar adsorption isotherm for TDCOF-5 measured at 87 K is shown as filled circle. The calculated NLDFT isotherm is overlaid as open circle. Note that a fitting error of less than 1% indicates the validity of using this method for assessing the porosity of TDCOF-5. The fitting error is indicated. ....	41
<b>2.8:</b> Langmuir plot for TDCOF-5 calculated from the Ar adsorption isotherm at 87 K. The model was applied from $P/P_0=0.17-0.30$ . The correlation factor is indicated. (W= Weight of gas absorbed at a relative pressure $P/P_0$ ).....	42
<b>2.9:</b> BET plot for TDCOF-5 calculated from the Ar adsorption isotherm at 87 K. The model was applied from $P/P_0=0.05-0.15$ . The correlation factor is indicated. (W= Weight of gas absorbed at a relative pressure $P/P_0$ ).....	43
<b>2.10:</b> Pore Size Distribution (PSD) for TDCOF-5 using the NLDFT model .....	44
<b>2.11: A)</b> Hydrogen isotherm for <i>TDCOF-5</i> measured at 77K and 87K. <b>B)</b> Hydrogen isosteric heat of adsorption ( $Q_{st}$ ) for TDCOF-5 .....	46
<b>2.12: A)</b> Methane isotherm for <i>TDCOF-5</i> measured at 273K and 298K. <b>B)</b> Methane isosteric heat of adsorption ( $Q_{st}$ ) for TDCOF-5 .....	47
<b>2.13: A)</b> Carbon dioxide isotherm for <i>TDCOF-5</i> measured at 273K and 298K. <b>B)</b> Carbon dioxide isosteric heat of adsorption ( $Q_{st}$ ) for <i>TDCOF-5</i> .....	48
<b>2.14: A)</b> Virial analysis of H <sub>2</sub> adsorption data for <i>TDCOF-5</i> . <b>B)</b> Combined isosteric heat of adsorption ( $Q_{st}$ ) for <i>TDCOF-5</i> .....	49

<b>2.14: A)</b> Virial analysis of H <sub>2</sub> adsorption data for <i>TDCOF-5</i> . <b>B)</b> Combined isosteric heat of adsorption ( <i>Q<sub>st</sub></i> ) for <i>TDCOF-5</i> .....	50
<b>2.16:</b> PXRD pattern of <i>TDCOF-5</i> with the experimental pattern in black, the Reitveld refined profile in red, the difference plot in blue and the eclipsed crystal model is green .....	54
<b>2.17:</b> Eclipsed PXRD pattern of <i>TDCOF-5</i> .....	55
<b>2.18:</b> Staggered PXRD pattern of <i>TDCOF-5</i> .....	56
<b>3.1:</b> FT-IR spectra of DBLPs and their starting building units. Lower panel is an expanded region from 600 to 1800 cm <sup>-1</sup> .....	70
<b>3.2:</b> SEM images of <b>A)</b> DBLP-3, <b>B)</b> DBLP-4, and <b>C)</b> DBLP-5.....	71
<b>3.3:</b> Solid state and <sup>11</sup> B MAS NMR spectra of DBLPs .....	73
<b>3.4:</b> Thermogravimetric analysis of DBLPs .....	73
<b>3.5:</b> Solid state <sup>13</sup> C CP-MAS of DBLP 3-4 .....	73
<b>3.6:</b> Solid state <sup>13</sup> C CP-MAS of DBLP-5 .....	74
<b>3.7:</b> XRD-patterns for the DBLPs. Broad peak at around 2θ = 15 indicates the amorphous characteristics of DBLPs.....	74
<b>3.8:</b> Ar adsorption isotherm for DBLP-3 (black), DBLP-4 (blue) and DBLP-5 (red) measured at 87 K. The filled markers are adsorption points and the empty markers are desorption points. ....	75
<b>3.9:</b> Experimental Ar adsorption isotherm for, DBLP-3 (black) measured at 87 K. The calculated NLDFT isotherm is overlaid as open circle. Note that a fitting error of < 1 % indicates the validity of using this method for assessing the porosity of DBLPs. The fitting error is indicated.....	76
<b>3.10:</b> Experimental Ar adsorption isotherm for DBLP-4 (blue) measured at 87 K. The calculated NLDFT isotherm is overlaid as open circle. Note that a fitting error of < 1 % indicates the validity of using this method for assessing the porosity of DBLPs. The fitting error is indicated.....	78

<b>3.11:</b> Experimental Ar adsorption isotherm for DBLP-5 (red) measured at 87 K. The calculated NLDFT isotherm is overlaid as open circle. Note that a fitting error of < 1 % indicates the validity of using this method for assessing the porosity of DBLPs. The fitting error is indicated.....	79
<b>3.12:</b> Pore Size Distribution for DBLP-3 (black) and DBLP-4 (blue) was calculated from the Ar adsorption isotherms by the Non-Local Density Functional Theory (NLDFT) method using a cylindrical pore model. ....	81
<b>3.13:</b> Pore Size Distribution for DBLP-5 (red) was calculated from the Ar adsorption isotherms by the Non-Local Density Functional Theory (NLDFT) method using a cylindrical pore model .....	82
<b>3.14:</b> BET plot for DBLP-3 (black), and DBLP-4 (blue) calculated from the Ar adsorption isotherm at 87 K. The model was applied from $P/P_0= 0.04-0.16$ . The correlation factor is indicated. (W= Weight of gas absorbed at a relative pressure $P/P_0$ ). ....	83
<b>3.15:</b> BET plot for DBLP-5 (red) calculated from the Ar adsorption isotherm at 87 K. The model was applied from $P/P_0= 0.04-0.16$ . The correlation factor is indicated. (W= Weight of gas absorbed at a relative pressure $P/P_0$ ).....	84
<b>3.16:</b> <b>A)</b> Crystal packing, <b>B)</b> the hydrogen-bonding network, and <b>C)</b> overlapping modes.....	86
<b>3.17:</b> CO <sub>2</sub> uptake isotherms for DBLP-3, DBLP-4 and DBLP-5 at 273 and 298 K.....	87
<b>3.18:</b> H <sub>2</sub> uptake isotherms for DBLP-3, DBLP-4 and DBLP-5 at 77 and 87 K .....	88
<b>3.19:</b> CH <sub>4</sub> uptake isotherms for DBLP-3, DBLP-4 and DBLP-5 at 273 and 298 K.....	89
<b>3.20:</b> Virial analysis of CO <sub>2</sub> adsorption data for DBLP-3, and DBLP-4.....	90
<b>3.21:</b> Virial analysis of CO <sub>2</sub> adsorption data for DBLP-5 and the isosteric heat of adsorption ( $Q_{st}$ ) for DBLP-3, DBLP-4, and DBLP-5. ....	91
<b>3.22:</b> Virial analysis of H <sub>2</sub> adsorption data for DBLP-3, and DBLP-4. ....	92

<b>3.23:</b> Virial analysis of H <sub>2</sub> adsorption data for DBLP-5 and the isosteric heat of adsorption ( $Q_{st}$ ) for DBLP-3, DBLP-4, and DBLP-5. ....	93
<b>3.24:</b> Virial analysis of CH <sub>4</sub> adsorption data for DBLP-3, and DBLP-4.....	94
<b>3.25:</b> Virial analysis of CH <sub>4</sub> adsorption data for DBLP-5 and the isosteric heat of adsorption ( $Q_{st}$ ) for DBLP-3, DBLP-4, and DBLP-5. ....	95
<b>3.26:</b> Gas sorption capacities for DBLP-3 at 298 K. CO <sub>2</sub> (black squares), CH <sub>4</sub> (red circles) and N <sub>2</sub> (green triangle).....	97
<b>3.27:</b> Gas sorption capacities for DBLP-4, and DBLP-5 at 298 K. CO <sub>2</sub> (black squares), CH <sub>4</sub> (red circles) and N <sub>2</sub> (green triangle). ....	100
<b>3.28:</b> Adsorption selectivity of CO <sub>2</sub> over N <sub>2</sub> and CH <sub>4</sub> for DBLP-3 from initial slope calculations. CO <sub>2</sub> (black), CH <sub>4</sub> (red) and N <sub>2</sub> (blue) isotherms collected at and 298 K. ....	101
<b>3.29:</b> Adsorption selectivity of CO <sub>2</sub> over N <sub>2</sub> and CH <sub>4</sub> for DBLP-4 from initial slope calculations. CO <sub>2</sub> (black), CH <sub>4</sub> (red) and N <sub>2</sub> (blue) isotherms collected at and 298 K. ....	102
<b>3.30:</b> Adsorption selectivity of CO <sub>2</sub> over N <sub>2</sub> and CH <sub>4</sub> for DBLP-5 from initial slope calculations. CO <sub>2</sub> (black), CH <sub>4</sub> (red) and N <sub>2</sub> (blue) isotherms collected at and 298 K. ....	103
<b>4.1:</b> Solid-State <sup>13</sup> C CP-MAS NMR spectrum for DBLP-4. ....	110
<b>4.2:</b> FT-IR spectrum for DBLP-4, BTPA and HATT.....	111
<b>4.3:</b> Solid-state <sup>11</sup> B multiple quantum MAS (MQMAS) NMR spectrum of DBLP-4 and DBLP-4-F; asterisks denote spinning-side bands.....	112
<b>4.4:</b> Scanning Electron Microscopy (SEM) Imaging of DBLP-4.....	113
<b>4.5:</b> Powder X-ray Diffraction Analysis of DBLP-4: Powder X-ray diffraction data of DBLP-4 were collected on a Panalytical X'pert Pro Multipurpose Diffractometer (MPD). Samples were	

mounted on a zero background sample holder measured in transmission mode using Cu K $\alpha$ radiation with a 2 $\theta$ range of 1.5-35 $^{\circ}$ . .....	114
<b>4.6:</b> Argon isotherm for DBLP-4 measured at 87 K. The filled squares are adsorption points and the empty squares are desorption points.....	117
<b>4.7:</b> Pore Size Distribution (PSD) for DBLP-4 from NLDFT.....	117
<b>4.7:</b> NLDFT calculated isotherm for DBLP-4 overlaid with the experimental argon isotherm. A fitting error less than 1% indicates validity of the model. ....	118
<b>4.8:</b> Multipoint BET plot for DBLP-4 calculated from the argon adsorption .....	118
<b>4.9:</b> CO $_2$ isotherms for DBLP-4-F as synthesized, 24 h and 48 h exposed to air at 273K. The filled points are adsorption and the empty points are desorption. ....	119
<b>4.10:</b> Multipoint BET plots for DBLP-4-F as synthesized calculated with CO $_2$ at 273K .....	119
<b>4.11:</b> Multipoint BET plots for DBLP-4-F, which are 24 h and 48 h exposed to air that are calculated from the CO $_2$ adsorption.....	120
<b>4.12:</b> Fluorescence enhancement of the DBLP-4 polymer upon the incremental addition of the 10 $^{-2}$ M fluoride anion in dimethylformamide. ....	122
<b>4.13:</b> Excitation Properties of BTPA, HATT, DBLP-4 and Self-Condensed BTPA in DMF. ...	123
<b>4.14:</b> Emission Properties of BTPA, HATT, DBLP-4 and Self-Condensed BTPA in DMF .....	124
<b>4.15:</b> Photobleaching experiment of DBLP-4 polymer in dimethylformamide upon exposure to UV light for 40 minutes. ....	125

## Abstract

# **DIAZABOROLE LINKED POROUS POLYMERS: DESIGN, SYNTHESIS, AND APPLICATION TO GAS STORAGE AND SEPARATION**

By Zafer Kahveci, Ph.D.

A dissertation submitted in partial fulfillment of the requirements for the degree of Doctor of Philosophy at Virginia Commonwealth University.

Virginia Commonwealth University, 2015

Director: Hani M. El-Kaderi, Associate Professor, Department of Chemistry

The synthesis of highly porous organic polymers with predefined porosity has attracted considerable attention due to their potential in a wide range of applications. Porous organic polymers (POPs) offer novel properties such as permanent porosity, adjustable chemical nature, and noteworthy thermal and chemical stability. These remarkable properties of the POPs make them promising candidates for use in gas separation and storage. The emission of carbon dioxide (CO<sub>2</sub>) from fossil fuel combustion is a major cause of global warming. Finding an efficient separation and/or storage material is essential for creating a cleaner environment. Therefore, the importance of the POPs in the field is undeniable. Along these pursuits, several porous polymers have been synthesized with different specifications. The first class of porous polymers are called Covalent Organic Frameworks (COFs). They possess highly ordered structures with very high surface areas and contain light elements. COFs based on B-O, C-N, and B-N bonds have been reported so far. In particular, COFs based on B-O bond formation are well investigated due to the kinetically labile nature of this bond which is essential for overcoming the crystallization problem



of covalent networks. Along this line, triptycene-derived covalent organic framework (TDCOF-5) has been synthesized through a condensation reaction between 1, 4-benzenediboronic acid and hexahydroxytriptycene which leads to the formation of boronate ester linkage. TDCOF-5 has the highest H<sub>2</sub> uptake under 1 atm at 77K (1.6%) among all known 2D and 3D COFs derived from B–O bond formation and moderate CO<sub>2</sub> uptake (2.1 mmol g<sup>-1</sup>) with  $Q_{st}$  values of 6.6 kJ mol<sup>-1</sup> and 21.8 kJ mol<sup>-1</sup>, respectively.

The second class of porous structures discussed herein is diazaborole linked polymers (DBLPs). They are constructed based on B-N bond formation and possess amorphous structures due to the lack of the reversible bond formation processes. At this scope, 2, 3, 6, 7, 14, 15-hexaamino triptycene (HATT) hexahydrochloride was synthesized and reacted with different boronic acid derivatives to produce three different porous polymers under condensation reaction conditions. DBLP-3, -4 and -5 have very high surface areas; 730, 904, and 986 m<sup>2</sup> g<sup>-1</sup>, and offer high CO<sub>2</sub> uptake (158.5, 198, and 171.5 mg g<sup>-1</sup>) at 1 bar and 273 K, respectively. DBLPs have much higher CO<sub>2</sub> uptake capacity when compared to almost all reported B-N and B-O containing porous polymers in the field. In addition to high CO<sub>2</sub> capacity, DBLPs showed remarkable CO<sub>2</sub>/N<sub>2</sub> and CO<sub>2</sub>/CH<sub>4</sub> selectivity, when the Henry's law of initial slope selectivity calculations were applied. In general, DBLPs exhibit high selectivities for CO<sub>2</sub>/N<sub>2</sub> (35-51) and CO<sub>2</sub>/CH<sub>4</sub> (5-6) at 298 K which are comparable to those of most porous polymers.

## Chapter 1

### Introduction

Global warming and climate change originating from increasing atmospheric carbon dioxide emissions are considered to be one of the most pressing environmental issues of the 21<sup>st</sup> century.<sup>12-16</sup> Since the onset of the Industrial Revolution, large scale uses of fossil fuels have continued to rise, and since then carbon dioxide concentration in the atmosphere has seen a dramatic increase. The major source of carbon dioxide emissions, which mainly comes from the combustion of coal, oil, and natural gas (80% of CO<sub>2</sub> emissions),<sup>17</sup> are expected to continue to increase, and this will be particularly evident in developing countries. Fossil fuels currently provide 87% of the world's energy and it is projected that usage will increase to about 18 billion tonne oil equivalents by 2035. A significant increase to the amount of approximately 12 billion in 2009.<sup>18</sup> The first international agreement on the emissions of the greenhouse gases (GHGs) is the Kyoto Protocol in which countries agreed to reduce the GHGs in the period of 2008-2012 by 5.2% on average, however, the results did not meet the expectations as of the 2011 Durban COP meeting leading to the protocol's extension until 2017. On the other hand, at the current rate of the consumption of the energy, coal will run out in 130 years, natural gas in 60 years, and oil in 42 years according to the estimates by the World Coal Institute.<sup>19</sup> To overcome these high carbon dioxide emissions and to solve the energy need issue, there has been great interest in finding renewable and clean alternative energy sources.

Reducing fossil fuel consumption gradually by replacement with solar, wind, geothermal, hydroelectric and hydrogen sources is one approach. Among these, hydrogen is the most promising energy source for transportation applications due to its high energy density in comparison with fossil fuels. Most importantly, hydrogen generates only energy and water as byproducts.<sup>15, 16, 20</sup>

However, there are challenges to hydrogen use such as low density and flammability. These challenges must be overcome by high performance storage systems.<sup>21</sup> To be considered useful, hydrogen needs to be stored at least at 40 g L<sup>-1</sup> volumetrically and 5.5 wt.% gravimetrically according to the U.S. Department of Energy (DOE) 2015 targets under the operation 40 to 60 °C and delivery pressure of 100 atm.<sup>22</sup> However, conventional methods for hydrogen storage such as high-pressure and cryogenic tanks are costly and relatively unsafe for transportation. Extensive efforts have been made to store hydrogen efficiently by using metal hydrides and chemical hydrides. Yet hydrides are poor candidates for practical hydrogen storage applications due to the irreversible nature of their hydrogen storage, high thermodynamics, slow kinetics and high weight. As such, it is necessary to develop new materials that can overcome the irreversibility of current hydrogen uptake methods and efficiently store hydrogen safely in an economically feasible way. Hydrogen storage by porous materials has undergone intensive research in the last two decades, due to the benefits of their reversible hydrogen uptake/release and highly stable nature.

Power generation facilities are the major contributor of CO<sub>2</sub> emissions among industrial sources and there are many approaches to reduce these emissions, including switching to alternative carbon-free or low-carbon fuels. However, despite a clear and present need for this switch, fossil fuels (especially coal and natural gas) have been the dominant energy source for decades. In light of this, carbon capture and storage (CCS) is the most important technology to separate and store released CO<sub>2</sub> from fossil fuels sources. CCS allows the use of fossil fuels while minimizing the release of CO<sub>2</sub> to the atmosphere by separating CO<sub>2</sub> from flue gas. Furthermore, separated CO<sub>2</sub> can be used in enhanced oil recovery (EOR) in which CO<sub>2</sub> is pumped into the oil reservoir to increase the mobility of oil.<sup>23</sup> There are three main technologies for capturing the CO<sub>2</sub>

Composition	Post-combustion	Pre-combustion
N <sub>2</sub>	70-75%	0.25%
CO <sub>2</sub>	15-16%	35.5%
H <sub>2</sub> O	5-7%	0.2%
O <sub>2</sub>	3-4%	-
H <sub>2</sub>	-	61.5%
SO <sub>x</sub>	< 800 ppm	-
NO <sub>x</sub>	500 ppm	-
H <sub>2</sub> S	100 ppm	1.1%

**Table 1.1:** Typical gas composition in post-combustion and pre-combustion processes.

from power plants: pre-combustion, post-combustion, and oxyfuel combustion. (i) In pre-combustion systems, as the name implies, CO<sub>2</sub> is removed prior to combustion among other gaseous and solid components (Table 1.1).<sup>24, 25</sup> Fossil fuels are first converted to syngas, which has mainly CO and H<sub>2</sub>, CO can undergo a water-gas shift reaction that will convert the CO to CO<sub>2</sub> and H<sub>2</sub>. The CO<sub>2</sub> is then removed from the system using storage techniques while H<sub>2</sub> can be used as other energy source such as fuel cells.<sup>26-28</sup> The high CO<sub>2</sub> content high-pressure syngas stream advantageous for the using existing solvent and capture technology. (ii) Oxyfuel combustion is based on the purification of the O<sub>2</sub> from air, making the output gas consisting mainly of CO<sub>2</sub> and water vapor, which can be easily separated by condensation. The main advantage of this process is that the output after the combustion is pure CO<sub>2</sub> and there is no need for separation steps for resulting gas mixtures. However, purifying O<sub>2</sub> from air is uneconomical hence making this method unfeasible.<sup>29, 30</sup> (iii) In post-combustion, CO<sub>2</sub> is removed selectively after the combustion of fossil fuels from flue gas, which includes mainly CO<sub>2</sub> (15-16%) and N<sub>2</sub> (70-75%) with other impurities

(Table 1.1), under atmospheric pressure. This technology is currently the benchmark method, due to its effectiveness and compatibility with existing power plants.

### 1.1 Existing Technologies for CO<sub>2</sub> Separation

It is important to pursue efficient and suitable technologies for CO<sub>2</sub> separation in order to achieve low cost energy consumption. Several methods and materials have been investigated for postcombustion capture up to date including: (a) absorption, (b) adsorption, (c) cryogenic distillation, and (d) membrane separation, as well as, most novel methods electrochemical pumps and chemical looping (Figure 1.1).<sup>23</sup> In adsorption technology, flue gas is dissolved in a liquid adsorbent. The CO<sub>2</sub> rich solvent is fed through the heater to increase the temperature to induce the release of CO<sub>2</sub>, a process called “stripping”, the hot CO<sub>2</sub> is then compressed and fed into the absorber column for CO<sub>2</sub> cooling and recycling. Among the most studied solvent systems are amine

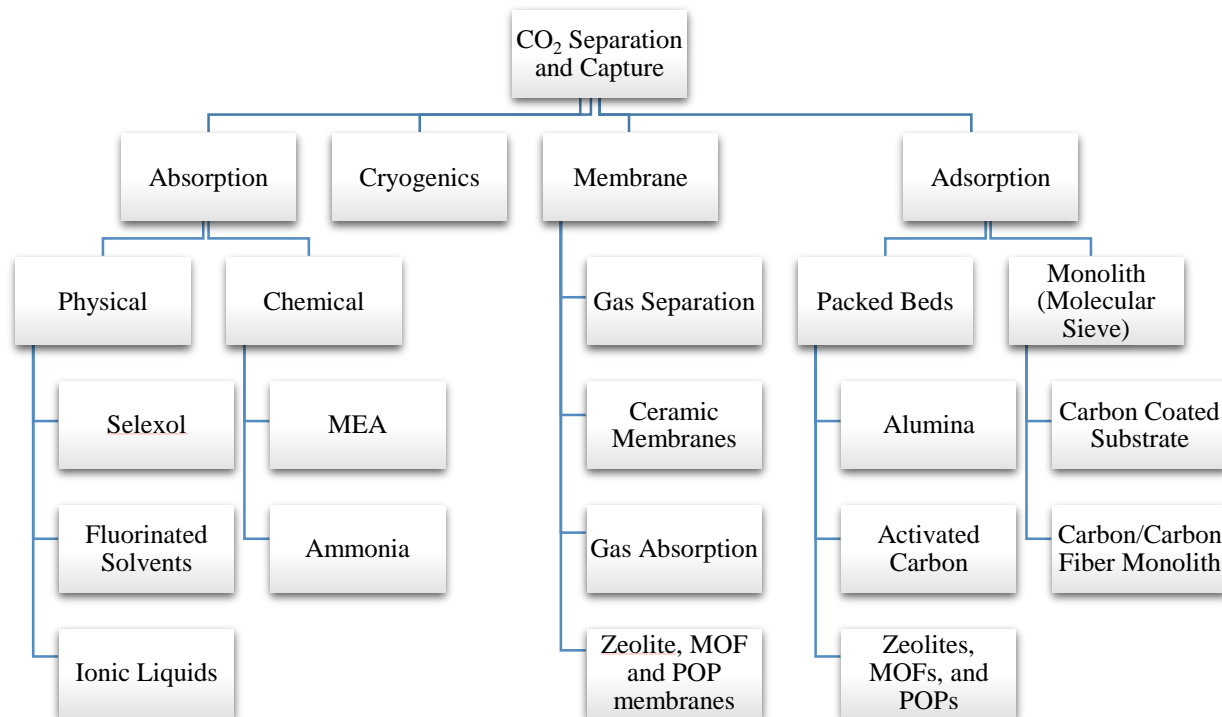


Figure 1.1: Materials for CO<sub>2</sub> capture

scrubbing solutions. Amine scrubbing consists of primary or secondary alkylamine (aqueous solutions of 20-30% monoethanolamine, or MEA are benchmark amine systems) which can reversibly react with CO<sub>2</sub>. Although amine scrubbing is widely used, the major drawback of this process remains the regeneration step, which is energy intensive. Generally 20-30% of the power plant's energy output is needed for solvent regeneration,<sup>30</sup> other concerns include the corrosive and toxic nature of liquid amines which suffer from decomposition and volatility.

In the adsorption process, CO<sub>2</sub> molecules are separated based on their selective interaction with adsorbent walls either physically or chemically. To achieve this goal, solid adsorbents must have high selectivity, high adsorption capacity and suitable adsorption-desorption kinetics as well as thermal and chemical stability after adequate cycles. There are two main solid adsorbents; physical and chemical. In chemical adsorption (chemisorption), CO<sub>2</sub> molecules react with the adsorbent through a chemical reaction in a reversible manner. For instance, metal oxides (such as CaO) react with CO<sub>2</sub> reversibly at high temperatures, 923 K, to produce carbonates (CaCO<sub>3</sub>), and these are then fed in the carbonation reactor at 1123 K to recover the concentrated stream of CO<sub>2</sub>. Chemical adsorbents suffer from high regeneration cost that limits their usage. Unlike chemisorption, physical adsorption (physisorption) involves the capture of CO<sub>2</sub> on the surface of the adsorbent through weak physical interactions such as Van der Waals and Columbic forces. The reversibility of weak interactions allows the storage and release to be more energetically favorable. These kinds of physisorbants generally have lower heat of adsorption of CO<sub>2</sub>, it requires 20-30% less adsorption energy than optimum aqueous MEA, which is a remarkable advantage because they need low energy for regeneration. With this consideration in mind, porous materials such as zeolites, metal organic frameworks (MOFs), ZIFs, activated carbon and porous organic polymers (POPs) are promising candidates for capturing CO<sub>2</sub> from the flue gas.<sup>31</sup> Zeolites are one of the

porous materials which are applied for CO<sub>2</sub> capture, however, it has some disadvantages such as very low CO<sub>2</sub> storage capacity, active life of the adsorbent is less than 10 cycles, due to the low stability of zeolite structure, and the large scale synthesis of zeolites is costly as well.<sup>32</sup> Activated carbon is another porous material for CO<sub>2</sub> capture, but they have lower CO<sub>2</sub> capacities than zeolites under ambient pressure due to non-functionalized pores, which lead to their lower binding affinity<sup>32</sup>. Other than zeolites and activated carbon, metal organic frameworks (MOFs)<sup>33</sup> and porous organic polymers (POPs) are also investigated as a potential CO<sub>2</sub> adsorbents. MOFs have great potential for use as CO<sub>2</sub> adsorbents due to their high microporosity and adjustable pore functionality, but currently most MOFs suffer from stability issues upon air and moisture exposure due to weak coordination bonds between ligand and metal sites.<sup>33</sup> Porous organic polymers are promising candidates to use in gas storage applications because of their very high surface area, high chemical and thermal stability, and high microporosity.<sup>34,35</sup> POPs are made of purely organic building blocks (consist of light elements B, C, N, and O) linked by covalent bonds.<sup>36</sup> Engineering pores for size, shape and functionality gives the ability to selectively capture a targeted gas by selecting a variety of organic building blocks. Covalent organic frameworks (COFs),<sup>37</sup> hyper-crosslinked polymers (HCPs)<sup>38</sup>, conjugated microporous polymers (CMPs)<sup>39</sup> and polymers of intrinsic microporosity (PIMs) are the examples of porous organic polymers. COFs have shown remarkable capacities for H<sub>2</sub>, CO<sub>2</sub> and CH<sub>4</sub> gas storage especially at high-pressure settings as well as selective uptake of those gasses.<sup>33</sup> The amount of CO<sub>2</sub> captured by POPs directly depends on the pore functionality, surface area, and pore size<sup>40</sup>. Therefore, there has been a growing focus for the extensive study to design new POPs which has the high surface area, stability and proper pore size and functional groups for the selective capture of CO<sub>2</sub>. The CO<sub>2</sub> uptakes of some well-known POPs at atmospheric pressure and at 273 K include, COFs (1.3-3.8 mmol g<sup>-1</sup>), BPL carbon (3.3

mmol g<sup>-1</sup>), carbazole-based porous organic polymers CPOPs (4.82 mmol g<sup>-1</sup>), triptycene-based microporous poly-(benzimidazole) networks TBIs (2.7–3.9 mmol g<sup>-1</sup>)<sup>41,42</sup> and –OH functionalized porous organic frameworks (POFs, 4.2 mmol g<sup>-1</sup>).<sup>15</sup>

### 1.1.1 Porous Polymers as Solid Sorbents for CO<sub>2</sub> Capture

Synthesis and characterization of 1D, 2D, and 3D infinite molecular inorganic-organic hybrid materials have been intensively studied (Figure 1.2).<sup>10</sup> Connectors and linkers are two

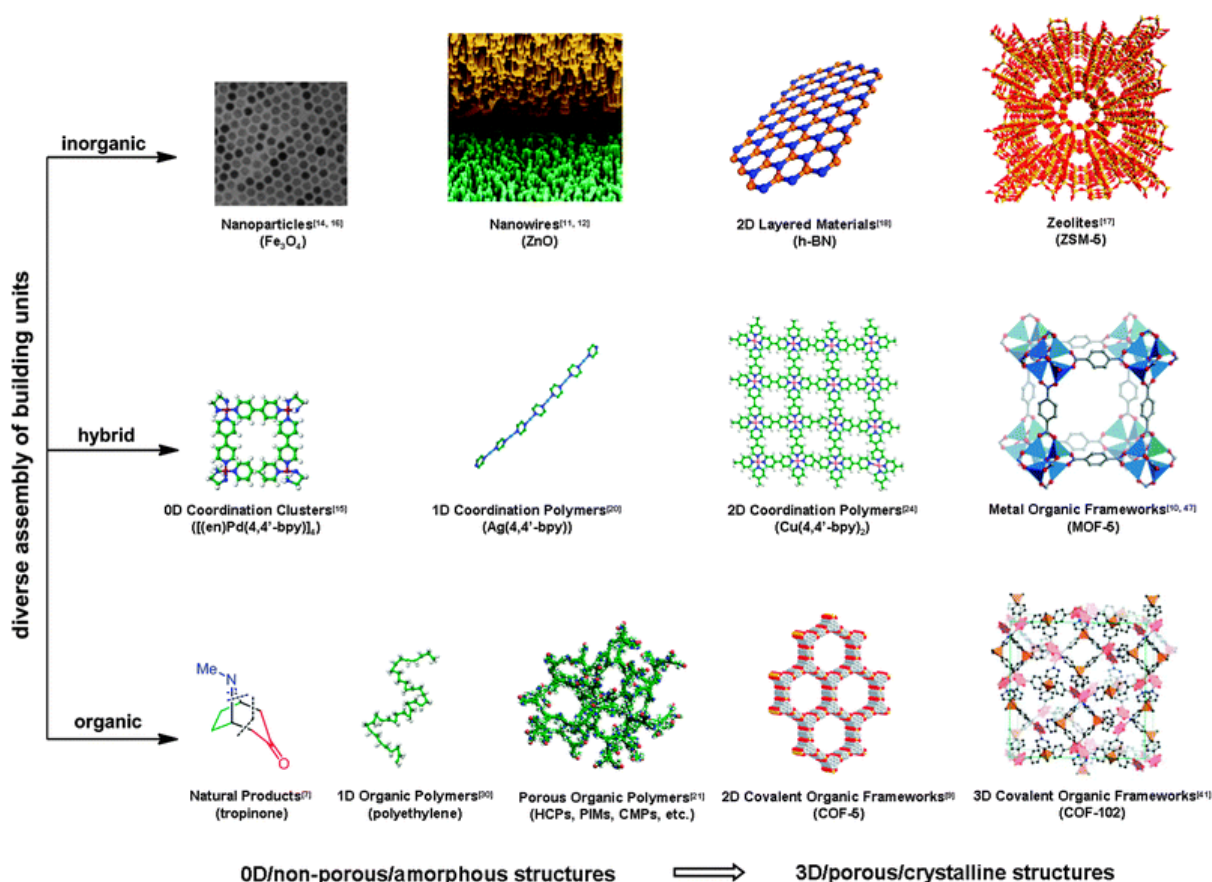


**Figure 1.2:** Examples of building units used in the construction of inorganic/hybrid/organic materials. Adapted from Ref. 5 with permission from The Royal Society of Chemistry.



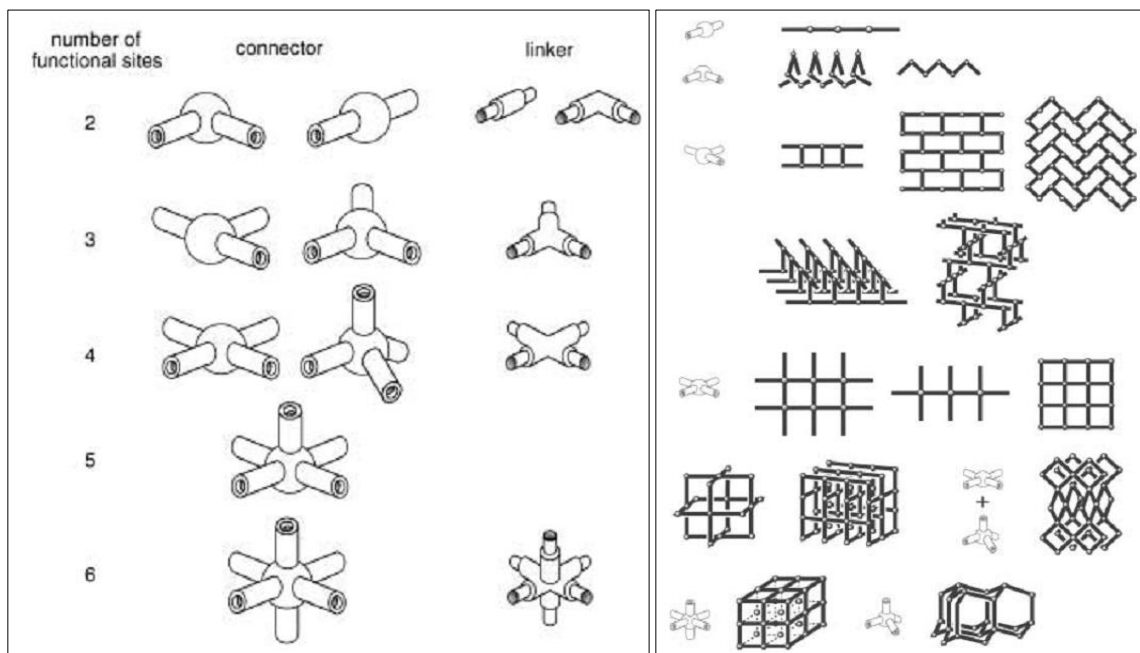


**Figure 1.3:** Components of coordination polymers and possible structural frameworks that can be constructed by using different combinations. Adapted from Ref. 10 with permission from John Wiley and Sons and Copyright Clearance Center.

main components of coordination polymers. Depending on the number of the binding sites or coordination geometries of the molecules, resulting polymers could be one-, two-, or three-dimensional (Figure 1.3). The choice of certain combination of discrete molecules leads to desired pore size, functionality and structural shape of the infinite network, thus, this is called bottom-up method. Due to the large number of the different sizes, geometry and functionality of the possible networks, there are no boundaries for the coordination polymers synthesis, which can offer various desired properties. Porous materials are typically categorized by the pore diameter; macropores (greater than 500 Å), mesopores (in between 500 Å and 20 Å) and micropores (smaller than 20 Å). In addition, porous materials can be divided into two main categories: (1) crystalline and (2) amorphous materials, according to their solid-state structure. Unlike the amorphous materials, crystalline materials have well-ordered solid pattern, uniform morphology and generally offer

wider pore sizes.

Solid adsorbents, either packed or fluidized adsorbent beds, have significant advantages for energy efficiency. CO<sub>2</sub> adsorption occurs on the surface of the solid materials which is recycled in the later stages of the process using pressure, vacuum, or temperature swing adsorption cycles. A variety of microporous and mesoporous materials have been considered for CO<sub>2</sub> capture. Such as zeolites, metal organic frameworks (MOFs), zeolitic imidazole frameworks (ZIFs), activated carbon and porous organic polymers (POPs).<sup>31</sup>

Zeolites are porous aluminosilicate materials, which possess a high thermal and chemical stability, are most widely applied for CO<sub>2</sub> capture. Zeolite 13X is one example which has promising CO<sub>2</sub> capture capacity at room temperature (16.4 wt.% at 0.8 bar and 298 K).<sup>43</sup> However, many of the zeolites can be easily saturated with water vapor which is present in the flue gas, as a result of CO<sub>2</sub> capture capacity significantly decreasing over time. The regeneration temperature for zeolites is very high (300 °C) and recovery cost is a significant disadvantage along with the low CO<sub>2</sub> storage capacity. Additionally, the active life of the adsorbent is less than 10 cycles, and its synthesis on a large scale is costly.<sup>32</sup> Other porous materials such as carbon species represent another option for CO<sub>2</sub> capture. They are highly porous carbonaceous materials which can be produced by pyrolysis from carbon rich materials, such as resins or biomass.<sup>43</sup> They have non-functional pores which leads to uniform electric potential on the surfaces and, thus they have lower CO<sub>2</sub> affinity, and hence lower CO<sub>2</sub> capacities compared to zeolites. However, they are inexpensive and insensitive to moisture unlike zeolites.<sup>32</sup> The most significant advantage of porous carbon species over zeolites is that their hydrophobicity makes their CO<sub>2</sub> capture properties less sensitive to water and they do not decompose under water vapor. In addition to water stability, since carbon species have lower heats of adsorption for CO<sub>2</sub>, they offer lower regeneration energies.<sup>44</sup>

Other than zeolites and activated carbon, metal organic frameworks (MOFs)<sup>33</sup> and porous organic polymers (POPs) have also been investigated as a potential CO<sub>2</sub> adsorbents. In the past 25 years, there have been significant advancements in synthesis and characterization of MOFs. MOFs are microcrystalline solids composed of organic bridging ligands and metal ions into an extended porous network structure (Figure 1.4).<sup>45</sup> They have unique properties such as, robustness, high thermal and chemical stabilities, very high surface areas up to 6000 m<sup>2</sup>/g)<sup>37</sup>, and low densities. MOFs have great potential in use as a CO<sub>2</sub> adsorbent due to their high microporosity and adjustable pore functionality. MOFs, in general, exhibit high CO<sub>2</sub> capacities at high pressures. To give an example; the benchmark material zeolite 13X adsorbs 7.4 mmol g<sup>-1</sup> CO<sub>2</sub> at 32 bar, while MOF-177 exhibits up to 33.5 mmol g<sup>-1</sup> at 32 bar.<sup>24</sup> Yet, currently most MOF structures suffer from stability issues upon air and moisture exposure due to the weak coordination bonds between ligand and metal sites.<sup>33</sup>



**Figure 1.4:** Representation of a typical MOF and POP. Adapted from Ref. 6 with permission from The Royal Society of Chemistry.

Porous organic polymers are promising candidates for use in gas storage applications because of their very high surface area, high chemical and thermal stability, and high microporosity.<sup>34,35</sup> POPs are made of purely organic building blocks (consist of light elements B, C, N, and O) linked by strong covalent bonds (Figure 1.4).<sup>36</sup> Engineering pores for size, shape and functionality gives the ability to selectively design for the target gas via the selection of a variety of organic building blocks. The synthesis of POPs can be carried out by using several methods such as Yamamoto coupling, Sonogashira cross-coupling, Suzuki coupling, imidazole ring formation, Friedel-Craft, Schiff-base formation, and cyclotrimerization reactions. Covalent organic frameworks (COFs),<sup>37</sup> hyper-cross-linked polymers (HCPs)<sup>38</sup>, conjugated microporous polymers (CMPs)<sup>39</sup>, benzimidazole-linked polymers (BILPs), borazine-linked polymers (BLPs), nanoporous organic frameworks (NPOF), porous aromatic framework (PAF), porous polymer networks (PPN), and polymers of intrinsic microporosity (PIMs) are examples for porous organic polymers.

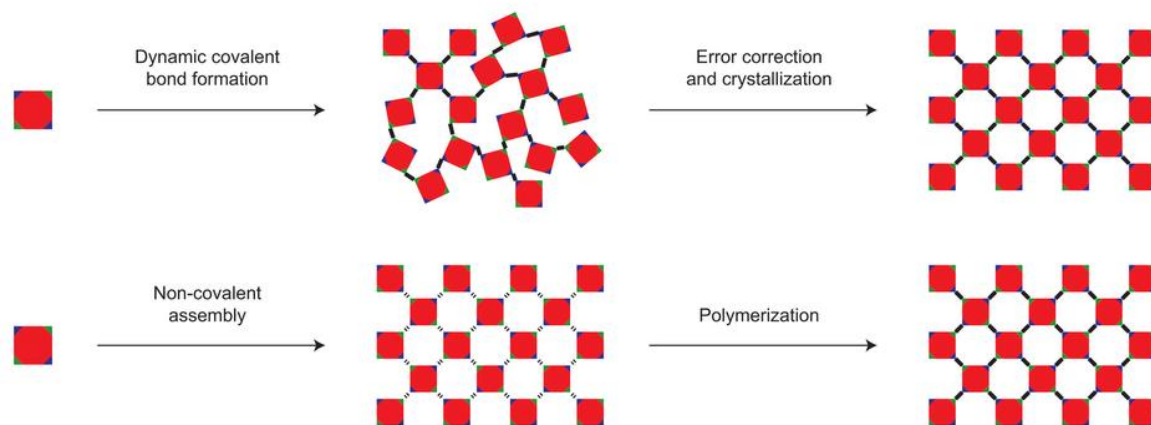


**Figure 1.5:** Schematic illustrations of the error correction step. This figure used with the permission from Nature Publishing Group.<sup>11</sup>

Covalent organic frameworks were introduced to the field by Yaghi in 2005<sup>2</sup>, and following this there has been remarkable progress in the synthesis and characterization of new COFs. The origin of COF synthesis involves reversible bond formation between organic linkers via self-condensation to boroxine rings (B-O-B linkages) or esterification to generate boronate ester (B-O-C) linkages. First, an initial polymerization occurs under dynamic covalent bond formation, followed by a reversible bond formation and breaking process to minimize the structural energy by forming ordered “crystalline” structure. This second step is also called “error correction” (Figure 1.5). COF-1 is the first synthesized COF, in which 1, 4-benzenediboronic acid was used under solvothermal reaction conditions.<sup>1</sup> Similarly, the reaction between phenylboronic

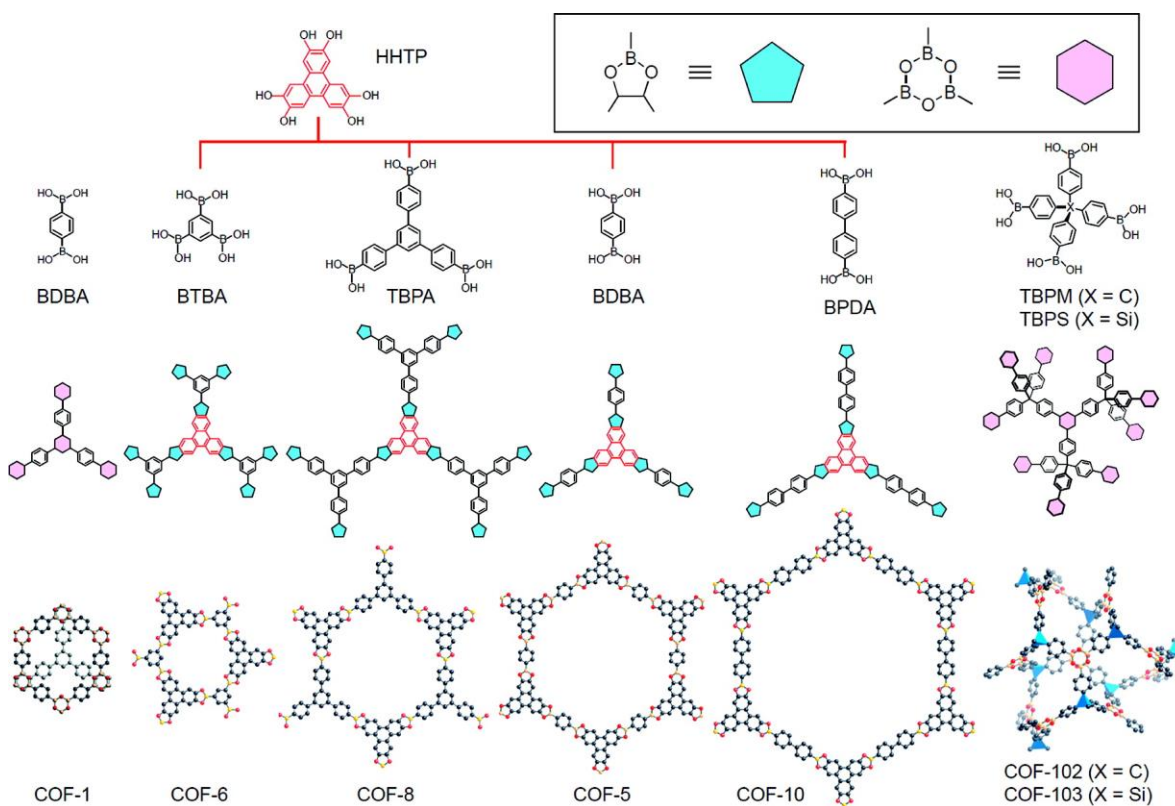


**Figure 1.6:** Formation of the COFs. Reprinted with permission from (FURUKAWA, H.; YAGHI, O. M., STORAGE OF HYDROGEN, METHANE, AND CARBON DIOXIDE IN HIGHLY POROUS COVALENT ORGANIC FRAMEWORKS FOR CLEAN ENERGY APPLICATIONS. J. AM. CHEM. SOC. 2009, 131, (25), 8875-8883.). Copyright (2009) American Chemical Society.

acid and hexahydroxyphenylene (HHTP) yielded COF-5 (Figure 1.6). The Brunauer Emmet Teller (BET) surface areas of COF-1 and COF-5 are 711 and 1590 m<sup>2</sup>/g, respectively. COF-6, -8 and -10 were synthesized using the same building unit (HHTP) in combination with other building units of different size and geometry.<sup>3</sup>

For practical CO<sub>2</sub> capture applications, porous materials must capture around 3-4 mmol g<sup>-1</sup> of CO<sub>2</sub> under atmospheric pressure to compete with the existing amine solvent scrubbing process. The amount of CO<sub>2</sub> captured by POPs directly depends on the pore functionality, surface area and pore size.<sup>40</sup> Therefore extensive study has gone into the design of new POPs which have high surface area, stability and the proper pore size and functional groups for the selective capture of CO<sub>2</sub>. The CO<sub>2</sub> uptakes of some well-known POPs at atmospheric pressure and at 273 K include COFs (1.3-3.8 mmol g<sup>-1</sup>), BPL carbon (3.3 mmol g<sup>-1</sup>), carbazole-based porous organic polymers CPOPs (4.82 mmol g<sup>-1</sup>), triptycene-based microporous poly-(benzimidazole) networks TBIs (2.7–3.9 mmol g<sup>-1</sup>)<sup>41, 42</sup> and –OH functionalized porous organic frameworks (POFs, 4.2 mmol g<sup>-1</sup>).<sup>15</sup>

El-Kaderi and coworkers have reported a new class of microporous organic polymers, called benzimidazole-linked polymers (BILPs)<sup>46-48</sup> (Figure 1.7) which have been synthesized through a metal-free condensation reaction between aryl-o-diamines and aryl-aldehydes that lead

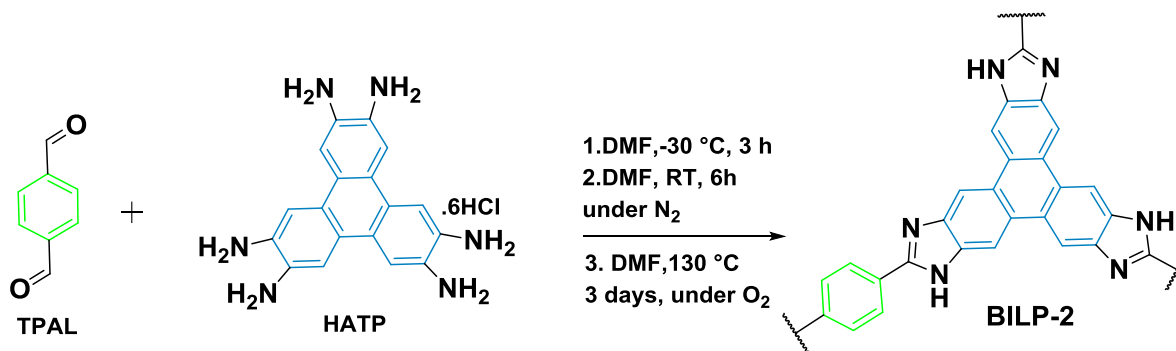


**Figure 1.7:** General synthetic method of the reported BILP-2.

to nitrogen-rich structures based on imidazole ring formation. BILPs are 2D or 3D amorphous polymers. Although their surface areas are moderate, they have superior properties such as very high chemical and physical stabilities as well as very high CO<sub>2</sub> uptake under ambient pressure (BILP-4: 5.3 mmol g<sup>-1</sup>). BILPs show very high thermal stability (up to 400 °C), evidenced by thermogravimetric analysis (TGA). In addition to BILPs, the El-Kaderi group reported a new class of porous polymers named azo-linked polymers (ALPs)<sup>49</sup> synthesized by homocoupling of aniline-like building units in the presence of copper(I) bromide and pyridine. ALPs have remarkable CO<sub>2</sub> uptake (up to 5.37 mmol g<sup>-1</sup>) at 273 K and 1 bar.

### 1.1.2 Diazaborole

There are several important properties of polymers that play a vital role in the performance of the materials in gas storage or selectivity CO<sub>2</sub> binding: surface area, structural crystallinity, and chemical functionality.<sup>5</sup> Porosity and pore shape are the two important parameters for high gas adsorption and separation; however, pore functionality tends to be more significant according to recent literature.<sup>50-52</sup> Incorporation of polarizable building blocks inside the pores has shown enhanced gas uptakes and gas selectivity. To give an example, the surface area of the PPN-6 is 4023 m<sup>2</sup> g<sup>-1</sup> and its CO<sub>2</sub> capacity is 1.16 mmol g<sup>-1</sup> at 1 bar, on the other hand, the CO<sub>2</sub> capacity after the functionalization of the PPN-6 with sulfonic acid (PPN-6-SO<sub>3</sub>H) is 3.60 mmol g<sup>-1</sup> at 1 bar.<sup>53</sup> In this regard, there have been many efforts to synthesize functional porous polymers. There are two methods for functionalization of the polymers: pre- and post-functionalization. In the post-functionalization process, desired functional groups are introduced into the network structure after polymerization as in the example of PPN-6-SO<sub>3</sub>H. On the other hand, in the pre-functionalization process, incorporation of the functional groups into the pores occurs prior to polymerization by starting with functionalized building monomers, this process is also called “auto-

functionalization”. Examples of these nitrogen rich porous polymers include: triazine-based polyimides (TPIs),<sup>54</sup> triptycene-based polymers of intrinsic microporosity (Trip(Et)-PIM),<sup>55</sup> polycarbazoles (CPOPs)<sup>56</sup> imine-linked microporous polymers,<sup>57, 58</sup> azo-linked polymers,<sup>51</sup> and benzimidazole-linked polymers (BILPs).<sup>50, 52, 59-61</sup> All of these porous structures have moderate surface areas but show high CO<sub>2</sub> capacity and selectivity.

Boron is a unique element to incorporate into the structure of porous organic polymers. The attractive feature of boron in the network is its ability to create a high density of Lewis acidic centers; an exceptional adsorbent surface for guest molecules.<sup>62</sup> However, because of the active sites of the boron atom, it is vulnerable to moisture, leading to decomposition as experienced in COFs. Nevertheless, boron-nitrogen bonds are known to be more stable compared to other derivatives because nitrogen’s lone pair electrons have the ability to conjugate with the vacant p-orbital of the boron atom.<sup>63-65</sup> In addition to increased bond stability, accessible nitrogen or amine functionalities on the pore walls, either through the selection of pre-functional building blocks or post functionalization of polymer network, can considerably enhance the CO<sub>2</sub> uptake as mentioned earlier.<sup>66, 67</sup> Monomeric species containing diazaborole rings have been previously synthesized and studied for the applications of light-emitting diodes, emissive materials, photovoltaic devices, nonlinear optics, and sensing.<sup>68</sup>

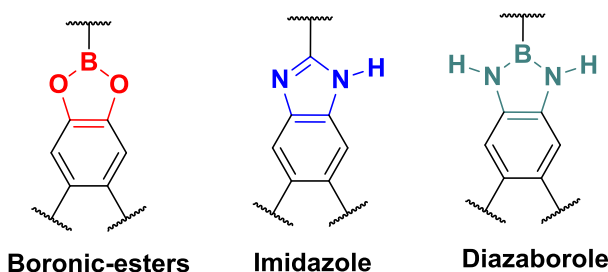


**Figure 1.8.** Boronate-ester, imidazole, and diazaborole building blocks.



Because of the accessible boron sites, pores of the polymer can be functionalized either through post- or pre- modification by adding variety of functional groups such as halides or alkyls (Figure 1.9). As we mentioned earlier, pore size of the polymer has significant effect on its gas storage capability. Thus, pore size can be tailored by adding

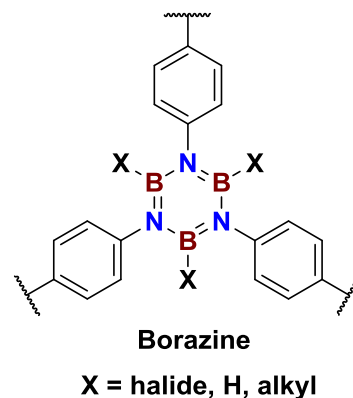
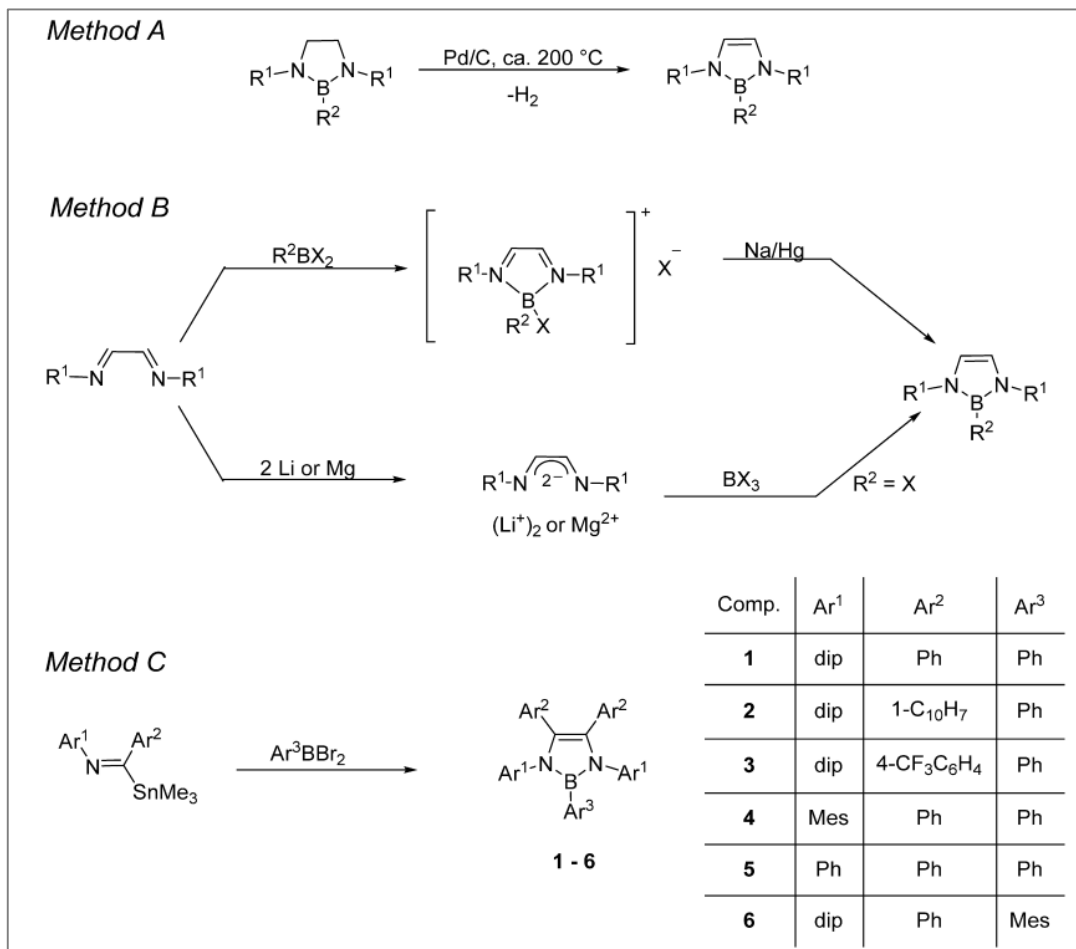


**Figure 1.9.** Borazine moiety

carefully selected functional groups with different sizes, for instance chlorine or bromine. One other advantage of having expandable boron sites is the incorporation of polarizable building units into the pores which has shown enhanced gas uptake properties.<sup>69</sup> Creating an electron density gradient by adding building blocks which have different electronegativity can polarize the gas molecules and enhance the storage capacity.

The first borazine decorated porous polymer has been reported by El-Kaderi *et al.* in 2011<sup>70, 71</sup> and afterward halide decorated BLPs have been synthesized. For example, BLP-1(H) and BLP-12(H) were formed by thermolysis of 1, 4-phenylenediamine and tetra-(4-aminophenyl)methane borane adducts in monoglyme to afford the corresponding polymers in good yields (Figure 1.10). The Brunauer-Emmett-Teller (BET) surface areas are 1360 and 2244 m<sup>2</sup>/g for BLP-1(H) and BLP-12(H), respectively. The H<sub>2</sub> uptake for BLP-1(H) (1.33 wt. %) is lower than that of BLP-12(H) (1.93 wt. %) and despite their amorphous nature, the hydrogen storage performances of the BLPs are comparable with other organic polymers. For example, under similar conditions the analogous crystalline COF-1<sup>8</sup> and CTF-1<sup>72</sup> store 1.28 and 1.55 wt. % of H<sub>2</sub>, respectively.



**Scheme 1.1:** Syntheses of monocyclic 1,3,2-benzodiazaboroles. Adapted from Ref. 7 with permission from Elsevier.

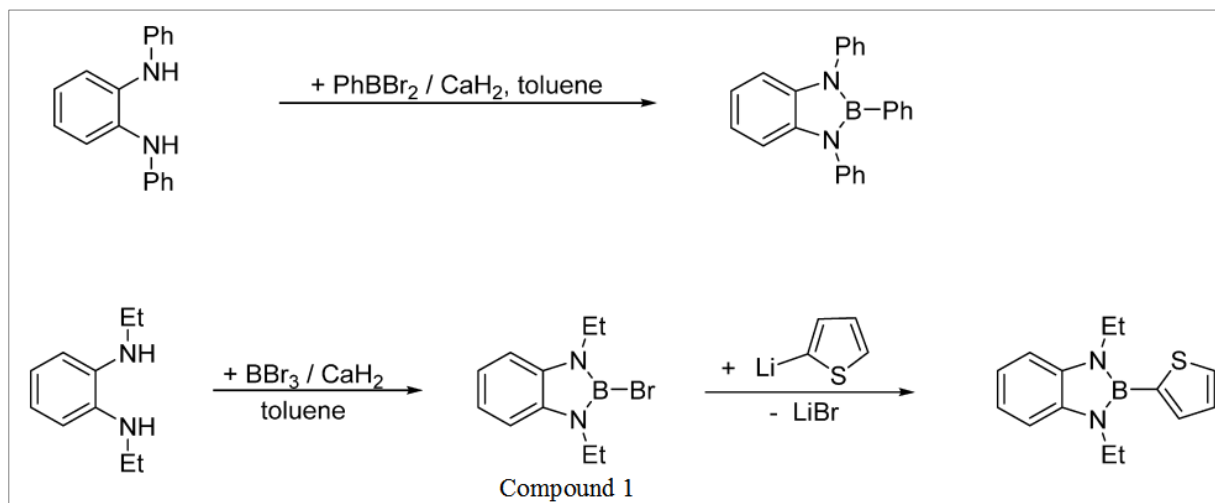
### 1.1.2.1 Synthesis of monocyclic 1,3,2-diazaboroles

In general there are three methods for the synthesis of monocyclic 1,3,2-diazaboroles (Scheme 1.1).<sup>7</sup> In method A, saturated 1,3,2-diazaborolidines undergo a catalytic dehydration to produce only alkyl and aryl-substituted derivatives of 1,3,2-diazaboroles. In method B, the 1,4-diazabutadienes can be transformed to 1,3,2-diazaboroles in two alternative routes: (1) 1,4-diazabutadienes converted to boronium salts and prior to treatment with Na/Hg, and (2) reduced first to 1,4-diazabutadiene-diides prior to boron trihalides cyclization. In this method, C,N,C-diaryl

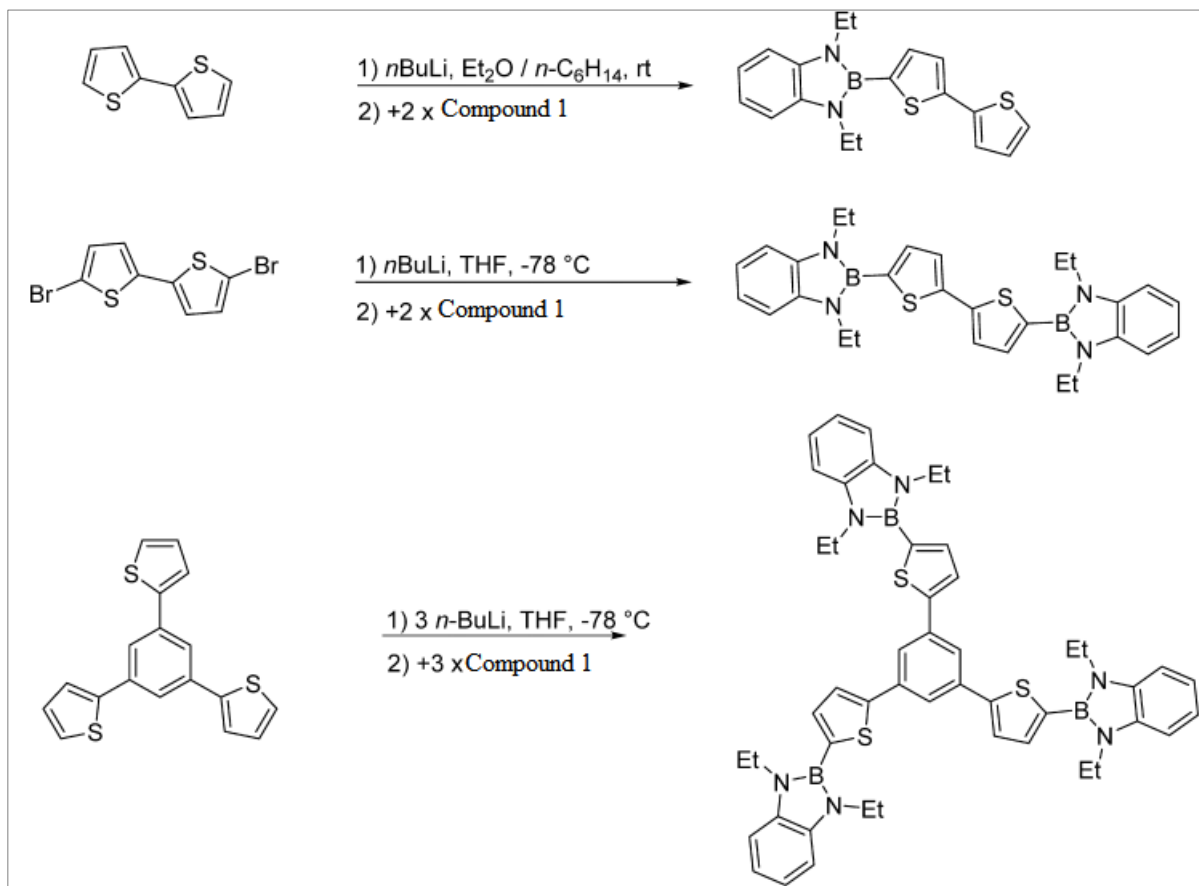
imidoylstannanes react with arylboron-dibromide to produce monocyclic 1,3,2-benzodiazaboroles.

### 1.1.2.2 Synthesis of 1,3,2-benzodiazaboroles

The reaction between phenyl-diamines with arylboron-dihalides through halide displacement or through reduction to diazaborolyl lithium followed by quenching with electrophiles led to the synthesis of 1,3,2-benzodiazaboroles (Scheme 1.2). Synthesizing Compound 1 in Scheme 1.2 opens the door to synthesize a variety of benzodiazaboroles upon treatment with organolithium compounds as seen in Scheme 1.2 and Scheme 1.3.

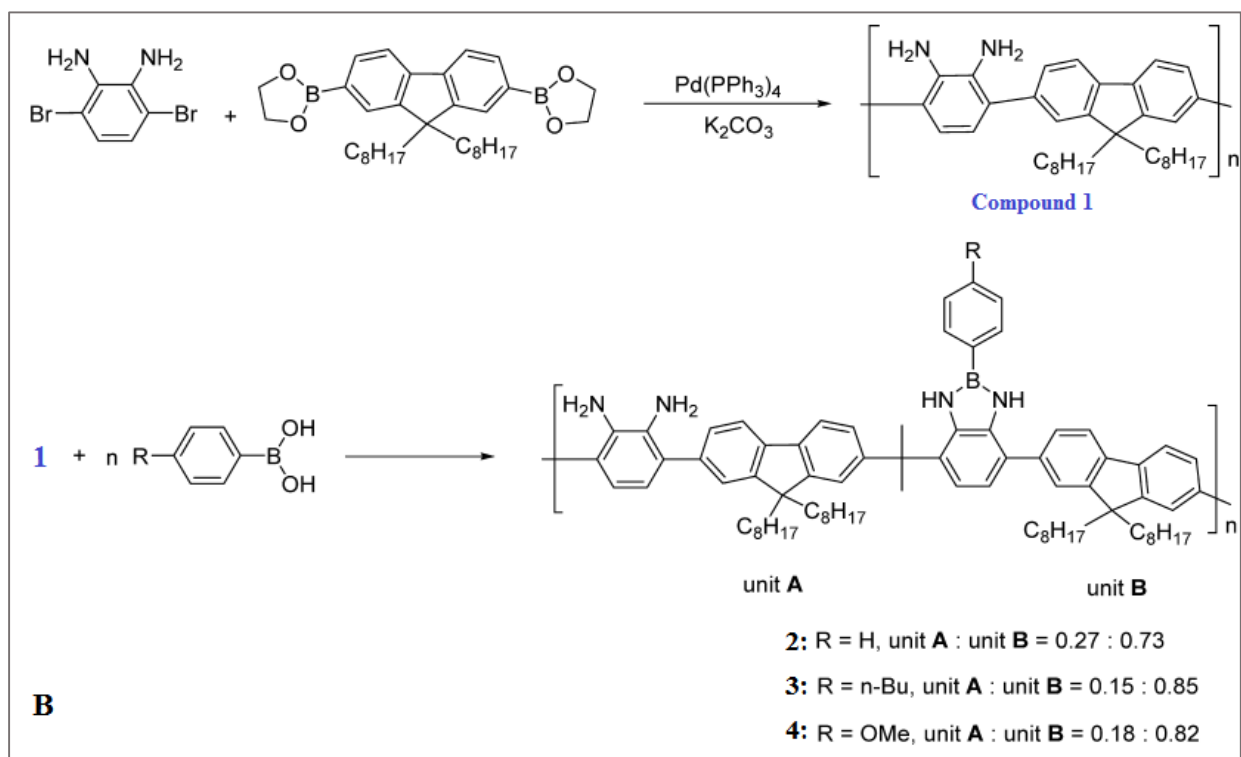
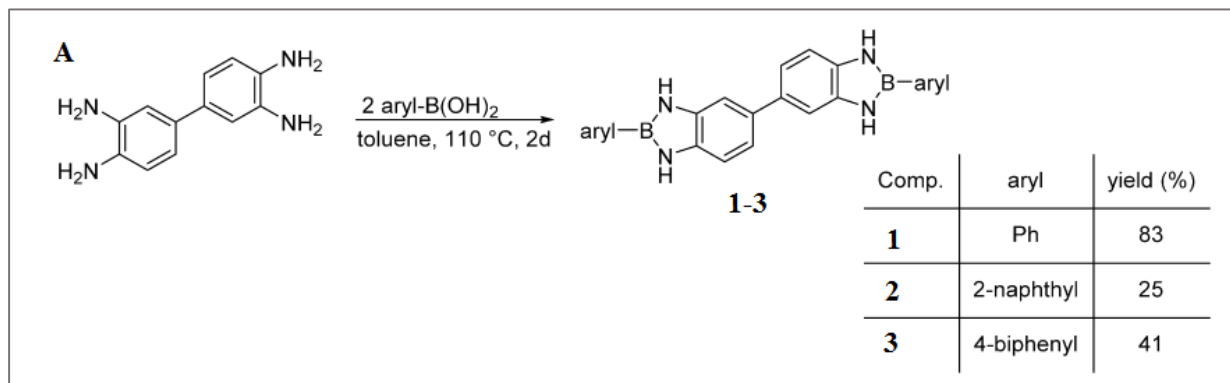


**Scheme 1.2:** Syntheses of 1,3,2-benzodiazaboroles by cyclocondensation and by organo/bromine exchange. Adapted from Ref. 7 with permission from Elsevier.



**Scheme 1.3:** Examples of 1,3,2-benzodiazaboroles synthesized by using organolithiums.

Compound 1 is described in Scheme 1.2. Adapted from Ref. 7 with permission from Elsevier.



**Scheme 1.4:** Syntheses of 1,3,2-benzodiazaboroles by condensation reaction. Adapted from Ref. 7 with permission from Elsevier.

One other approach to synthesize the 1,3,2-benzodiazaboroles is the condensation reaction between phenyl-diamines and boronic acid derivatives. Early examples showed only synthesis of the discrete molecules (Scheme 1.4-A), however, recently side chain functionalization of the polymers with the benzodiazaboroles has been introduced to the field (Scheme 1.4-B). This

method is highly advantageous as it eliminates byproducts, which can facilitate material isolation and purification. We will discuss in detail the use of this synthetic route in the preparation of highly porous polymers containing diazaborole units.

### 1.1.3 Pore Characterization of Solid Sorbents

As stated above, coordination polymers are promising materials for small gas storage and separation due to the ability of these polymers to confine gas molecules in the pores of the network. Thus, the amount of gas molecule (guest) captured in the pores directly depends on the structural properties of the walls such as, shape, pore volume, and functional groups in the pores. The electrostatic interaction between the guest molecules and the pore walls “physisorption” requires significantly lower energy to release trapped gas molecules than chemical adsorption, “chemisorption”, in which chemically bonded guests cannot be removed easily. In this regard, physisorption has been widely used for surface characterization of porous solids.

An adsorption or desorption isotherm is a measurement in which the temperature remains constant for the experiment, while the amount of adsorbed or desorbed gas calculated as a function of relative pressure ( $P/P_0$ ). Where  $P$  is the absolute pressure and  $P_0$  is the vapor pressure of a pure liquid. Pore size, surface area and pore shape of porous materials can be determined by the measurements of their pure gas isotherms, generally Ar or N<sub>2</sub>. Brunauer-Emmett-Teller (BET) categorized five isotherm types in 1940, and later IUPAC has recognized a type VI isotherm. These six adsorption isotherms are shown in (Figure 1.9). Type I isotherm is representative of a microporous material, in which a sharp initial uptake can be seen followed by a plateau region, which indicates the adsorption of very small gases. The sharp initial uptake arises from the relatively stronger fluid-solid interaction than the fluid-fluid interaction. Type II isotherms are characteristic of nonporous or a macroporous material, here, there is a small initial uptake followed

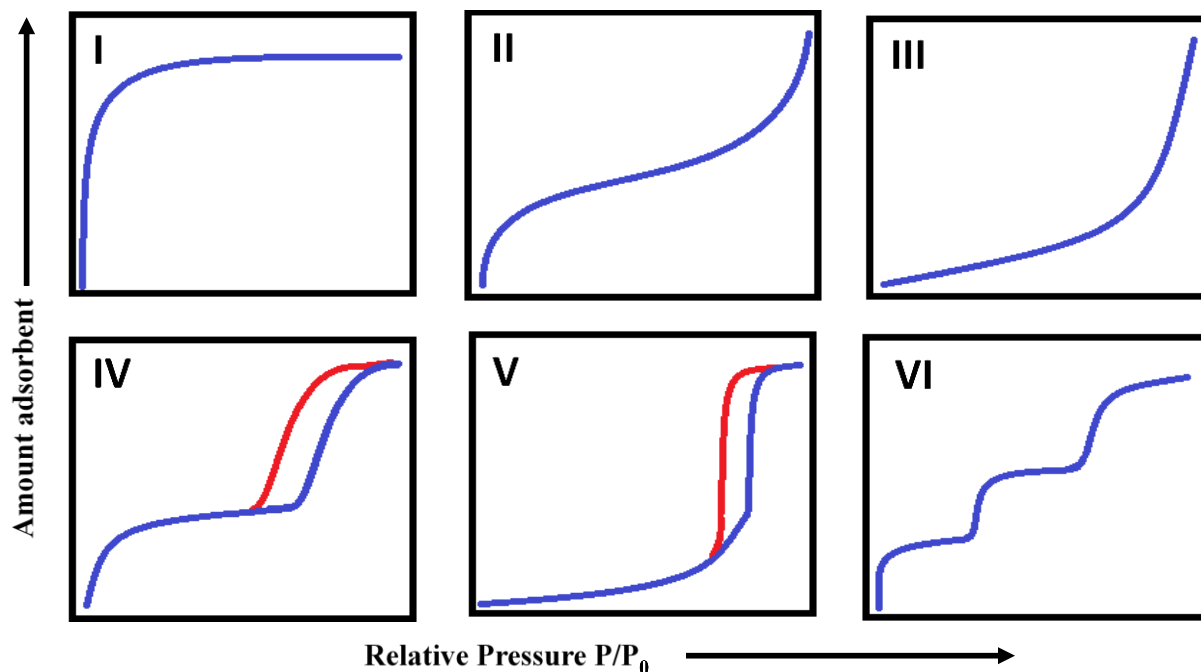


**Figure 1.11** Six types of isotherms as identified by Brunauer-Emmett-Teller and Sing. Blue line is adsorption and red desorption.

by relatively increasing trend. The linear portion indicates the saturation of the monolayer and accumulating the guest molecules as multilayers. The type III isotherm, similar to the type V, shows no/or very little initial uptake at very low pressures, due to the greater interaction of fluid-fluid rather than fluid-solid. The type IV isotherm represents mesoporous materials and follows the same trend with type II excepting a large second step adsorption portion at higher pressures with a hysteresis which appears between the adsorption and desorption isotherm. The second step increase is due to capillary condensation, in which the adsorbate molecules condense inside the small pores, capillaries and hysteresis arise from the difference in the mechanism of adsorption and desorption. Type V isotherms are same with the type III except they show the mesoporous characteristic of the materials. Finally, the type VI isotherm has been identified in recent years for materials which show more than one type of sorption site. Surface area can be calculated from the

adsorption isotherms by simply calculating the amount of adsorbed material on the pore walls of the adsorbent. The two main theories for calculating the surface area of porous materials are Langmuir theory and Brunauer-Emmett-Teller (BET) theory, and measurements calculated from these different methods are called Langmuir and BET surface areas.

In 1916, Irving Langmuir proposed one of the early adsorption models which is based on four important assumptions (1) there is only monolayer formation at the maximum adsorption, (2) the surface of the adsorbent is uniform, (3) adsorbed molecules do not interact with each other (4) there is only one kind of mechanism for the entire adsorption process. The Langmuir equation is as follows;

$$\frac{P}{W} = \frac{1}{aW_m} + \frac{P}{W_m}$$

Where  $P$  is the pressure,  $a$  is a constant,  $W$  is weight of the material, and  $W_m$  is the weight of a monolayer.  $W/W_m$  is called fractional coverage. The slope,  $\frac{1}{W_m}$ , of the equation and  $W_m$  can be determined by plotting the  $P/W$  as a function of pressure. Specific surface area,  $S$ , can be calculated using the equation;

$$S_T = \frac{W_m N A_{cs}}{M}$$

$$S = \frac{S_T}{w}$$

Where  $S$  is the specific surface area,  $S_T$  is the total surface area,  $A_{cs}$  is the cross-sectional area of the adsorbate,  $M$  is the molecular weight of the adsorbate and  $w$  is the sample weight.



However, Langmuir's assumptions are not entirely true due to the surface non-ideality, multilayer formation and different adsorption mechanisms. Thus, Brunauer-Emmett-Teller (BET) extended Langmuir's theory. The BET model accounts for the formation of multiple layers of the adsorbate during the adsorption (Figure 1.10). The Langmuir equation was thus modified as follows;

$$\frac{1}{W\left[\left(\frac{P}{P_0}\right) - 1\right]} = \frac{1}{aW_m} + \frac{a - 1}{W_m a} \left(\frac{P}{P_0}\right)$$

A linear plot of  $1/[W((P/P_0)-1)]$  as a function of the relative pressure,  $P/P_0$ , gives us the BET surface area. Since BET theory accounts for multilayer formation (which means not only adsorbate-adsorbent interaction, but also adsorbate-adsorbate interaction) this surface area calculation method is thought to be more reliable and it is more accurate for micro-, meso- and macroporous materials.

There are several theories for calculating the pore size distribution (PSD) of porous materials by using pure gas isotherms such as argon, nitrogen and CO<sub>2</sub>. Density Functional Theory (DFT), Barrett-Joyner and Halenda (BJH), Horvath and Kawazoe (HK), and Non-Local Density

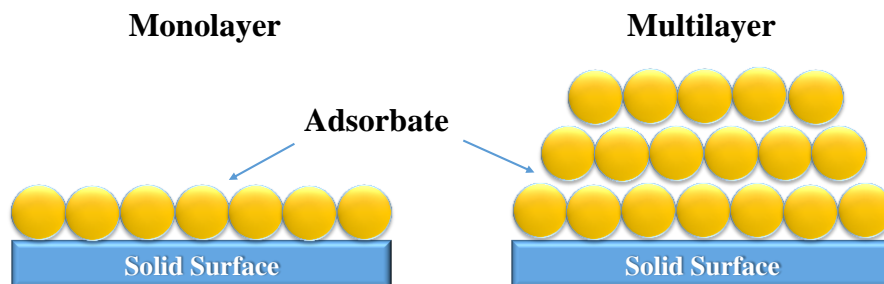


**Figure 1.12** Formation of monolayer (Langmuir) and multilayer (BET) theory.

Functional Theory (NLDFT) can be used to investigate porosity. For investigating the pore size distribution of the porous materials, the NLDFT approach is commonly used, which is used in the later chapters for data presentation. Simply, the NLDFT model integrates the experimental single pure gas isotherm to calculate the pore size distribution. The nitrogen isotherm (at 77 K) is commonly used for calculating the surface area and pore size distribution because nitrogen is inert and its kinetic diameter is relatively small (3.64 Å).<sup>24</sup> Argon is another inert gas with a kinetic diameter slightly smaller than nitrogen (3.39 Å). One advantage of argon over nitrogen is the fact that it can measure pore sizes down to ~4.0 Å, whereas nitrogen ~7.0 Å, due to the smaller diameter of Ar. Finally, CO<sub>2</sub> molecules with a kinetic diameter of 3.30 Å and high kinetic energy at high measurement temperature (273 K) comparing to the cryogenic temperatures for Ar and N<sub>2</sub>, helps in penetrating deep into the narrower pores typically inaccessible by Ar or N<sub>2</sub> molecules.

#### 1.4 Dissertation Problem

High atmospheric CO<sub>2</sub> concentration is the greatest factor presently contributing to global warming. Outside of fossil fuels, renewable energy sources are great candidates to solve the problem of CO<sub>2</sub> emission, but there are no such energy sources to supply the demand. It is projected that fossil fuel consumption will continue to increase. While these technologies are being developed, limiting CO<sub>2</sub> release to the atmosphere is vital and as such, CO<sub>2</sub> capture and sequestration (CCS) has captured great interest over the past decades. Porous materials such as zeolites, metal organic frameworks (MOFs) and covalent organic frameworks (COFs) are promising solid adsorbent materials and alternatives to current sequestration methods. Although, MOFs are one of the important candidates for gas storage, most of them become unstable and degrade under practical storage conditions; which limits their use. Porous organic polymers, on the other hand, show remarkable properties such as very low density, superior stability, adjustable pore size and functionality, and very high surface area and recyclability, which are features that make them possible gas storage and separation adsorbents. Our recent reported porous polymer families BILPs and ALPs have shown impressive CO<sub>2</sub> uptake and selectively capture of CO<sub>2</sub> over N<sub>2</sub> and CH<sub>4</sub> under 1 atm at 273 K. However, due to their amorphous structure, which brings the limitation of pore formation engendering, and moderate surface area, their CO<sub>2</sub> capture performances under elevated pressure remains modest.

Hydrogen is a promising replacement for fossil fuels, because of its high energy capacity, abundance and cleanness, with only water being the byproduct after combustion. However, due to the high volumetric density, storage is a real challenge for on-board applications. Recently, our group introduced a new porous organic polymer, called triptycene-derived covalent organic framework (TDCOF-5), which has highly ordered microcrystalline structure and a very high BET

surface area  $2497 \text{ m}^2 \text{ g}^{-1}$ . TDCOF-5 was synthesized through a condensation reaction between 1,4-benzenediboronic acid and hexahydroxytritycene which leads to the formation of boronate ester linkages. Because of the unique structure of triptycene, which is known to allow for a high degree of internal free volume, the latent edges of building units of the polymer are exposed for interaction with gas molecules. TDCOF-5 has the highest  $\text{H}_2$  uptake under 1 atm at 77 K (1.6%) among all known 2D and 3D COFs derived from B–O bond formation and moderate  $\text{CO}_2$  uptake ( $2.1 \text{ mmol g}^{-1}$ ) with the  $Q_{st}$  values of  $6.6 \text{ kJ mol}^{-1}$  and  $21.8 \text{ kJ mol}^{-1}$  respectively. However,  $\text{CO}_2$  and  $\text{H}_2$  uptakes fall behind the practical application targets. One disadvantage of COFs is their high moisture sensitivity due to the vacant boron p-orbital which allow for nucleophilic attack by water. To overcome this problem, we have designed a new type of porous organic polymer, named diazaborole-linked polymers (DBLPs) and successfully developed a synthetic procedure for polymer preparation. The delocalized electronic structure of DBLPs is believed to retard the interaction of incoming water molecules with the vacant boron p-orbital making these polymers more chemically robust than COFs. Another advantage of diazaborole decorated pore channels is a high number of accessible nitrogen interaction sites. It has proven that nitrogen-rich porous structures have enhanced gas uptakes, especially towards  $\text{CO}_2$  through hydrogen bonding. DBLPs reported herein have been synthesized through a condensation reaction between aryl-o-diamine and boronic acid building blocks and were evaluated for gas uptake and selective  $\text{CO}_2$  binding.

## Chapter 2

### Targeted Synthesis of a Mesoporous Triptycene-Derived Covalent Organic Framework

#### 2.1 Introduction

Covalent organic frameworks (COFs) are highly porous microcrystalline materials that have received considerable attention as a result of their potential in areas that encompass gas storage, catalysis, and electronics.<sup>73</sup> The formation of covalent bonds involved in connecting molecular building blocks during polymerization processes can retard crystalline network formation, however, COFs based on B-O,<sup>1-4</sup> C-N,<sup>42, 72, 74</sup> and B-N<sup>75</sup> bonds have been reported. In particular, COFs based on B-O bond formation are well investigated due to the kinetically labile nature of this bond which is essential for overcoming the crystallization problem of covalent networks.<sup>1</sup> Furthermore, 2D COFs are very common and their solid-state assembly is typically driven by electron rich building blocks that exhibit favorable  $\pi$ - $\pi$  stacking interactions that can hinder the accessibility of boron sites. These sites are very relevant to gas storage applications as demonstrated by experimental and theoretical studies.<sup>62, 76</sup> Additionally, it has been proven that enhanced porosity can be attained through exposing the latent edges of building units which act as potential interaction sites during gas storage processes.<sup>77</sup> Along this line, triptycene is known to allow for a high degree of internal molecular free volume,<sup>78, 79</sup> and therefore, triptycene-based porous materials possess enhanced adsorptive gas uptake capacities as demonstrated for polymers of intrinsic microporosity,<sup>55</sup> shape-persistent cage molecules,<sup>80</sup> metal salphens,<sup>81</sup> and MOFs.<sup>82</sup>

In this study we demonstrate for the first time the use of triptycene in constructing a mesoporous 2D COF that has high surface area, accessible boron sites, and enhanced gas storage capacity.

## 2.2 Experimental Section

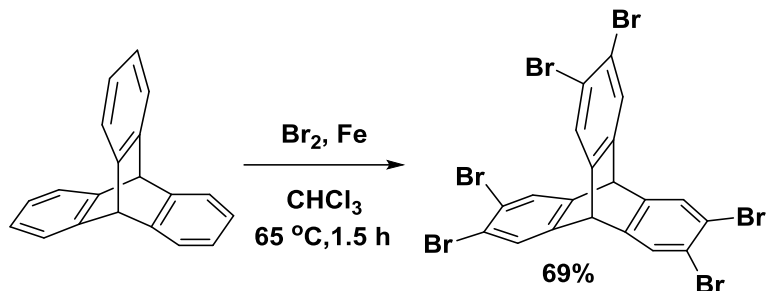
### 2.2.1 Materials and Methods

All starting materials, unless noted otherwise, were obtained from Aldrich Chemicals and used without further purification. Chromatographic separations were performed using standard column chromatography methods using silica gel purchased from Acros Organics (60 Å, 35-70 µm). Solvents were dried by distillation from Na (toluene) or Na/benzophenone (THF). 2, 3, 6, 7, 12, 13-hexahydroxytriptycene was prepared according to literature methods.<sup>55</sup> All products were handled under a nitrogen atmosphere using glovebox or Schlenk line techniques. Solution <sup>1</sup>H and <sup>13</sup>C NMR spectra were obtained on a Varian Mercury-300 MHz NMR spectrometer. Elemental analyses were performed by Midwest Microlab, Indianapolis, IN. Higher carbon and hydrogen contents may result from residual hydrocarbons in the cavities. FT-IR spectra were obtained using a Nicolet-Nexus 670 spectrometer equipped with Smart iTR™. Representative solid-state nuclear magnetic resonance (NMR) spectra were recorded at ambient temperature on a Bruker DSX-300 spectrometer using a Bruker magic angle spinning (MAS) probe with 4 mm (O.D.) 80 µL volume zirconia rotors with Kel-F drive caps at Spectral Data Services, Inc. SEM samples were prepared by dispersing the material onto a sticky carbon surface attached to a flat aluminum sample holder. The samples were then platinum coated using an EMS (Electron Microscopy Sciences) 550x Sputter Coater at 1x10<sup>-1</sup> mbar of pressure in a nitrogen atmosphere for 90 seconds while maintaining 20 mA of current. Samples were analyzed on a Zeiss EVO XVP Scanning Electron Microscope using the SEI detector with accelerating voltages ranging from 10 kV to 20 kV.

Powder X-ray diffraction data were collected on a Panalytical X'pert pro multipurpose diffractometer (MPD). Samples were mounted on a sample holder and measured using Cu K $\alpha$  radiation with a  $2\theta$  range of 1.5-35. Thermogravimetric analysis was obtained using a TA Instruments TGA Q5000 analyzer with 50  $\mu$ L platinum pans to assess the thermal stability of the polymer. Experiments were run at a ramp rate of 5 K/minute under a nitrogen atmosphere. Argon sorption experiments were run using a Quantachrome Autosorb iQ2 analyzer. In a typical experiment, a sample was loaded into a 9 mm large bulb cell (Quantachrome) of known weight and then hooked up to Autosorb IQ2 and degassed at 120 °C for 12 h. The degassed sample was refilled with nitrogen, weighed and then transferred back to the analyzer. The temperatures for adsorption measurements were controlled by using a bath of liquid nitrogen (77 K), liquid argon (87 K), or temperature controlled water bath (273 K and 298 K). Hydrogen isotherms were collected at 77 K and 87 K. Carbon dioxide and methane isotherms were collected at 273 K and 298 K. Pore Size Distribution (PSD) was calculated using spherical/cylindrical pore (zeolite) NLDFT adsorption model.<sup>83</sup>

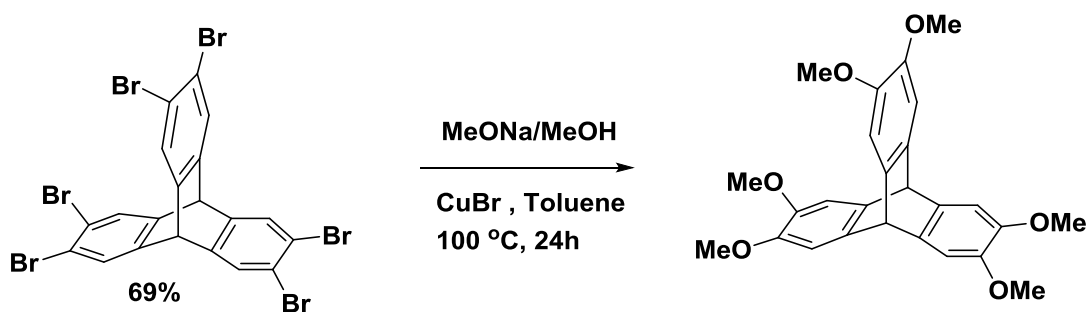
### 2.2.2 Synthesis of 2, 3, 6, 7, 12, 13-hexabromotriptycene

This compound was synthesized according to a published method.<sup>84</sup> Triptycene (1.06 g, 4.18 mmol) was dissolved in dry chloroform (stabilized with amylene) (100 mL) in a Schlenk flask under nitrogen. Iron (30 mg) and bromine (1.35 mL, 26.3 mmol) were added, and the solution was refluxed for 1.5 h. Excess chloroform and bromine were removed under vacuum. Recrystallization from hot chloroform yielded a white solid (4.0 g, 69%). <sup>1</sup>H NMR (300 MHz, CDCl<sub>3</sub>)  $\delta$  (ppm) 5.23 (s, 2H), 7.62 (s, 6H). <sup>13</sup>C NMR (75 MHz, CDCl<sub>3</sub>)  $\delta$  (ppm) 144.2, 129.3, 122.0, 51.3



### 2.2.3 Synthesis of 2, 3, 6, 7, 12, 13-hexamethoxytriptycene

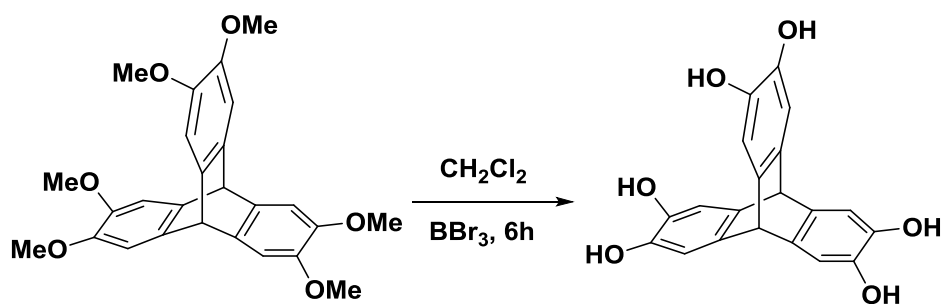
According to the procedure of Ghanem et al.<sup>55</sup> a mixture of 2,3,6,7,12,13-hexabromotriptycene (4.92 g, 6.76 mmol), copper(I) bromide (0.6 g, 4.2 mmol), 25 wt. % sodium methoxide in methanol (70 mL, 1.22 mol), ethyl acetate (5 mL), and dry toluene (100 mL) was refluxed under nitrogen overnight. The mixture was cooled down, quenched with addition of 50 ml water and extracted with dichloromethane. The organic layer was dried over  $\text{MgSO}_4$  and the solvent removed by rotary evaporation to give off white powder crystals (2.72 g, 93% yield)  $^1\text{H}$  NMR (400 MHz;  $\text{CDCl}_3$ )  $\delta$  (ppm): 3.84 (s, 18H), 5.19 (s, 2H), 7.01 (s, 6H);  $^{13}\text{C}$  NMR (100 MHz;  $\text{CDCl}_3$ )  $\delta$  (ppm): 53.2, 56.3, 108.5, 139.0, 145.8





## 2.2.4 Synthesis of 2, 3, 6, 7, 12, 13-hexahydroxytriptycene

According to the procedure of Zhu et al.<sup>85</sup> 2, 3, 6, 7, 12, 13-hexamethoxytriptycene (1.48 g, 3.0 mmol) dissolved in the dry dichloromethane (70 ml) at 0 °C under a nitrogen atmosphere and boron tribromide (3.4 g, 19.8 mmol) was added dropwise and the mixture stirred at room temperature for 3 h. The reaction was quenched by adding icy water and the precipitate was filtered, washed with water and dried. The crude powder product was recrystallized from THF/petroleum ether and filtered over a medium glass frit to give pale pink crystals (1.20 g, 98 %).

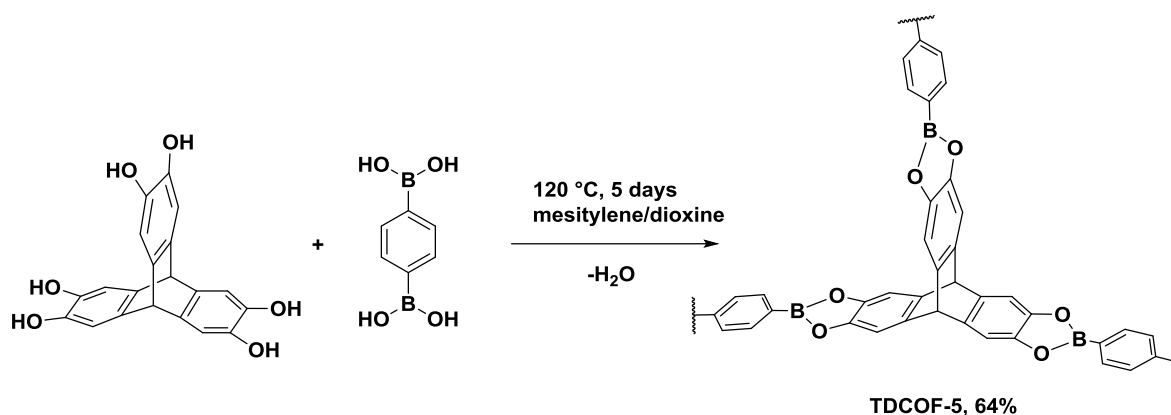


## 2.2.5 Synthesis of Triptycene-Derived Covalent Organic Framework (TDCOF-5)

A Pyrex tube with an outer diameter of 12 mm and inner diameter of 10 mm was charged with 2, 3, 6, 7, 12, 13-hexahydroxytriptycene (46 mg, 0.13 mmol) and benzene-1, 4-diboronic acid (30 mg, 0.18 mmol) under nitrogen ( $\text{N}_2$ ) flow. 3 mL of a 1:1.5 (v: v) solution of mesitylene: dioxane was added. The tube was flash frozen at 77 K (liquid nitrogen bath) evacuated and flame sealed. The reaction mixture was heated at 120 °C for 5 days with a rate of 0.1 °C per minute and the resulting white precipitate was isolated by filtration over a medium glass frit and washed with anhydrous acetone twice (2x15 mL). The product was immersed in anhydrous acetone (15 mL) for two days and the solvent was changed and freshly replenished five times. The solvent was

removed by filtration and dried at 85 °C to give TDCOF-5 as a white powder (38 mg, 64 %). Anal.

Calcd. for (C<sub>28</sub>H<sub>58</sub>B<sub>6</sub>O<sub>12</sub>): C, 70.96; H, 2.87. Found: C, 69.39; H, 3.24.



## 2.3. Results and Discussion

### 2.3.1 Synthesis and Characterization of TDCOF-5

The synthesis of TDCOF-5 was performed by the hydrothermal treatment of a mixture of 1,4-benzenediboric acid and hexahydroxytriphenylene in a solvent mixture of mesitylene/dioxine for 5 days at 120 °C. TDCOF-5 was isolated and purified under an inert atmosphere of nitrogen and was investigated by spectral and analytical methods which included FT-IR, solid-state <sup>11</sup>B and <sup>13</sup>C MAS, and elemental analysis while solid-state packing was determined by powder x-ray diffraction (PXRD) and materials modeling studies. TDCOF-5 was isolated as a white microcrystalline powder and purified by washing with anhydrous acetone then degassed at 120 °C and 1.0 x 10<sup>-5</sup> Torr for 16 h prior to characterization and porosity measurements.

The formation of the boronate ester linkage was first established by FT-IR studies (Figure 2.1) which revealed a significant depletion of the boronic acid and hydroxyl bands and the formation of characteristic bands consistent with the boronate ester bond at  $1352\text{ cm}^{-1}$  (B-O).<sup>1-4</sup> The solid-state  $^{11}\text{B}$  and  $^{13}\text{C}$  NMR further supports the formation of the  $\text{C}_2\text{O}_2\text{B}$  ring and the incorporation of an intact triptycene moiety into the framework of TDCOF-5. The signal for  $^{11}\text{B}$  MQ-MAS (Figure 2.2) was observed as a broad signal centered about 13.4 ppm, consistent with tri-coordinate boron signals, previously reported for COFs containing boronate ester linkages.<sup>1-4</sup> In addition, the  $^{13}\text{C}$  CP-MAS spectrum (Figure 2.3) contains signals that arise from the triptycene and phenyl building units. The TGA trace for activated TDCOF-5 indicated thermal stability at up to  $420\text{ }^\circ\text{C}$  under an argon atmosphere which is in-line with most COFs (Figure 2.4). The morphology and phase purity of TDCOF-5 were investigated by scanning electron microscopy (Figure 2.5) which revealed aggregated rectangular prisms of  $\sim 150\text{ nm}$  in size.

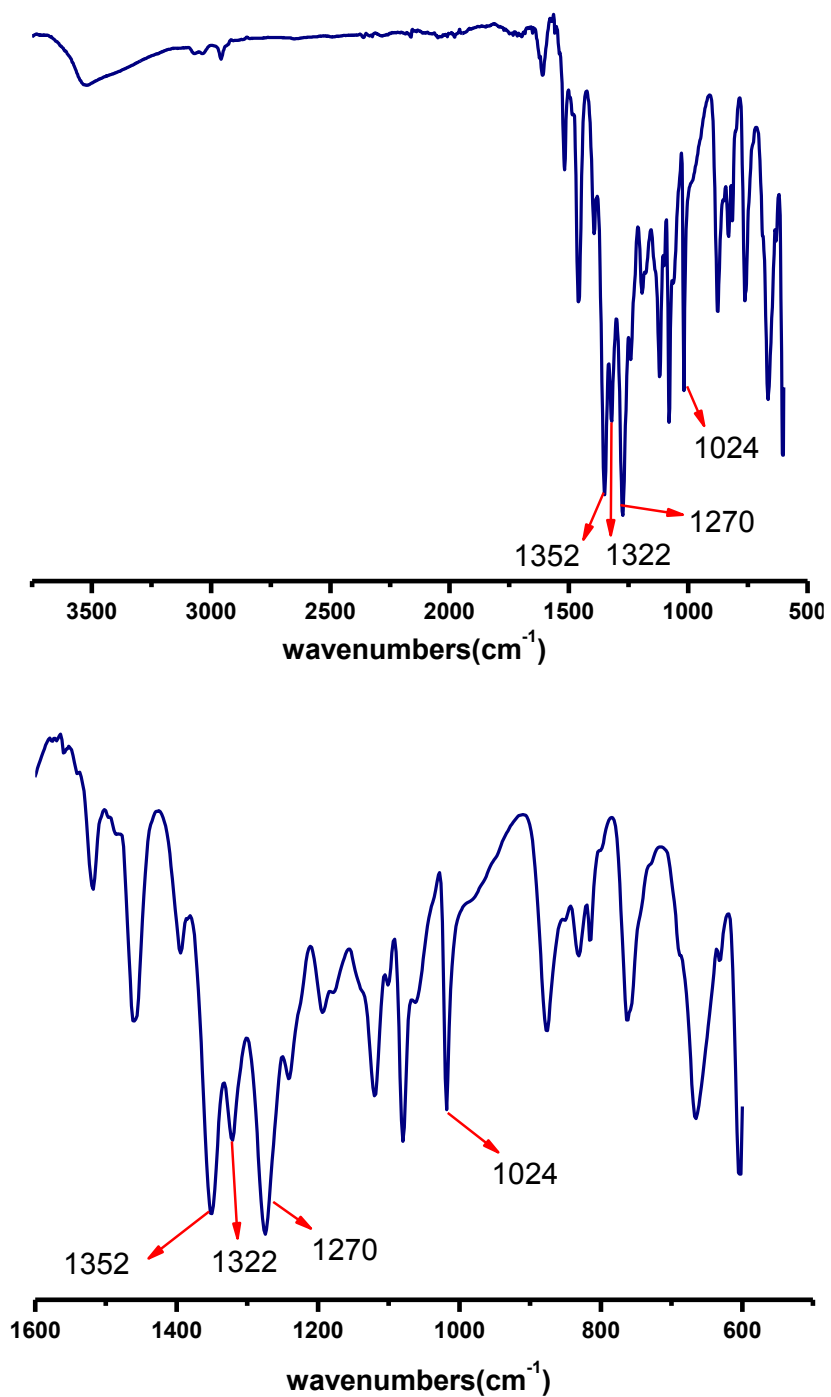


**Figure 2.1:** FT-IR spectra were obtained as KBr pellets using a Nicolet Nexus 670 FT-IR spectrometer. The formation of the  $\text{BC}_2\text{O}_2$  ring is supported by the following IR-bands ( $\text{cm}^{-1}$ ): B-O (1352), B-C (1270), and C-O (1024). FT-IR results are in line with previous reported COFs.<sup>1-4</sup>

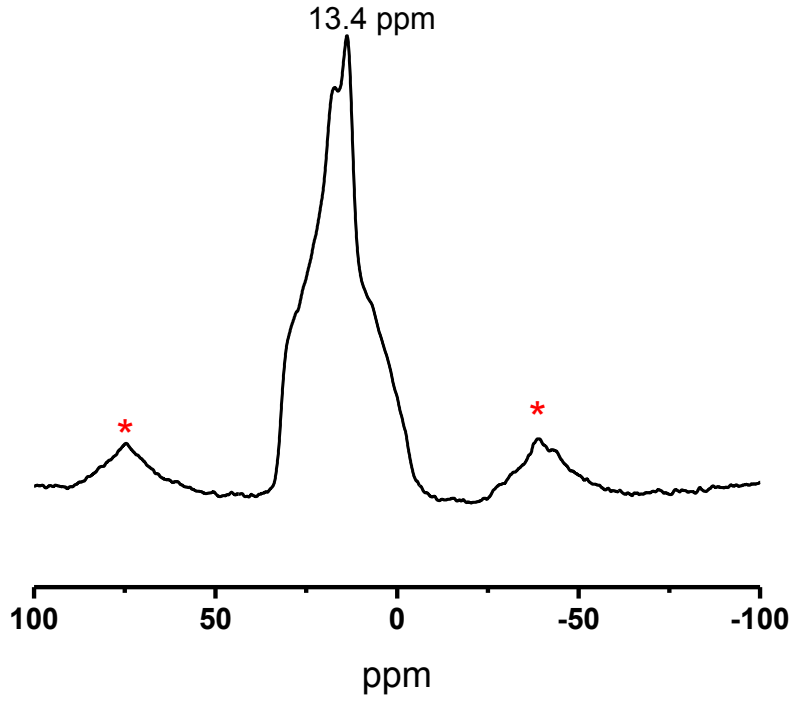


**Figure 2.2:** Solid-state  $^{11}\text{B}$  multiple quantum MAS (MQMAS) NMR spectrum of TDCOF-5; asterisks denote spinning-side bands.

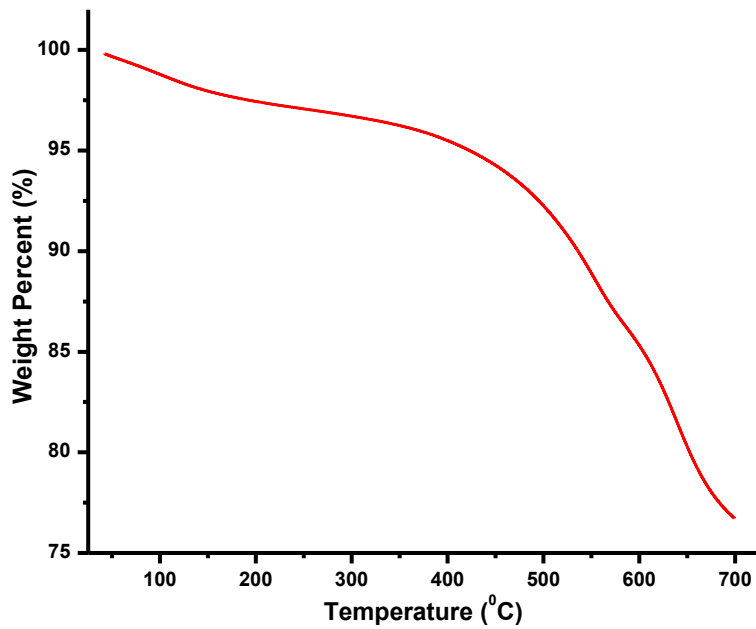
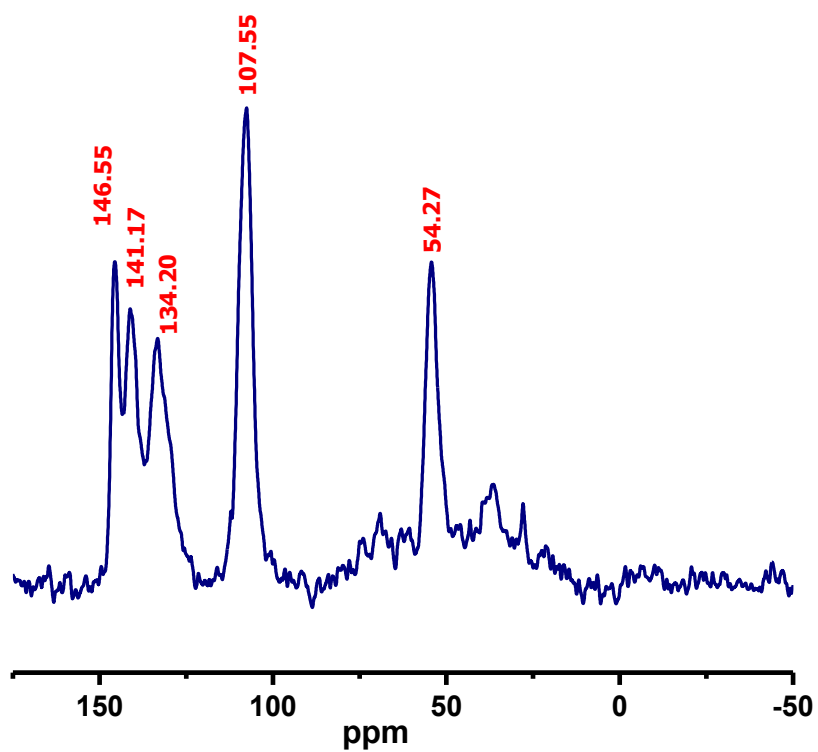


**Figure 2.3:** TGA for an activated sample of TDCOF-5



Carbon	Chemical Shift (ppm)
1	54.27
2	141.17
3	107.55
4	146.55
5	134.20
6	134.20

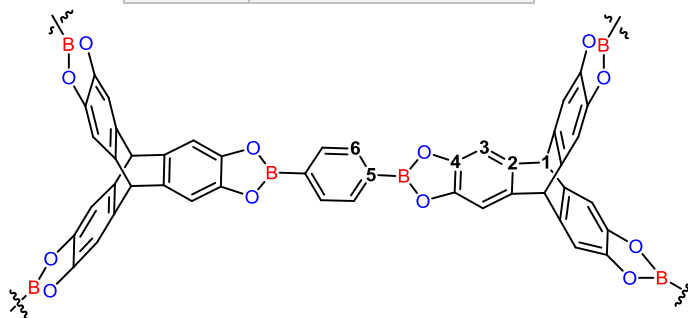


**Figure 2.4:** Solid-State  $^{13}\text{C}$  CP-MAS NMR spectrum for TDCOF-5.

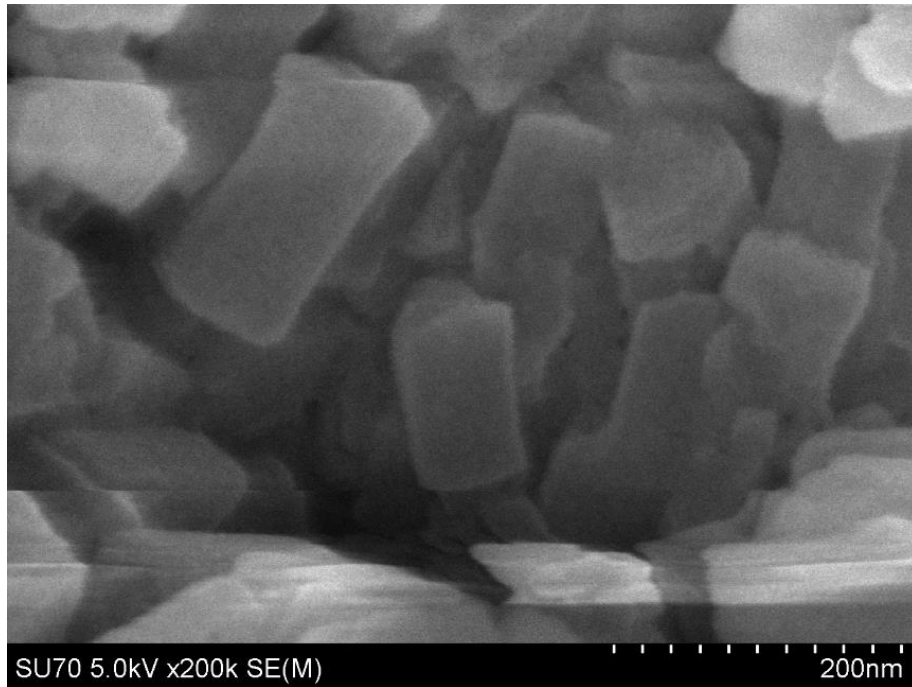
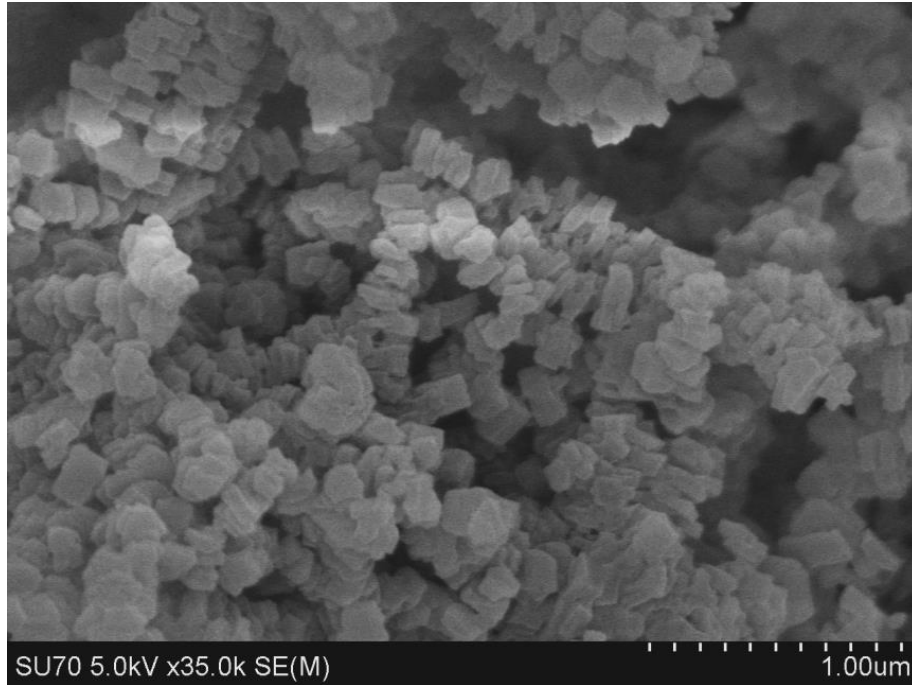


**Figure 2.5:** SEM images of as-prepared TDCOF-5

### 2.3.2 Porosity Studies of TDCOF-5

Prior to porosity and gas uptake measurements, a sample of TDCOF-5 (~75 mg) was activated by degassing at 120 °C and  $1 \times 10^{-5}$  Torr for 16 h to remove residual solvent and gas molecules from the pores. The Type IV argon isotherm (Figure 2.6) is consistent with a mesoporous material that is characterized by a sharp uptake at  $P/P_0 = 10^{-5}$  to  $10^{-2}$  followed by a second step starting around  $P/P_0 = 10^{-1}$  due to pore filling. The calculated Brunauer-Emmett-Teller (BET) surface area was found to be  $2497 \text{ m}^2 \text{ g}^{-1}$  while the Langmuir model gave a surface area of  $3832 \text{ m}^2 \text{ g}^{-1}$  that is similar to the calculated Connolly surface ( $4973 \text{ m}^2 \text{ g}^{-1}$ ). The experimental surface area values are considerably higher than those reported for the analogous COF-5:  $SA_{BET} = 2050 \text{ m}^2 \text{ g}^{-1}$   $SA_{LANG} = 3300 \text{ m}^2 \text{ g}^{-1}$ .<sup>86</sup>

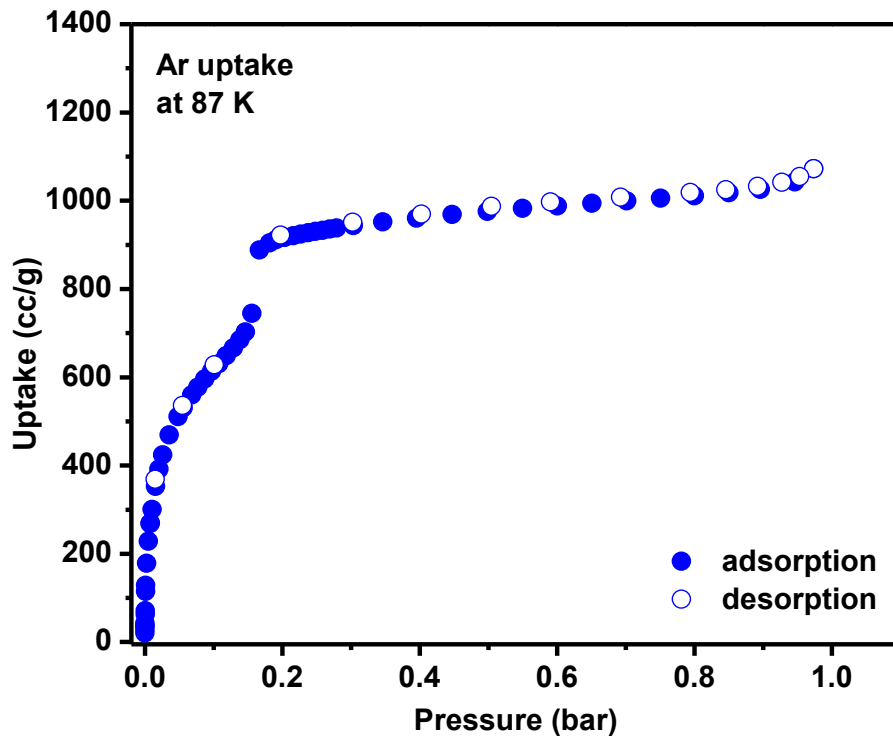


**Figure 2.6:** Argon adsorption isotherm for TDCOF-5 measured at 87 K. The filled circles are adsorption points and the empty circles are desorption points.



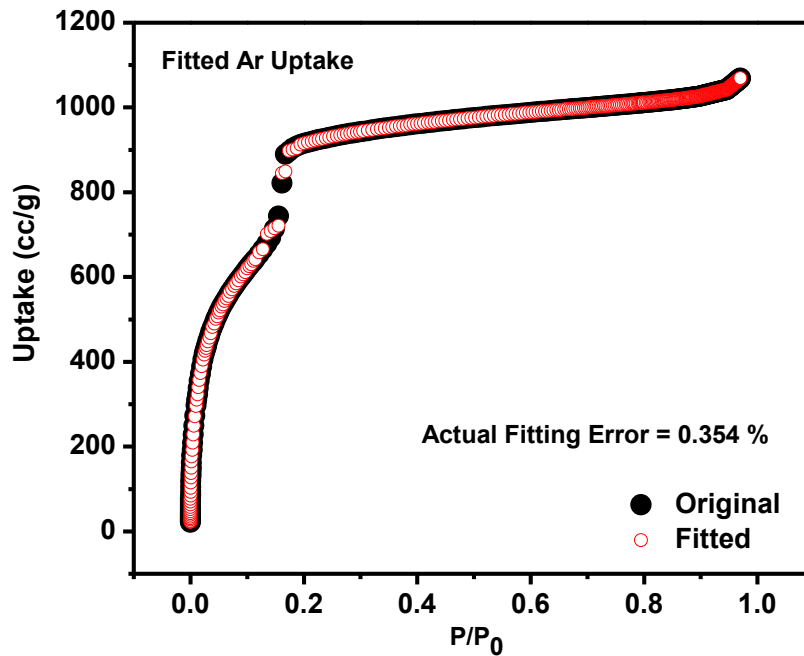


**Figure 2.7:** Experimental Ar adsorption isotherm for TDCOF-5 measured at 87 K is shown as filled circle. The calculated NLDFT isotherm is overlaid as open circle. Note that a fitting error of less than 1% indicates the validity of using this method for assessing the porosity of TDCOF-5. The fitting error is indicated.

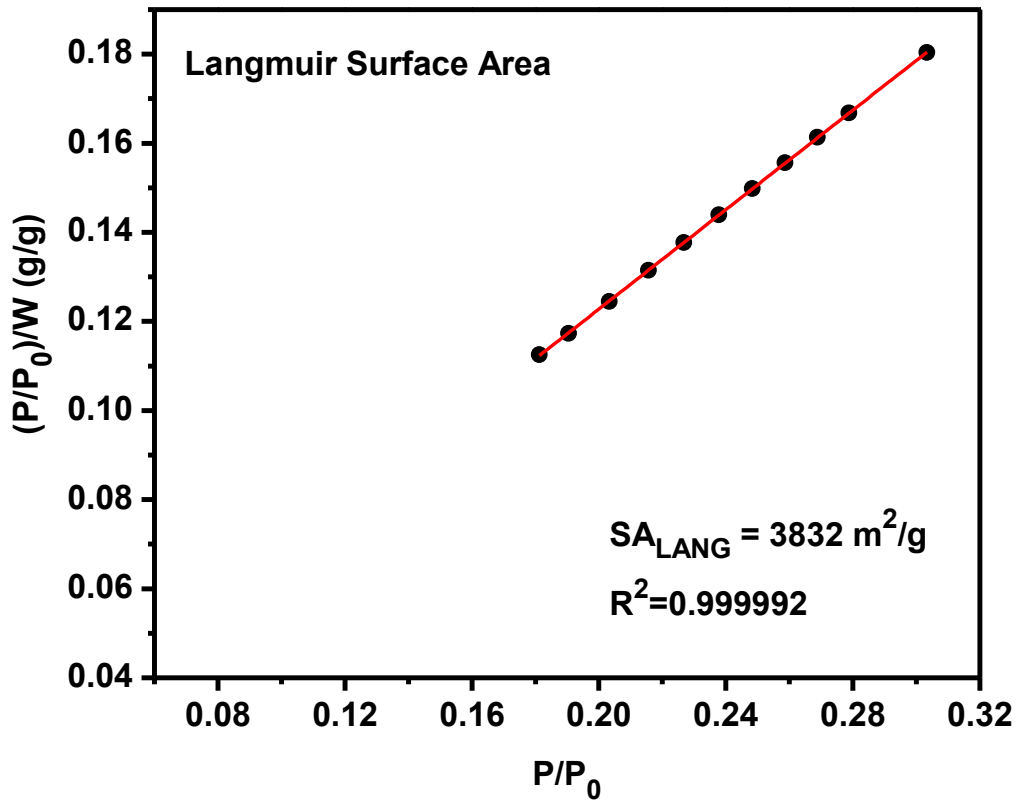


**Figure 2.8:** Langmuir plot for TDCOF-5 calculated from the Ar adsorption isotherm at 87 K.

The model was applied from  $P/P_0 = 0.17-0.30$ . The correlation factor is indicated. ( $W =$  Weight of gas absorbed at a relative pressure  $P/P_0$ ).

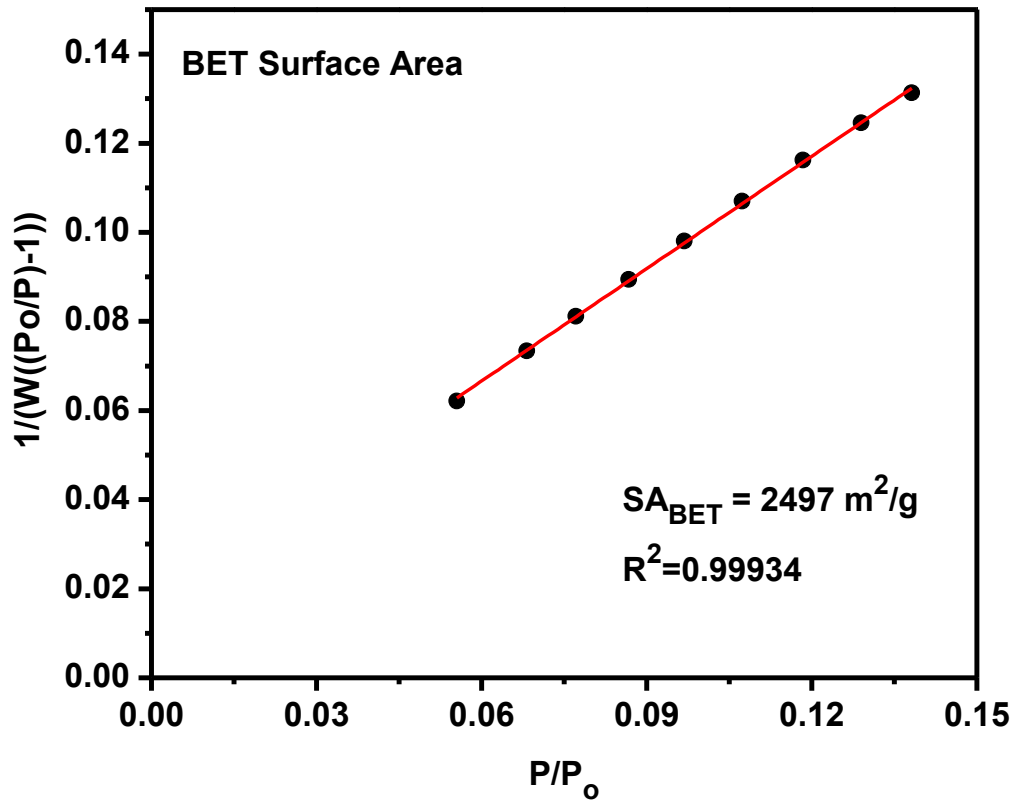


**Figure 2.9:** BET plot for TDCOF-5 calculated from the Ar adsorption isotherm at 87 K. The model was applied from  $P/P_0 = 0.05-0.15$ . The correlation factor is indicated. (W= Weight of gas absorbed at a relative pressure  $P/P_0$ ).

Pore size distribution (PSD) was estimated from non-local density functional theory (NLDFT) calculations (Figure 2.10) and found to be centered at about 26 Å and somewhat smaller than the predicted pore aperture of the eclipsed model (31 Å), while the pore volume at  $P/P_0 = 0.95$  was 1.3 cc g<sup>-1</sup>. This discrepancy may arise from imperfect solid-state stacking of the eclipsed 2D sheets as reported for many 2D COFs and predicated by theoretical studies. In contrast to 2D COFs that employ electron-rich building units and assemble into eclipsed structures driven by the strong  $\pi$ - $\pi$  interactions, the use of the triptycene core in TDCOF-5 leads to more accessible boron sites that can facilitate interaction with gas molecules. For example, COF-10 exhibits a remarkably high NH<sub>3</sub> uptake driven by the interactions between NH<sub>3</sub> and the boron sites.<sup>62</sup> Furthermore, reducing the number of latent edges of molecular building units in porous architectures can provide additional gas interaction sites and is believed to enhance adsorptive gas storage.<sup>77</sup>

### 2.3.3 Gas Storage Studies of TDCOF-5

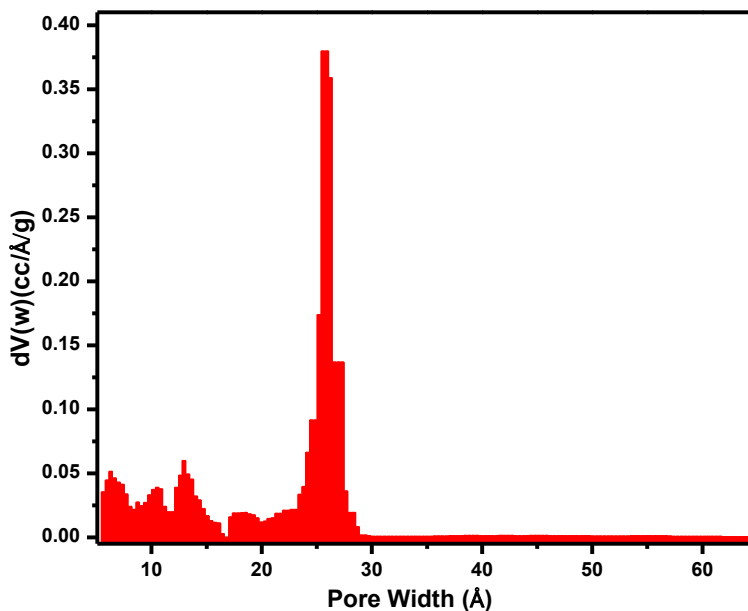


**Figure 2.10:** Pore Size Distribution (PSD) for TDCOF-5 using the NLDFT model.

Hydrogen isotherms have been collected at 77 K and 87 K (Figure 2.11) and the hydrogen isosteric heat of adsorption ( $Q_{st}$ ) calculated by using the virial method<sup>87</sup>. The H<sub>2</sub> uptake at 77 K/1.0 bar (1.6 wt. %) is the highest among all known 2D and 3D COFs<sup>80</sup> derived from B-O bond formation and almost double the uptake of COF-5 (0.9 wt. %),<sup>86</sup> it is also comparable to those of porous organic polymers and other COFs.<sup>15</sup>

We collected CH<sub>4</sub> and CO<sub>2</sub> isotherms at 273 K and 298 K (Figure 2.12-13) to mainly investigate the binding affinity for these gases. Methane is abundant and has low carbon footprint, whereas CO<sub>2</sub> capture from flue gas is highly desirable to capture because of the greenhouse effect of CO<sub>2</sub>. At 273 K and 1.0 bar, TDCOF-5 can store up to 9.2 wt. % (2.1 mmol g<sup>-1</sup>) of CO<sub>2</sub> and 11.5 cc g<sup>-1</sup> of CH<sub>4</sub> with respective  $Q_{st}$  values of 21.8 and 12.6 kJ mol<sup>-1</sup>. Again, it is worth mentioning that the CO<sub>2</sub> uptake is higher than those of reported COFs and only exceeded by the uptake of COF-6 which has much narrower channels (9 Å), but lower than the uptakes and binding affinities of functionalized porous organic polymers such as BILPs<sup>46-48</sup>, POFs<sup>67</sup> and PPNs<sup>88</sup>. The methane uptake at 273 K/1.0 bar (16 cc g<sup>-1</sup>) was compared to data available for COFs; COF-10 (8.0 cc g<sup>-1</sup>) and COF-102(14 cc g<sup>-1</sup>).<sup>86</sup>

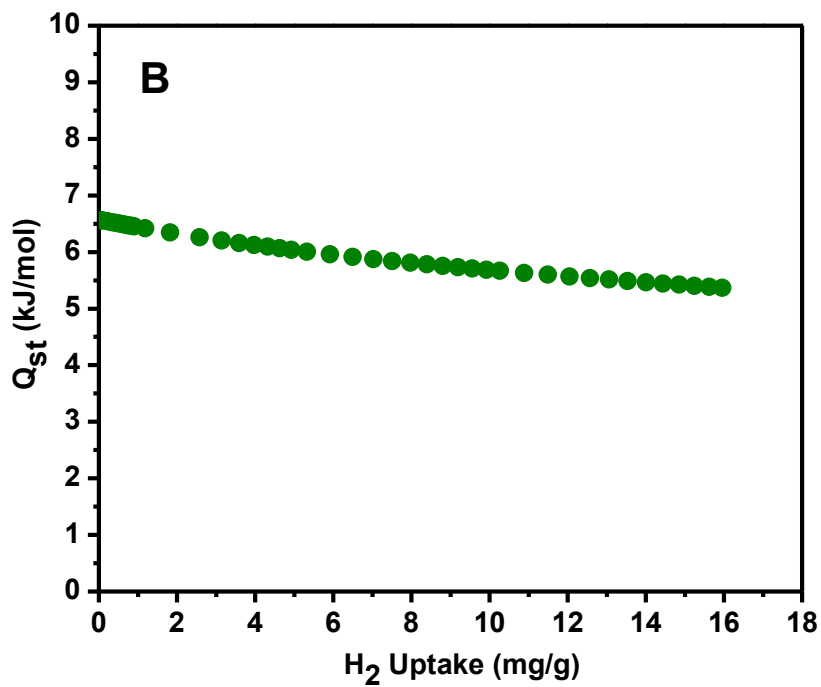
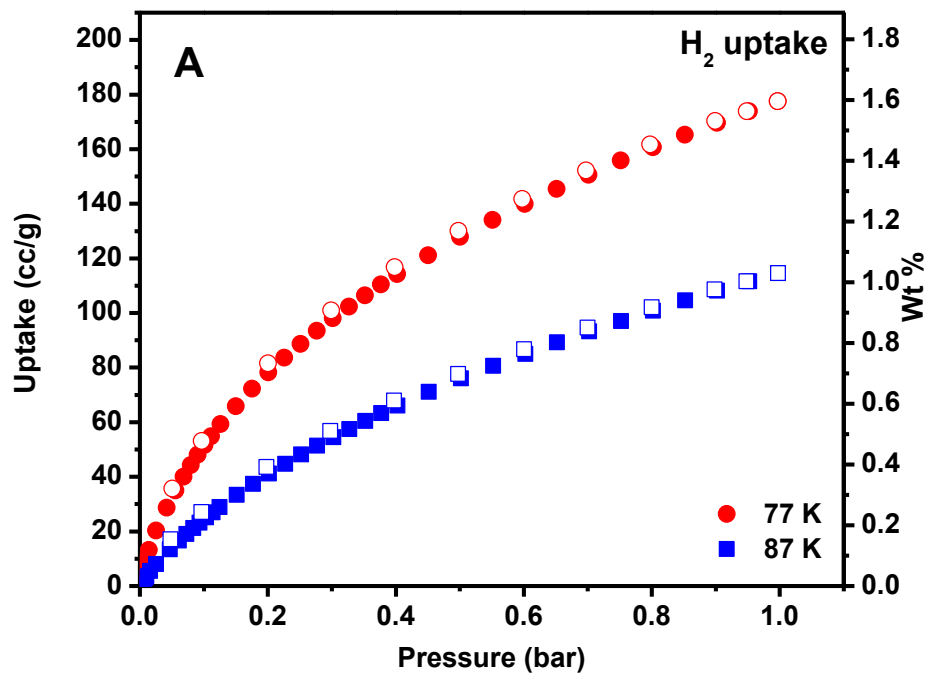


**Figure 2.11:** A) Hydrogen isotherm for *TDCOF-5* measured at 77K and 87K. B) Hydrogen isosteric heat of adsorption ( $Q_{st}$ ) for *TDCOF-5*.

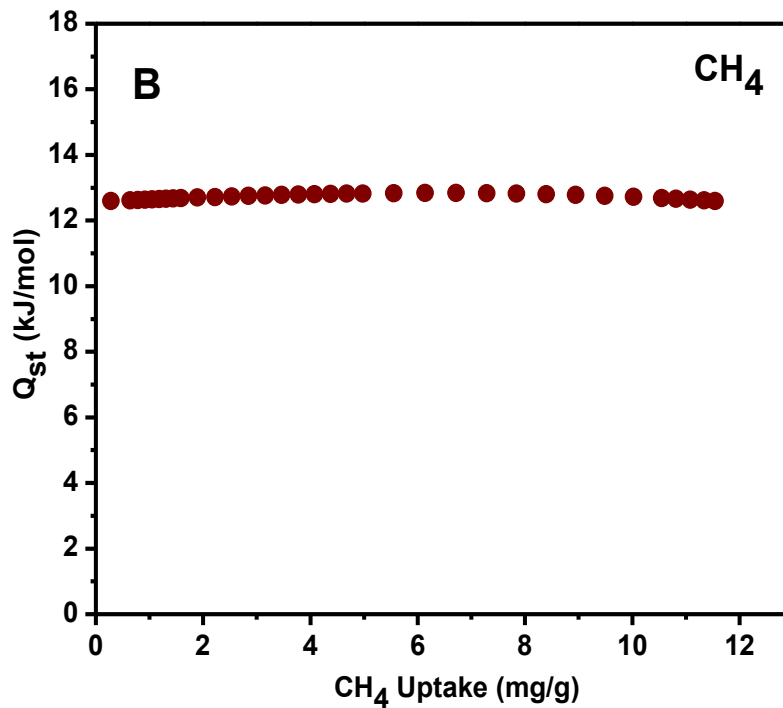
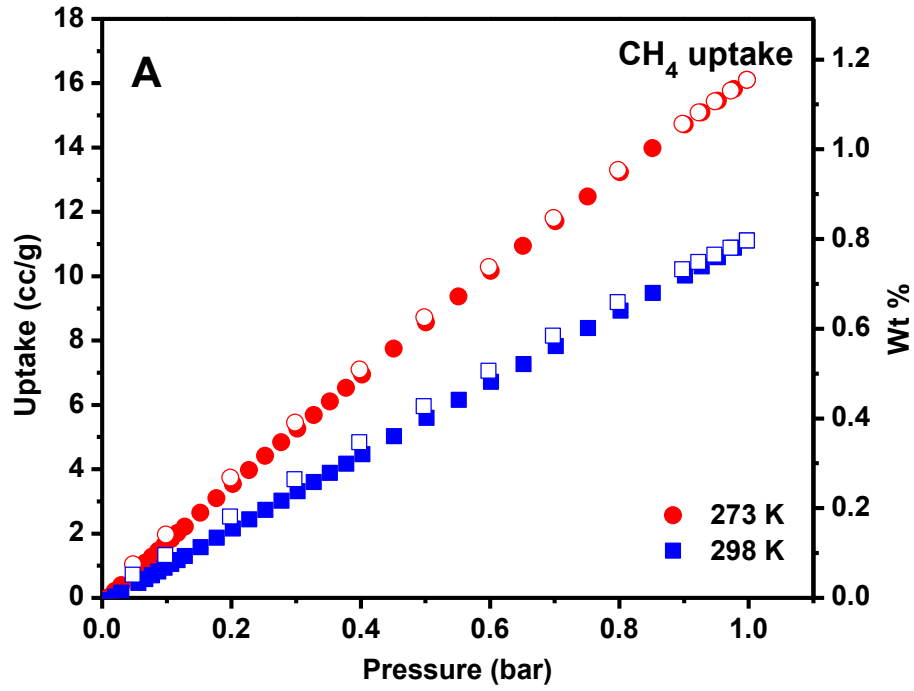


**Figure 2.12:** A) Methane isotherm for *TDCOF-5* measured at 273K and 298K. B) Methane isosteric heat of adsorption ( $Q_{st}$ ) for *TDCOF-5*.

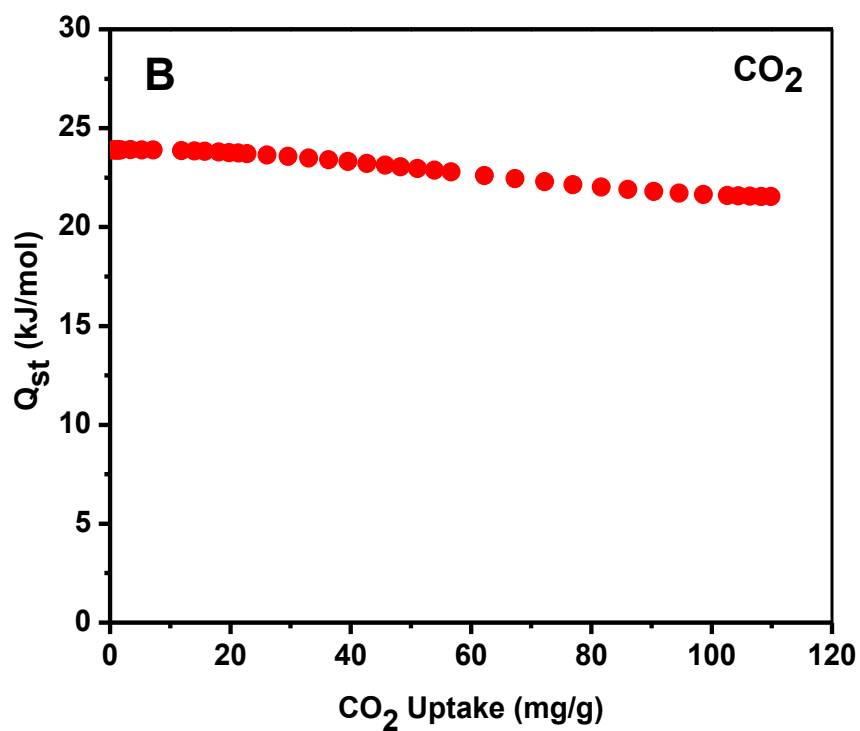
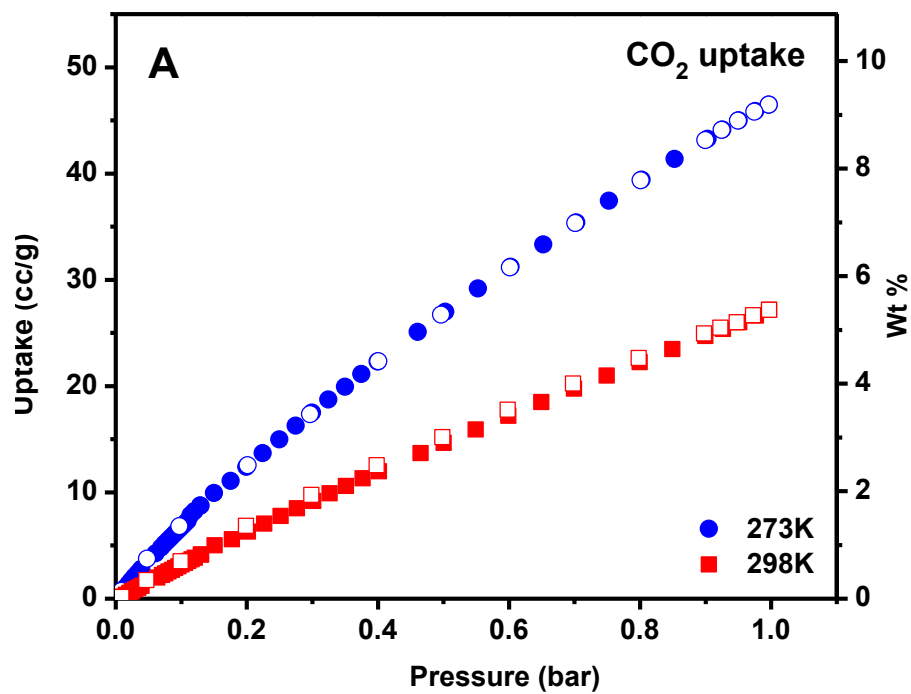


**Figure 2.13:** A) Carbon dioxide isotherm for *TDCOF-5* measured at 273K and 298K. B)

Carbon dioxide isosteric heat of adsorption ( $Q_{st}$ ) for *TDCOF-5*.



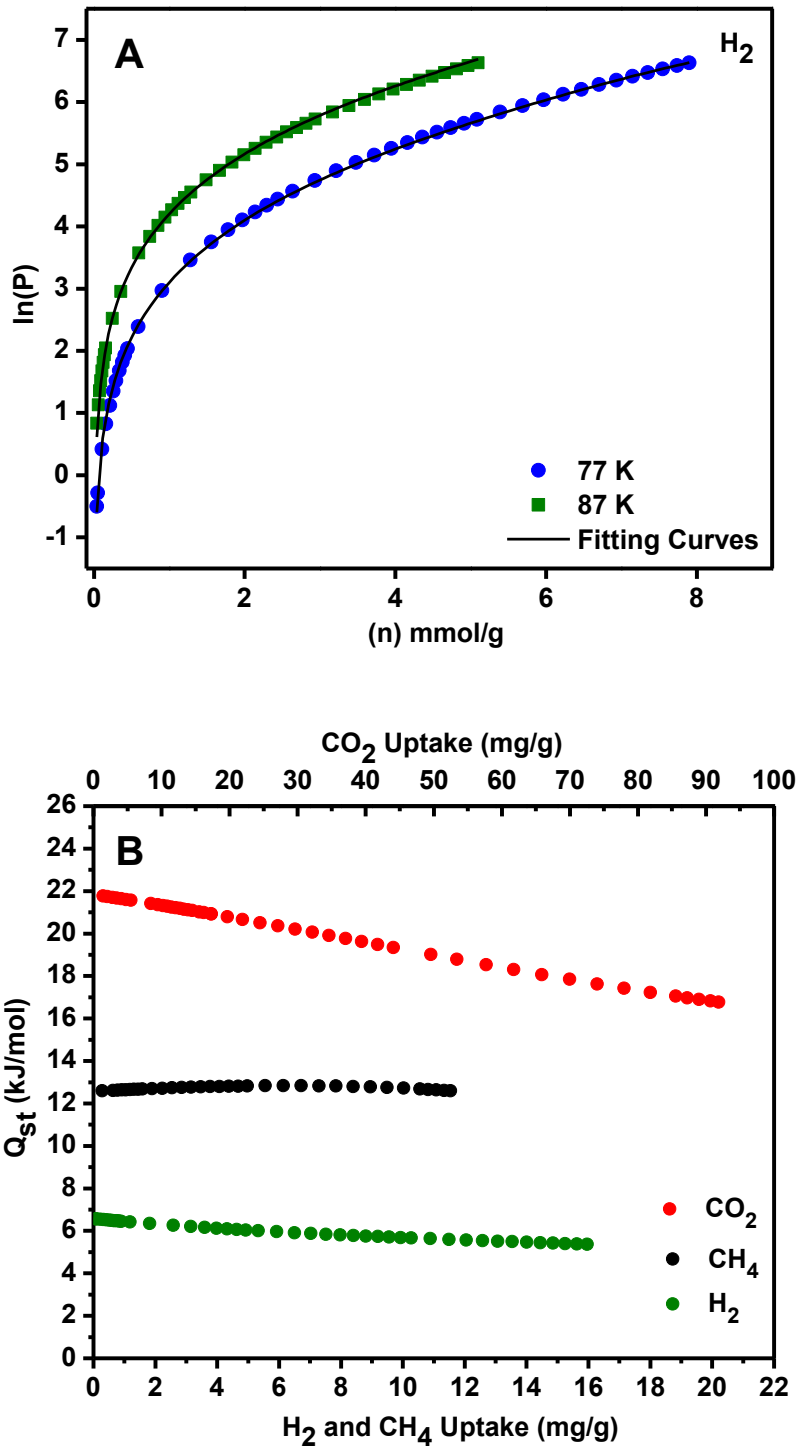


**Figure 2.14:** A) Virial analysis of  $H_2$  adsorption data for *TDCOF-5*. B) Combined isosteric heat of adsorption ( $Q_{st}$ ) for *TDCOF-5*.

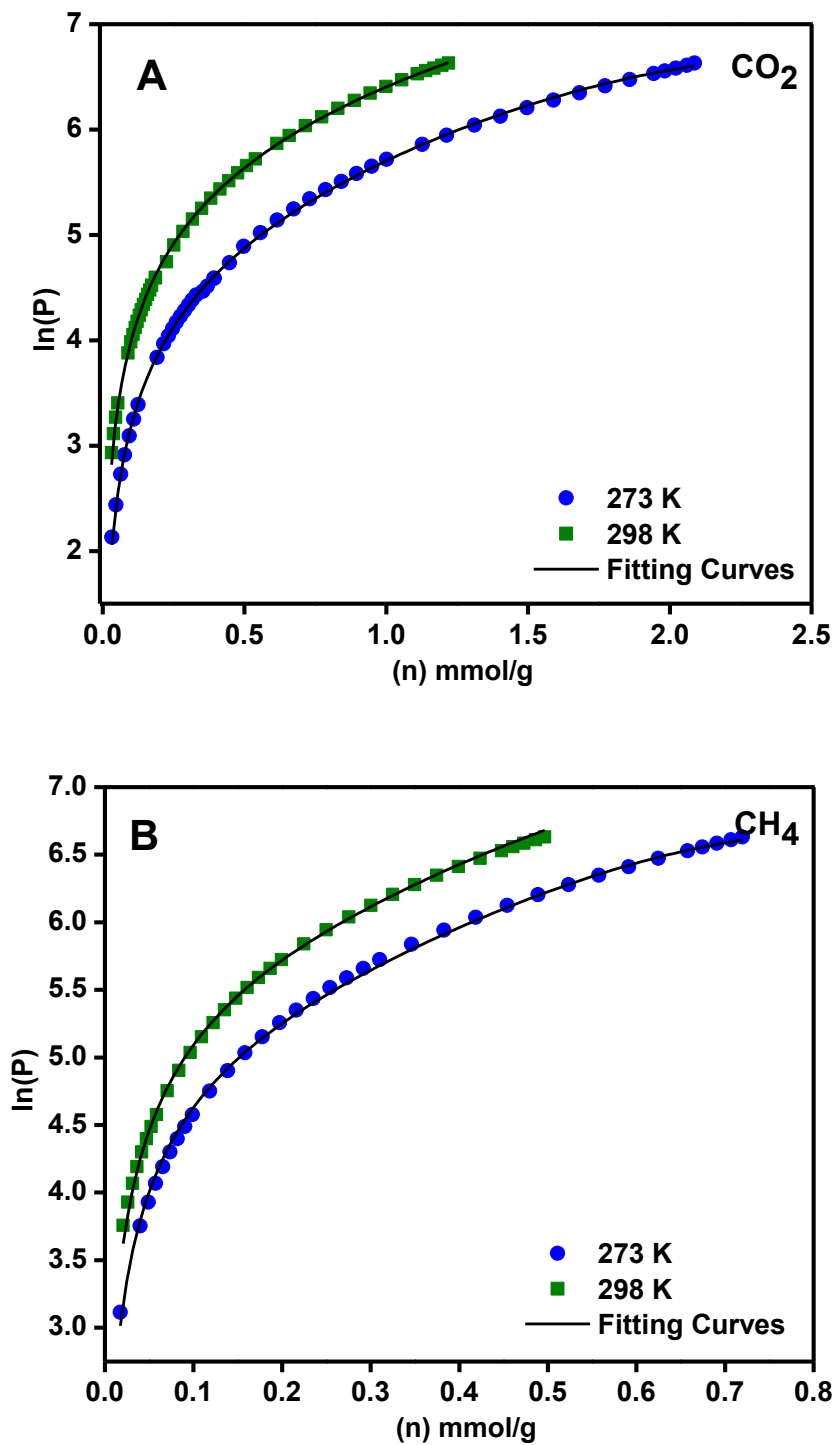


**Figure 2.15:** Virial analysis of A) CO<sub>2</sub> and B) CH<sub>4</sub> adsorption data for TDCOF-5

The  $Q_{st}$  value for hydrogen (Figure 2.14) at low coverage was found to be  $6.6 \text{ kJ mol}^{-1}$  which is within the range of 2D COFs ( $6.0\text{-}7.0 \text{ kJ mol}^{-1}$ )<sup>89</sup> and other organic polymers. The uptake by TDCOF-5 is almost double that of COF-10 and exceeds the uptake of COF-102 even though the latter has a higher surface area and much narrower channels ( $\sim 12 \text{ \AA}$ ) which typically favor methane storage at low pressure. The calculated  $Q_{st}$  for methane at low coverage was found to be  $12.6 \text{ kJ mol}^{-1}$  which is only exceeded by the affinities of COF-6 and COF-1 (pore width  $\sim 9 \text{ \AA}$ ); this enhanced binding affinity can be one of the reasons behind the high methane uptake observed for TDCOF-5. The above discussed adsorptive gas properties of TDCOF-5 are consistent with our recent DFT calculations which revealed that  $\text{H}_2$ ,  $\text{CH}_4$ , and  $\text{CO}_2$  molecules favor interaction with boron-containing heterocyclic building units over phenyl moieties in organic polymers.<sup>90</sup>

### 2.3.3.1 Calculation of Isothermic Heats of Adsorption for TDCOF-5

The virial equation was used to determine the binding affinity and isothermic heats of adsorption. The virial equation is given as: <sup>91</sup>

$$\ln\left(\frac{N}{P}\right) = A_0N^0 + A_1N^1 + A_2N^2 + \dots \quad \text{(I)}$$

Where  $N$  is the amount adsorbed at pressure  $P$  and  $A_0, A_1$ , etc. are virial coefficients.  $A_0$  is related to adsorbate-adsorbent interactions, whereas  $A_1$  describes adsorbate-adsorbate interactions. Under condition of low surface coverage, the higher terms ( $A_2$ , etc.) in the virial equation can be neglected.

A virial-type expression in the following form can also be used to fit the experimental isotherm data for a given material at different temperatures. <sup>87</sup>

$$\ln(P) = \ln(N) + \frac{1}{T} \sum_{i=0}^m a_i N^i + \sum_{i=0}^n b_i N^i \quad \text{(II)}$$

Where  $N$  is the amount adsorbed at pressure  $P$ ,  $T$  is the temperature,  $a_i$  and  $b_i$  are temperature independent empirical parameters, and  $m$  and  $n$  determine the number of terms required to adequately describe the isotherm. The resulting virial coefficients  $a_0$  through  $a_m$  can then be used to calculate the isothermic heats of adsorption as function of uptake:

$$Q_{st} = -R \sum_{i=0}^m a_i N^i \quad \text{(III)}$$

Where  $R$  is the universal gas constant (8.314 J K<sup>-1</sup> Mol<sup>-1</sup>)

It follows that the zero-coverage isothermic heats of adsorption is given by

$$Q_{st} = -Ra_0 \quad \text{(IV)}$$

### 2.3.4 Structural Models and Atomic Coordinates for TDCOF-5

The structure of TDCOF-5 was investigated by a combination of powder x-ray diffraction (PXRD) and material modelling studies. The experimental PXRD pattern (Figure 2.16) confirms the formation of a microcrystalline material. Given the rigid and tritopic nature of hexahydroxytritycene, its copolymerization with 1,4-benzenediboronic acid would lead to 2D networks having hexagonal channels that can stack in either eclipsed (AA, P6/mmm) or staggered (AB, P6<sub>3</sub>/mmc) conformations.<sup>1</sup> As such, we constructed two models following methods reported for 2D COFs using Materials Studio Visualizer and optimized their geometries and energies by the Forcite module.<sup>92</sup> From the data presented in (Figure 2.17), it is clear that TDCOF-5 crystallizes into an eclipsed arrangement similar to those of 2D COFs that employ electron rich building units such as triphenylene pyrene, and porphyrins.<sup>73</sup> As shown in Figure 4, the calculated diffraction pattern of the eclipsed model which in this case is based on P6/mmm space group matches well with that of TDCOF-5 and is in sharp contrast to the calculated pattern of the staggered model (P6<sub>3</sub>/mmc). The latter conformation results in an intense reflex at  $2\theta = 7.06^\circ$  that corresponds to the (101) plane which is absent from the experimental PXRD pattern of TDCOF-5. The powder-XRD pattern was subjected to refinement by the Rietveld<sup>93</sup> method and produced lattice parameters of  $a = b = 29.7042 \text{ \AA}$  and  $c = 7.4121 \text{ \AA}$ ; these numbers agree well with the values of the theoretical eclipsed conformation ( $a = b = 31.3283 \text{ \AA}$  and  $c = 7.5183 \text{ \AA}$ ). The  $wRp$  and  $Rp$  values converged to 2.80% and 2.04%, respectively. The general broadening of the PXRD reflections is most likely due to deviation from the ideal eclipsed stacking of the 2D layers. Such interactions have been suggested to lead to small offsets (1.5-2.8  $\text{\AA}$ ) that cannot be measured by X-ray diffraction studies. The d-spacing (7.4121  $\text{\AA}$ ) between the 2D layers is considerably larger

than those reported for eclipsed 2D COF structures derived from the hexahydroxytriphenylene unit as a result of the non-coplanar conformation of the triptycene core.

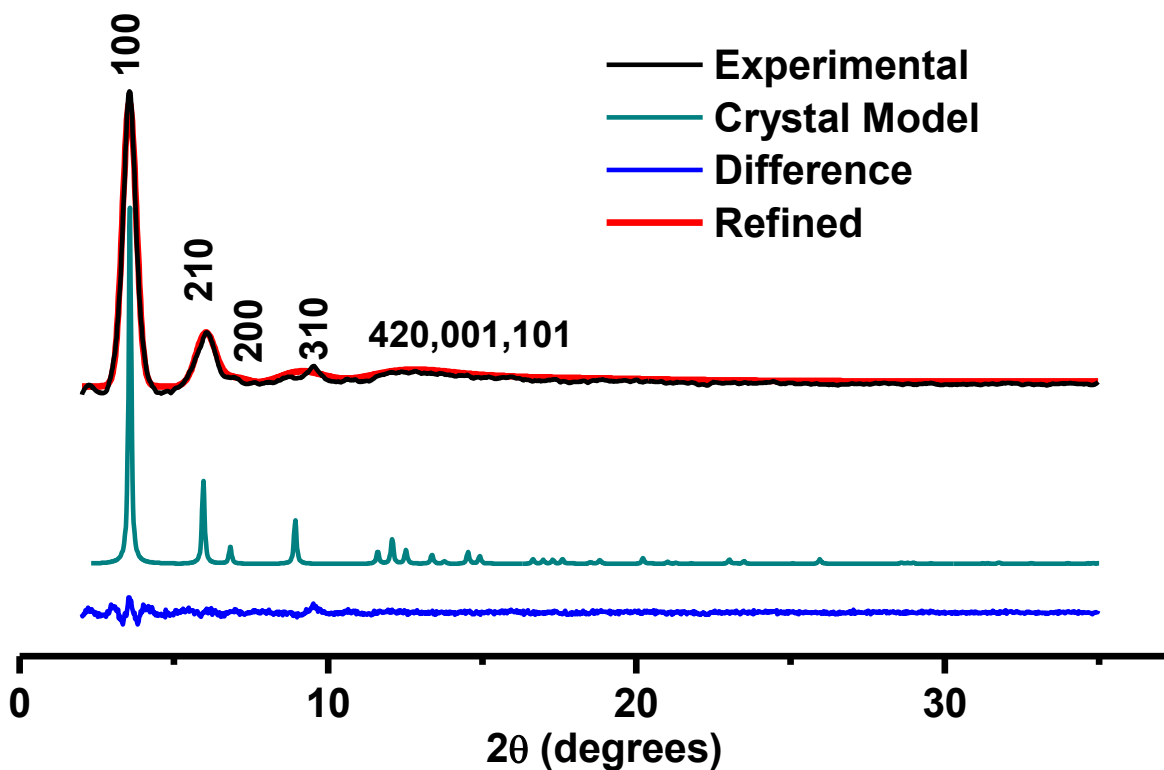


**Figure 2.16:** PXRD pattern of *TDCOF-5* with the experimental pattern in black, the Reitveld refined profile in red, the difference plot in blue and the eclipsed crystal model is green.

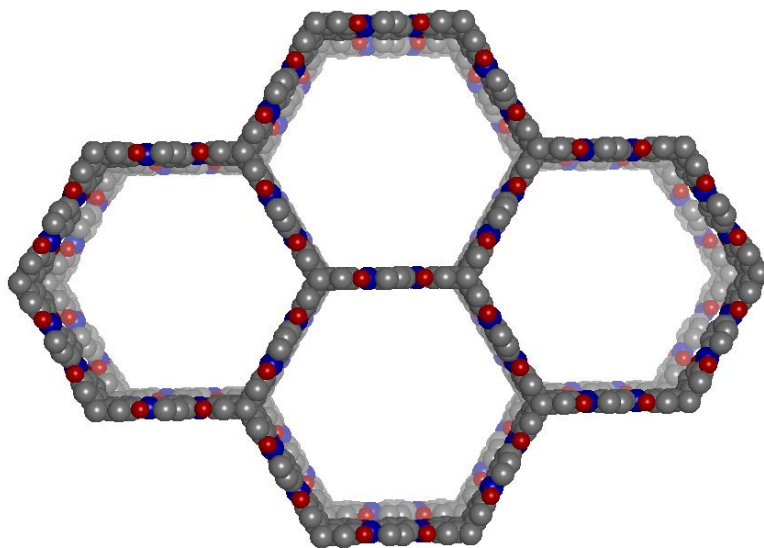
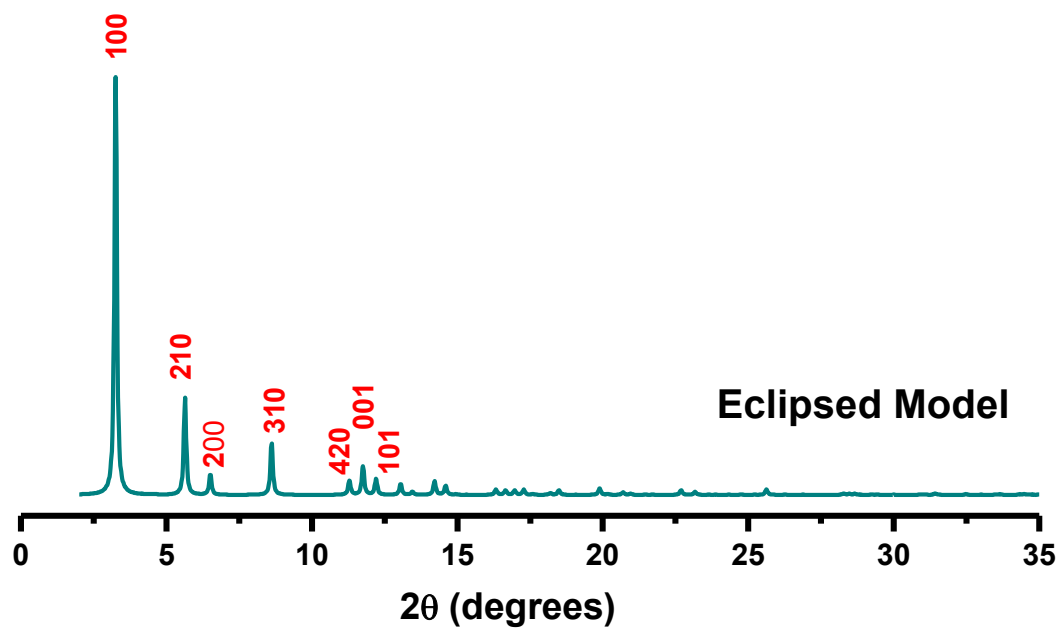


**Figure 2.17:** Eclipsed PXR D pattern of *TDCOF-5*

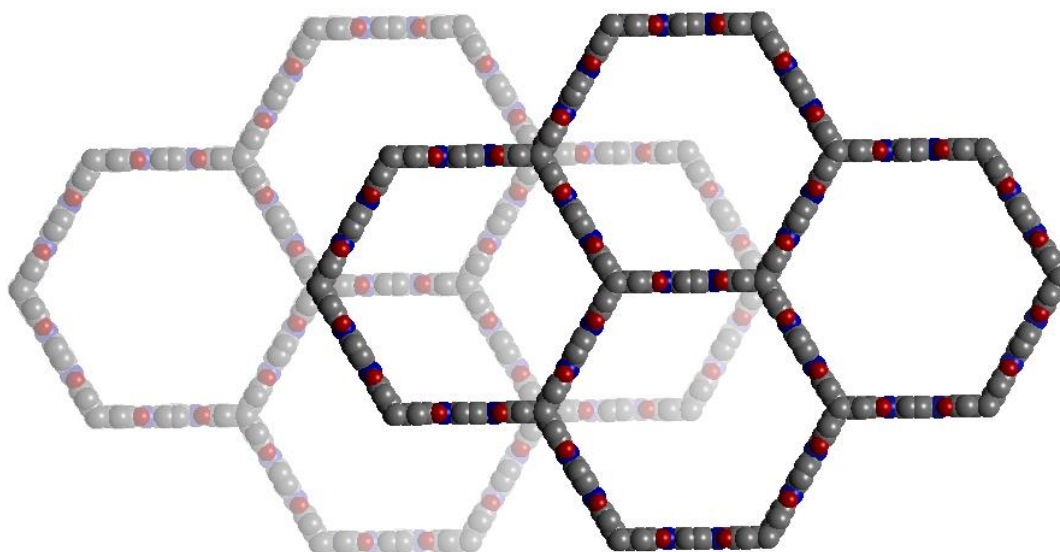
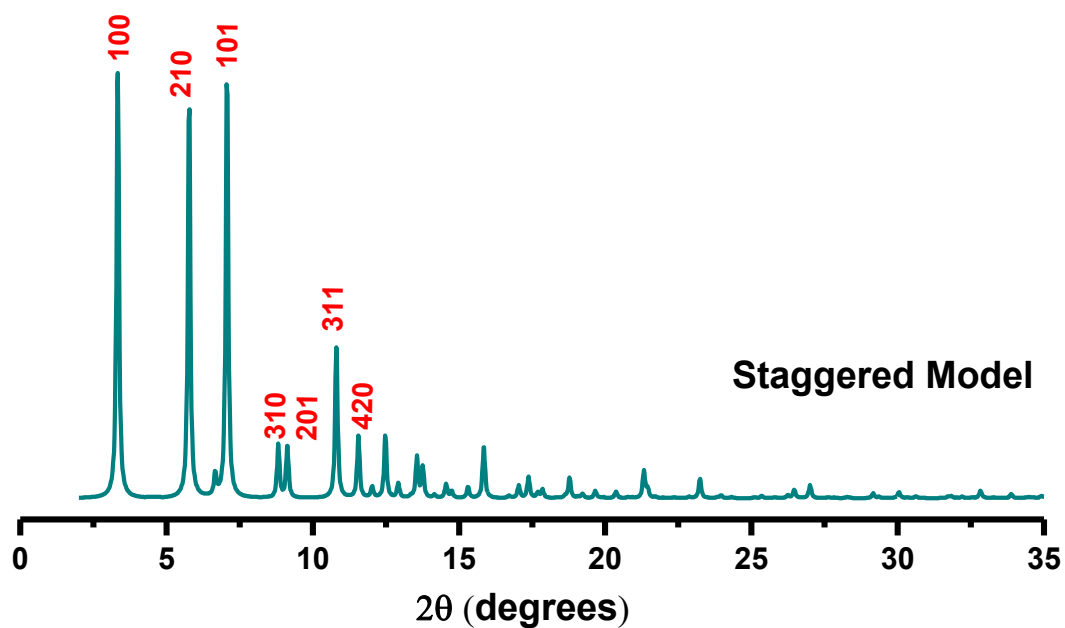


**Figure 2.18:** Staggered PXR D pattern of *TDCOF-5*.



*TDCOF-5* model was constructed using *Materials Studio Visualizer*<sup>92</sup> utilizing the Forcite module. The eclipsed conformation for polymer was modeled using boron nitride space group (*P6/mmm*) and staggered conformation was modeled using with a graphite topology of space group (*P6<sub>3</sub>/mmc*). Vertex positions were obtained from the Reticular Chemistry Structure Resource<sup>94</sup>. The vertices were replaced by a triptycene with the  $\text{BO}_2\text{C}_2$  ring pointing along the extension. The midpoint of each extension was replaced by benzene for *TDCOF-5*.

The positions of atoms in the unit cell were determined using *CrystalMaker for Windows Version 1.4.5* and are shown as fractional atomic coordinates in Tables 2.1-2-3.

**Table 2.1:** Fractional atomic coordinates for the refined unit cell parameters for *TDCOF-5* calculated from GSAS and EXP-GUI software packages.

Refined			
<i>Hexagonal</i>			
$a = b = 30.5978 \text{ \AA} ; c = 14.1705 \text{ \AA}$			
$\alpha = \beta = 90^\circ ; \gamma = 120^\circ$			
	X	Y	Z
B1	0.557	0.443	1
C1	0.2816	0.6408	0.1028
C2	0.2333	0.6167	-0.1992
C3	0.1906	0.5953	-0.097
C4	0.3333	0.6667	0.1868
C5	0.486	0.514	1.1768
C6	0.5278	0.4722	1.000
H1	0.2318	0.6159	0.3427
H2	0.3333	0.6667	-0.3344
H3	0.4759	0.5241	1.3052
O1	0.1431	0.5716	-0.1646

**Table 2.2:** Fractional atomic coordinates for the staggered conformation of *TDCOF-5* calculated from *Materials Studio* modeling.

Graphite			
<i>P6<sub>3</sub>/mmc</i>			
a = b = 30.5978 Å ; c = 14.1705 Å			
$\alpha = \beta = 90^\circ ; \gamma = 120^\circ$			
Hexagonal			
	X	Y	Z
B1	0.22270	0.44540	0.25000
B2	0.88939	0.77879	0.75000
C1	0.30706	0.61412	0.30043
C2	0.30692	0.15346	0.83552
C3	0.38637	0.19318	0.75000
C4	0.28024	0.14012	0.75000
C5	0.97373	0.94745	0.80041
C6	0.33333	0.66666	0.34456
C7	0.43139	0.71570	0.14921
C8	0.47625	0.73813	0.20115
C9	0.00000	0.00000	0.84436
C10	0.09803	0.04901	0.64916
C11	0.14288	0.07144	0.70114
C12	0.35969	0.17984	0.83551
H1	0.33333	0.66666	0.42300
H2	0.43190	0.71595	0.07285
H3	0.00000	0.00000	0.92231
H4	0.09851	0.04926	0.57278
H5	0.37950	0.18975	0.90240
H6	0.28710	0.14355	0.90240
O1	0.23778	0.47556	0.16330
O2	0.90447	0.80893	0.66330

**Table 2.3:** Fractional atomic coordinates for the eclipsed conformation of *TDCOF-5* calculated from *Materials Studio* modeling.

Boron Nitride			
<i>P6/mmm</i>			
a = b = 31.3283 Å ; c = 7.51830 Å			
$\alpha = \beta = 90^\circ ; \gamma = 120^\circ$			
Hexagonal			
	X	Y	Z
B	0.55701	0.44299	1.00000
C1	0.28159	0.64080	0.10278
C3	0.19057	0.59528	-0.09697
C4	0.33333	0.66666	0.18683
C5	0.48599	0.51401	1.17676
C6	0.52779	0.47221	1.00000
H1	0.23176	0.61588	-0.34269
H2	0.33330	0.66666	-0.33441
H3	0.47588	0.52412	1.30519
O5	0.14311	0.57156	-0.16455

## 2.4. Conclusion

The synthesis and characterization of a highly porous triptycene-derived covalent organic framework (TDCOF-5) and its performance in small gas storage are reported. TDCOF-5 crystallizes into a 2D mesoporous network that contains accessible boron sites, exhibits high surface area ( $SA_{Lang} = 3832 \text{ m}^2 \text{ g}^{-1}$ ), and enhanced gas uptake properties under low pressure settings. We have demonstrated that integrating triptycene into the backbone of COFs can significantly enhance their porosity and performance in small gas storage. These attributes are most likely driven by the ability of triptycene to reduce  $\pi$ - $\pi$  interactions between the building units and thereby render the boron sites more accessible for interaction with gas molecules.

## Chapter 3

### Synthesis and Characterization of Porous Diazaborole-Linked Polymers

#### 3.1 Introduction

The synthesis of porous organic polymers has attracted significant attention due to their potential in various applications including gas storage and separation, conductivity, catalysis, electronics, and chemical sensing.<sup>1, 2</sup> Among these polymers are Covalent Organic Frameworks (COFs) of which the structure, metrics, and functionality can be systematically tailored. COFs are purely organic structures and consist of light elements such as C, B, O, and H which are connected via strong covalent bonds. The dynamic nature of the B-O bond in COFs results in microcrystalline structure; however, it renders them prone to hydrolysis, which leads to the loss of porosity. Boron-nitrogen bonds are known to be more stable compared to other derivatives because nitrogen's lone pair electrons have the ability to conjugate with the vacant p-orbital of the boron atom.<sup>63-65</sup> In addition to increasing bond stability, accessible nitrogen or amine functionalities on the pore walls either through the selection of pre-functional building blocks or use of post-modification methods can considerably enhance CO<sub>2</sub> uptake.<sup>66, 67</sup> Recently our group has synthesized benzimidazole linked polymers (BILPs) which have accessible nitrogen sites on the pore walls, resulting in high gas affinity (up to 5.35 mmol g<sup>-1</sup> CO<sub>2</sub> at 273 K and 1 bar). This motivated us to synthesize crystalline porous polymer via B-N bond formation; unfortunately, covalently linked polymers in general lack long-range ordering and tend to be amorphous due to irreversible bond formation.

Keeping these key considerations in mind, we have designed and synthesized a new class of porous organic polymer dubbed diazaborole-linked polymers (DBLPs). DBLPs were prepared by

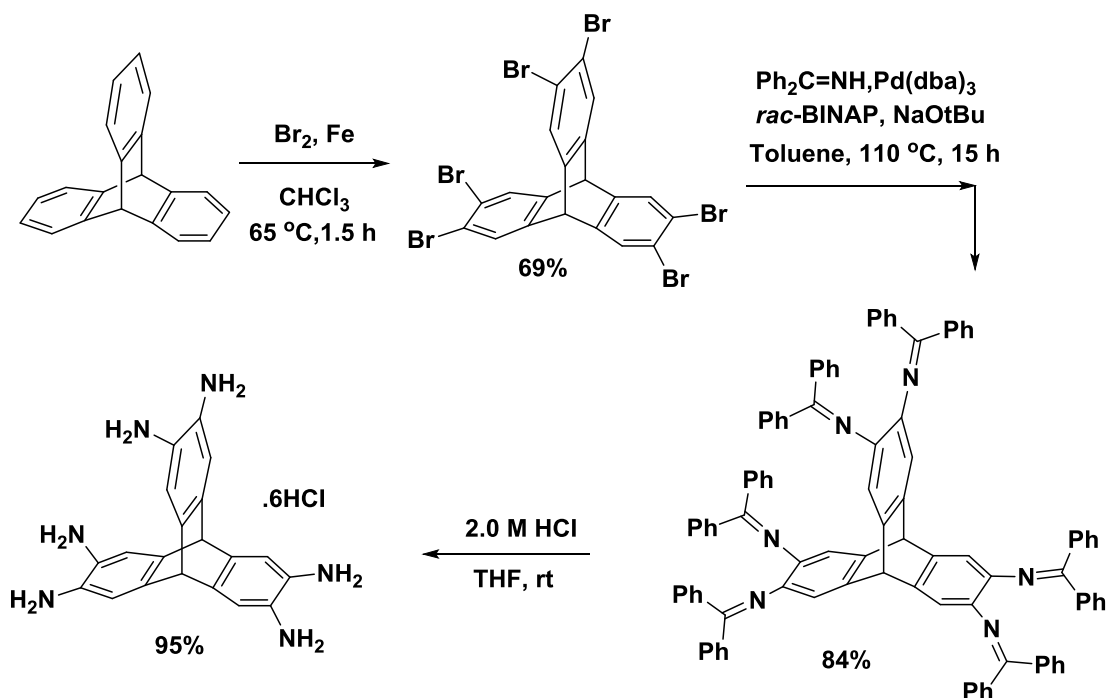
a metal-free polymerization process and are the first examples of porous polymer networks linked by diazaborole rings, which leads to auto-functional pore walls throughout the polymer structure. DBLPs show high CO<sub>2</sub> and H<sub>2</sub> uptake at ambient pressure and temperature, high CO<sub>2</sub> selectivity over N<sub>2</sub> and CH<sub>4</sub> as well as high thermal and chemical stability. High CO<sub>2</sub> uptake may arise from sub-nanometer pore structures and diazaborole functionalized pore walls. The strong CO<sub>2</sub> affinity arises from hydrogen bonding<sup>9</sup> between N-H of the polymer framework and CO<sub>2</sub>'s oxygen, as well as dipole-quadrupole interactions between the CO<sub>2</sub> and pore walls. We investigated the DBLPs performance in small gas uptake such as N<sub>2</sub>, CH<sub>4</sub>, and CO<sub>2</sub> under low pressure conditions.

### 3.1 Experimental Section

#### 3.1.1 Materials and Methods

All starting materials, unless noted otherwise, were obtained from Acros Organics and used without further purification. Benzene-1, 4-diboronic acid (BDBA), triptycene, chloroform (stabilized with amylene) and *N,N*-dimethylformamide (DMF) were purchased from Aldrich Chemical Co. and used without further purification. Solvents were dried by distillation from Na (toluene) or Na/benzophenone (THF). 1,3,5-benzenetriboronic acid (BTBA)<sup>95, 96</sup> and 2,3,6,7,14,15-hexaaminotriptycene (HATT)<sup>47</sup> (Scheme 3.1) were synthesized according to published methods. All products were handled under a nitrogen atmosphere using glovebox or Schlenk line techniques. Chromatographic separations were performed using standard column chromatography methods using silica gel purchased from Acros Organics (60 Å, 35-70 µm). Solution <sup>1</sup>H and <sup>13</sup>C NMR spectra were obtained on a Varian Mercury-300 MHz NMR spectrometer. Elemental analyses were performed by Midwest Microlab, Indianapolis, IN. Higher carbon and hydrogen contents may result from residual hydrocarbons in the cavities. FT-IR spectra

were obtained using a Nicolet-Nexus 670 spectrometer equipped with Smart iTR™. Representative solid-state nuclear magnetic resonance (NMR) spectra were recorded at ambient temperature on a Bruker DSX-300 spectrometer using a Bruker magic angle spinning (MAS) probe with 4 mm (O.D.) 80  $\mu$ L volume zirconia rotors with Kel-F drive caps at Spectral Data Services, Inc. SEM samples were prepared by dispersing the material onto a sticky carbon surface attached to a flat aluminum sample holder. The samples were then platinum coated using an EMS (Electron Microscopy Sciences) 550x Sputter Coater at  $1 \times 10^{-1}$  mbar of pressure in a nitrogen atmosphere for 90 seconds while maintaining 20 mA of current. Samples were analyzed on a Zeiss EVO XVP Scanning Electron Microscope using the SEI detector with accelerating voltages ranging from 10 kV to 20 kV. Powder X-ray diffraction data were collected on a Panalytical X'pert pro multipurpose diffractometer (MPD). Samples were mounted on a sample holder and measured using Cu K $\alpha$  radiation with a  $2\theta$  range of 1.5-35. Thermogravimetric analysis was obtained using a TA Instruments TGA Q5000 analyzer with 50  $\mu$ L platinum pans to assess the thermal stability of the polymer. Experiments were run at a ramp rate of 5 K/minute under a nitrogen atmosphere. Argon sorption experiments were run using a Quantachrome Autosorb iQ2 analyzer. In a typical experiment, a sample was loaded into a 9 mm large bulb cell (Quantachrome) of known weight and then hooked up to Autosorb IQ2 and degassed at 120 °C for 12 h. The degassed sample was refilled with nitrogen, weighed and then transferred back to the analyzer. The temperatures for adsorption measurements were controlled by using bath of liquid nitrogen (77 K), liquid argon (87 K), or temperature controlled water bath (273 K and 298 K). Hydrogen isotherms were collected at 77 K and 87 K. Carbon dioxide and methane isotherms were collected at 273 K and 298 K. Pore Size Distribution (PSD) was calculated using spherical/cylindrical pore (zeolite) NLDFT adsorption model.<sup>83</sup>



**Scheme 3.1:** Overall synthesis of hexahydroxytryptycene and hexaaminotriptycene (HCl salt)

### 3.1.2 Synthesis of 2, 3, 6, 7, 12, 13-Hexabromotriptycene

This compound was synthesized according to a published method.<sup>84</sup> Triptycene (1.06 g, 4.18 mmol) was dissolved in dry chloroform (stabilized with amylene) (100 mL) in a Schlenk flask under nitrogen. Iron (30 mg) and bromine (1.35 mL, 26.3 mmol) were added, and the solution was refluxed for 1.5 h. Chloroform and bromine were removed under vacuum. Recrystallization from hot chloroform yielded a white solid (4.0 g, 69%). <sup>1</sup>H NMR (300 MHz, CDCl<sub>3</sub>) δ (ppm) 5.23 (s, 2H), 7.62 (s, 6H). <sup>13</sup>C NMR (75 MHz, CDCl<sub>3</sub>) δ (ppm) 144.2, 129.3, 122.0, 51.3



### 3.1.3 Synthesis of N<sup>2</sup>,N<sup>3</sup>,N<sup>6</sup>,N<sup>7</sup>,N<sup>14</sup>,N<sup>15</sup> Hexakis(diphenylmethylene)triptycene-2,3,6,7,14,15 hexaamine.

This compound was synthesized according to a published method.<sup>47</sup> Tris(dibenzylideneacetone)dipalladium(0) (614 mg, 0.67 mmol) and rac-BINAP (840 mg, 1.36 mmol) were charged in a 250 mL Schlenk flask under nitrogen atmosphere and 70 mL of anhydrous toluene was added. The mixture heated at 110 °C for 30 min and cooled to room temperature under N<sub>2</sub> atmosphere. The benzophenone imine (3.60 mL, 21.4 mmol), 2, 3, 6, 7, 12, 13-hexabromotriptycene (2.00 g, 2.75 mmol), sodium tert-butoxide (2.06 g, 21.4 mmol) were added to the cooled mixture and refluxed overnight at 110 °C. The resultant solution was cooled to room temperature, diluted with CH<sub>2</sub>Cl<sub>2</sub> then filtered through a filter paper (Whatman®, 55 mm ø) and evaporated to dryness under reduced pressure. The residue was subjected to column chromatography on silica gel with EtOAc/hexane (1:4) as the eluent. The second fraction was collected and evaporated to dryness to give an orange solid. Recrystallization of this solid from EtOAc/EtOH afforded N<sup>2</sup>,N<sup>3</sup>,N<sup>6</sup>,N<sup>7</sup>,N<sup>14</sup>,N<sup>15</sup>-Hexakis(diphenylmethylene)triptycene 2,3,6,7,14,15 hexaamine as a yellowish orange crystalline solid (3.06 g, 84%). <sup>1</sup>H NMR (300 MHz, CDCl<sub>3</sub>) δ (ppm) 7.62 (d, j = 6.0 Hz, 12H, *o*-Ph CH), 7.23-7.40 (m, 24H, *m*-Ph CH (12H), *p*-Ph CH (6H+6H)), 7.13 (t, j = 9.0 Hz, 12H, *m*-Ph CH), 6.60 (d, j = 6.0 Hz, 12H, *o*-Ph CH), 6.35 (s, 6H, triptycene aromatic CH), 4.36 (s, 2H, triptycene aliphatic CH). <sup>13</sup>C NMR (75 MHz, CDCl<sub>3</sub>) δ (ppm) 166.9, 141.0, 140.9, 137.5, 137.1, 130.2, 129.8, 129.4, 128.7, 128.0, 117.2, 52.7.

### 3.1.4 Synthesis of 2,3,6,7,14,15-Hexaaminotriptycene (HATT)

This compound was synthesized according to a published method.<sup>47</sup> 2.0 M aqueous HCl solution (1.7 mL, 3.4 mmol) was added to a THF solution (22 mL) of N<sup>2</sup>,N<sup>3</sup>,N<sup>6</sup>,N<sup>7</sup>,N<sup>14</sup>,N<sup>15</sup>-Hexakis(diphenylmethylene)triptycene-2,3,6,7,14,15 hexaamine (500 mg, 0.38 mmol) and the mixture was stirred at room temperature for 0.5 h. The precipitate was isolated by filtration, washed with THF and hexane, and dried under vacuum to give the hexaammoniumtriptycene hexachloride salt as a brownish solid (216 mg, 95%). <sup>1</sup>H NMR (300 MHz, DMSO-d<sub>6</sub>) δ (ppm) 6.99 (s, 6H, triptycene aromatic CH), 5.26 (s, 2H, triptycene aliphatic CH). <sup>1</sup>H NMR (300 MHz, D<sub>2</sub>O) δ (ppm) 7.23 (s, 6H, triptycene aromatic CH), 5.52 (s, 2H, triptycene aliphatic CH). <sup>13</sup>C NMR (75 MHz, D<sub>2</sub>O) δ (ppm) 142.9, 124.6, 118.5, 50.6.

### 3.1.5 Synthesis of DBLP-3

1,4-benzenediboronic acid (BDBA) (42 mg, 0.25 mmol) and 2,3,6,7,14,15-hexaaminotriptycene (HATT) (100 mg, 0.18 mmol) were ground with a mortar and pestle then suspended in 30 mL of dry N-N-dimethylformamide (DMF) under a nitrogen atmosphere in a 100 mL Schlenk flask. The resulting solution was bubbled with nitrogen gas for 10 minutes then sonicated for around 30 minutes. The flask was transferred into an oven and gradually heated until 130 °C then kept at that temperature for three days. The reaction flask was cooled to ambient temperature then transferred to a glovebox. The product was filtered over a medium glass frit and washed with dry DMF and dry acetone. The product was soaked in 15 ml dry acetone/DMF (50:50 v:v) mixture for 12 hours at which point the solvent was decanted and soaking continued for an additional 12 hours with dry acetone. This was followed by a further 12 hours soaking after replenishing the solvent. The solid was then filtered and activated at 110 °C under reduced

pressure for 16 hours to afford DBLP-3 (53 mg, 65% yield) as a greenish solid. Anal. Calcd. for  $C_{58}H_{34}B_6N_{12}(12H_2O)$ : C, 58.73%; H, 5.44%; N, 14.17%; Found: C, 59.82%; H, 4.19%; N, 12.53%.

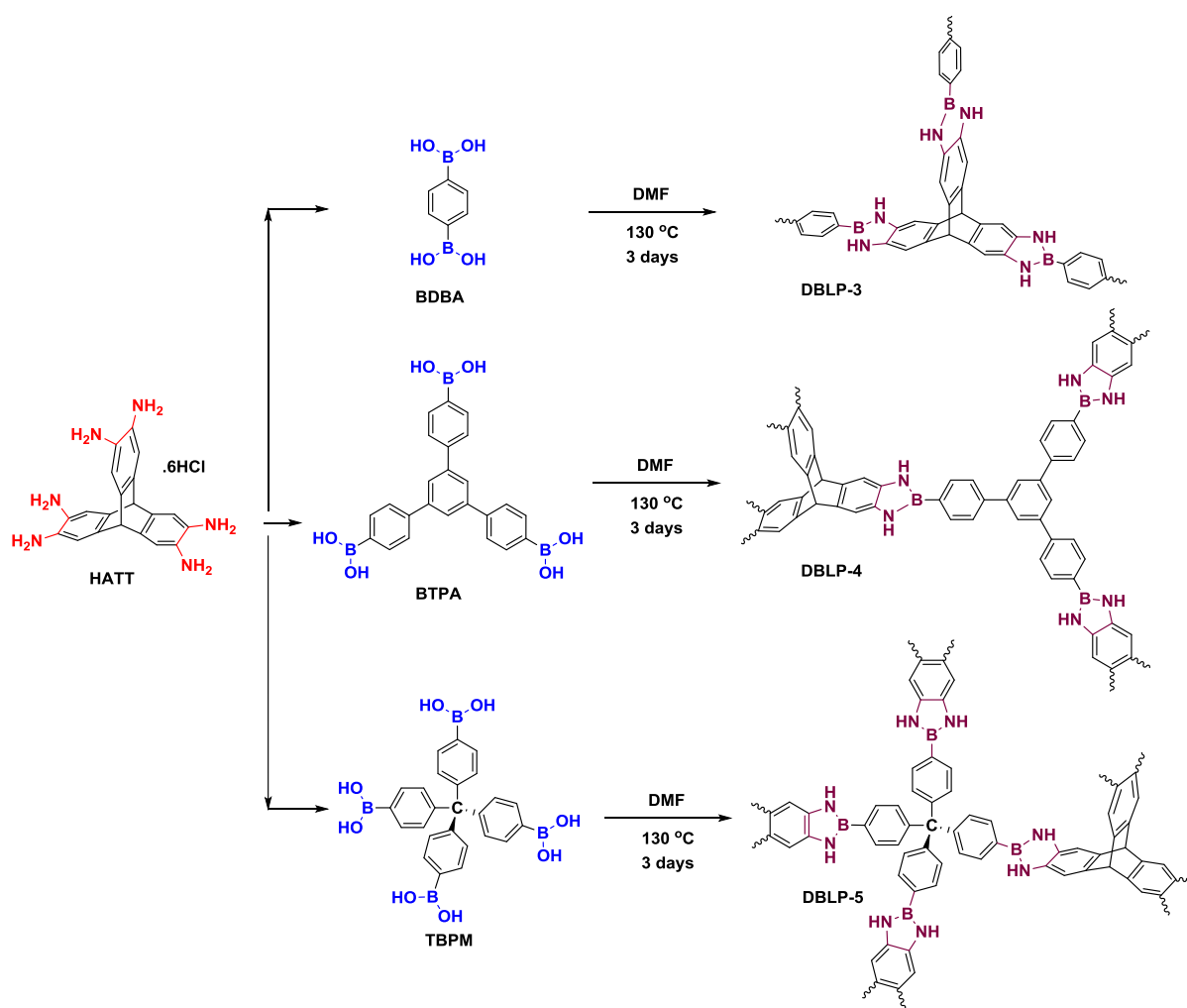
### 3.1.6 Synthesis of DBLP-4

1,3,5-benzenetriboronic acid (BTBA) (46.6 mg, 0.094 mmol) and 2,3,6,7,14,15-hexaaminotriptycene (HATT) (60 mg, 0.107 mmol) were grained with a mortar and pestle then suspended in 30 mL of dry N-N-dimethylformamide (DMF) under a nitrogen atmosphere in a 100 mL Schlenk flask. The resulting solution was bubbled with nitrogen gas for 10 minutes then sonicated for around 30 minutes. The flask was transferred into an oven and gradually heated to 130 °C and left for incubation for 72 hours. The reaction flask was cooled to ambient temperature then transferred to a glovebox. The product was filtered over medium glass frit and washed with dry DMF and dry acetone. The product was soaked in 15 ml dry acetone/DMF (50:50 v:v) mixture for 12 hours at which point the solvent was decanted and only dry acetone was added for 12 hours more. This was followed by a further 12 hours soaking after replenishing the solvent. The solid was then filtered and activated at 110 °C under reduced pressure for 16 hours to afford DBLP-4 (42 mg, 66 % yield) as a greenish solid. Anal. Calcd. for  $C_{44}H_{29}B_3N_6(6H_2O)$ : C, 67.56%; H, 5.28%; N, 10.74%. Found: C, 70.22%; H, 4.99%; N, 8.52%.

### 3.1.7 Synthesis of DBLP-5

Tetra(4-dihydroxyborylphenyl)methane (TBPM) (40 mg, 0.080 mmol) and 2,3,6,7,14,15-hexaaminotriptycene (HATT) (60 mg, 0.107 mmol) were grained with a mortar and pestle then suspended in 30 mL of dry N-N-dimethylformamide (DMF) under a nitrogen atmosphere in a 100 mL Schlenk flask. The resulting solution was bubbled with nitrogen gas for 10 minutes then

sonicated for around 30 minutes. The flask was transferred into an oven and gradually heated to 130 °C and incubated for 72 hours. The reaction flask was cooled to ambient temperature then transferred to a glovebox. The product was, filtered over a medium glass frit and washed with dry DMF and dry acetone. The product was soaked in 15 ml dry acetone/DMF (50:50 v:v) mixture for 12 hours at which point the solvent was decanted and only dry acetone was added for 12 hours more. This was followed by a further 12 hours soaking after replenishing the solvent. The solid was then filtered and activated at 110 °C under reduced pressure for 16 hours to afford DBLP-5



**Scheme 3.2:** Synthesis of DBLP-3, DBLP-4, and DBLP-5

(58 mg, 60 % yield) as a greenish solid. Anal. Calcd. for  $C_{155}H_{104}B_{12}N_{24}(24H_2O)$ : C, 64.99%; H, 5.35%; N, 11.73%. Found: C, 66.79%; H, 4.72%; N, 8.14%.

### 3.3. Results and Discussion

#### 3.3.1 Synthesis and Characterization of DBLPs

The preparation of DBLPs typically starts with the grinding of diamine and boronic acid building blocks using a mortar-pestle to improve mixing since these units are not soluble under reaction conditions. The resultant powder is suspended in dry DMF under nitrogen atmosphere in a Schlenk flask. The flask is gradually heated to 130 °C for 3 days to afford the corresponding DBLPs (Scheme 3.2) as colored powdery products in good yields after filtration, followed by washing and drying at 120 °C and  $1.0 \times 10^{-5}$  Torr for 12 h. The purification of all DBLPs involved washing with DMF and acetone to solubilize and remove the unreacted boronic acids and 2, 3, 6, 7, 14, 15-hexaaminotriptycene. DBLPs are insoluble in common organic solvents such as tetrahydrofuran, dimethylformamide, acetone, dichloromethane, and chloroform. Polymers were prepared for spectral, analytical and porosity measurements by drying under reduced pressure and heat (120 °C). The chemical composition, stability, and phase purity and the amorphous nature of the DBLPs were established using elemental analysis, FT-IR, solid-state  $^{11}B$  and  $^{13}C$  CP-MAS, SEM and XRD, as well as porosity measurements on activated samples. Scanning electron microscopy (SEM) of the polymers revealed aggregated particles of variable size in the range of ~0.4 to ~1.0  $\mu m$ . The aggregated morphology differs for different DBLPs (Figure 3.2). The FT-IR spectrum of DBLPs (Figure 3.1) revealed N-H stretching at around  $3400\text{ cm}^{-1}$  (free N-H) and

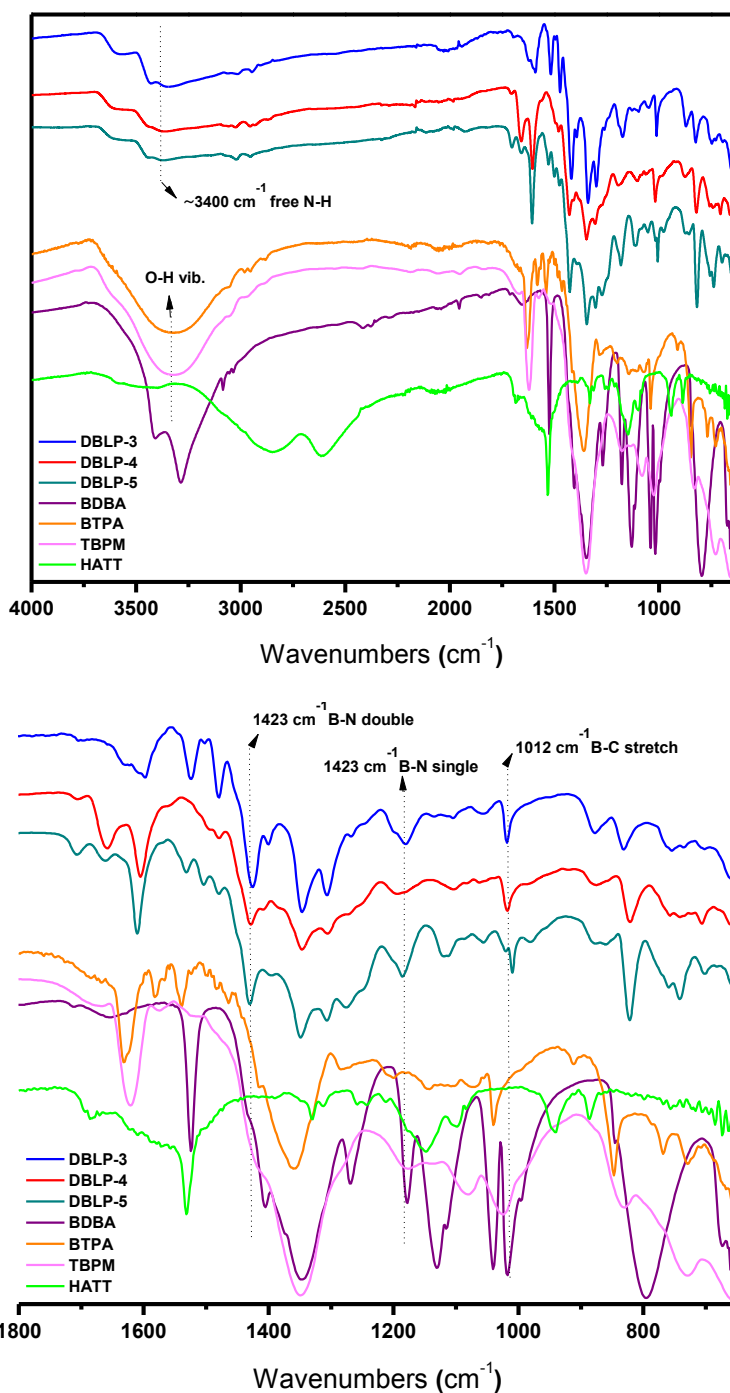


**Figure 3.1:** FT-IR spectra of DBLPs and their starting building units. Lower panel is an expanded region from 600 to 1800 cm<sup>-1</sup> disappearance of broad OH vibrations which is coming from the boronic acid units, while intense new bands appeared at 1423 cm<sup>-1</sup> (B-N, double bond character), 1171 cm<sup>-1</sup> (B-N, single bond

character), and  $1012\text{ cm}^{-1}$  (B-C stretch), can be assigned to skeleton vibration of the diazaborole ring.<sup>9, 97-99</sup>

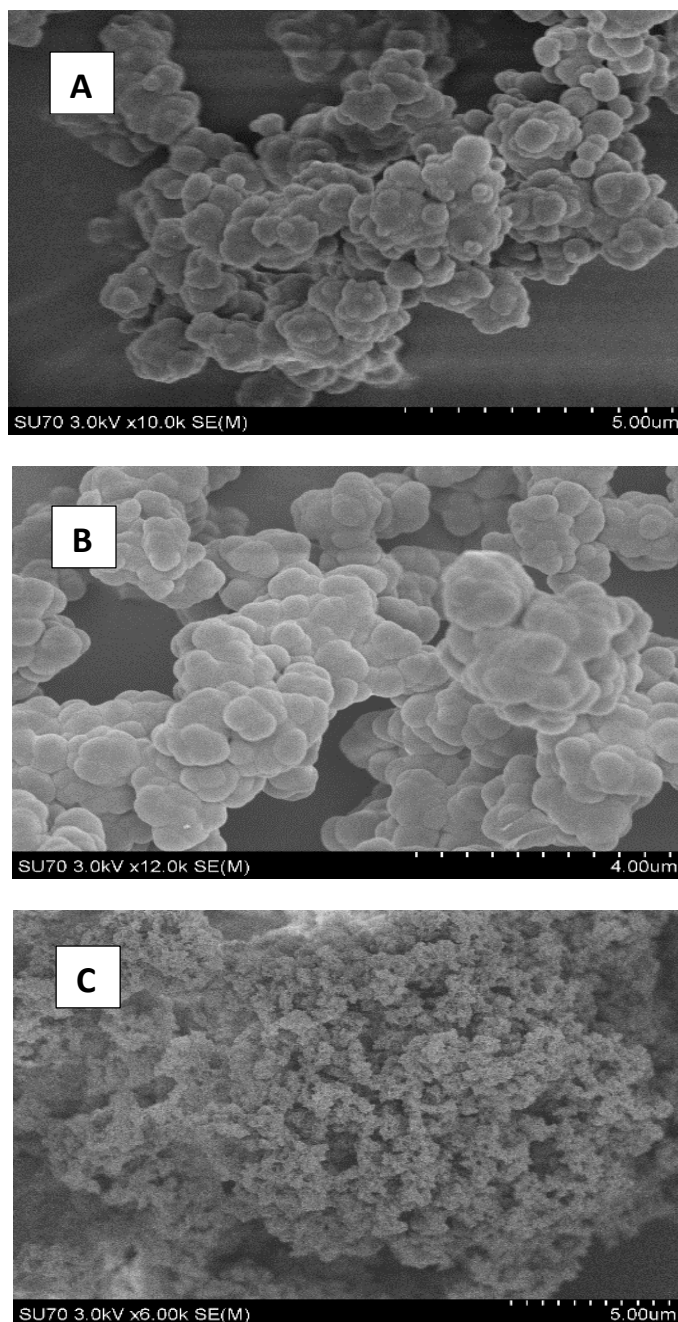


**Figure 3.2:** SEM images of A) DBLP-3, B) DBLP-4, and C) DBLP-5

The solid-state  $^{11}\text{B}$  (Figure 3.3) revealed a broad signal ranging from 19.8 ppm to 8.0 ppm which falls in the reported tri-coordinate boron atoms<sup>100</sup> and the  $^{13}\text{C}$  CP-MAS (Figure 3.5-6) spectra of DBLPs confirm their successful synthesis with the characteristic peaks. Triptycene aliphatic C-H, triptycene aromatic C-H, triptycene aromatic C, aromatic C-H, aromatic C and quaternary C for tetraphenyl methane building block peaks are found to be at 54, 64, 107, 113, 127, and 141 ppm, which further support the formation of the diazaborole ring and the incorporation of an intact triptycene moiety into the framework of DBLPs. We have selected one representative material for UV-Vis measurement to compare the electronic properties with the possible self-polycondensation of the corresponding boronic acid units. Upon exciting the DBLP-4 polymer with 340 nm light in DMF, a green emission with broad peak ranging from 450 to 680 nm is observed (Figure 3.8) whereas the self-condensed polymer of BTPA building unit showed a broad peak ranging from 350 to 450 nm. Again, this result supports the formation of diazaborole linked polymer. Thermogravimetric analysis was obtained using a TA Instruments TGA Q5000 analyzer with 50  $\mu\text{L}$  platinum pans to assess the thermal stability of each diazaborole-linked polymer. Experiments were run at a ramp rate of 5 K/minute under a nitrogen atmosphere and results showed all the polymers were stable up to 350  $^{\circ}\text{C}$  (Figure 3.4). DBLPs showed amorphous nature as evidenced by powder-XRD studies (Figure 3.7).



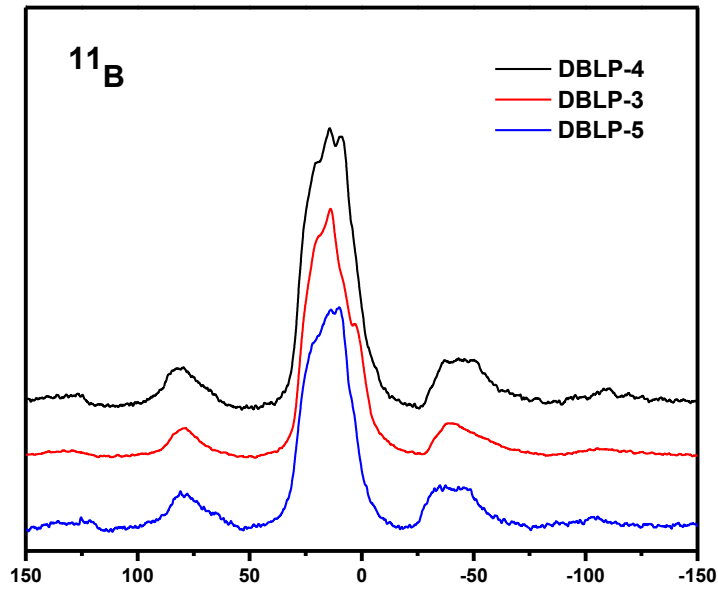


**Figure 3.3:** Solid state and <sup>11</sup>B MAS NMR spectra of DBLPs

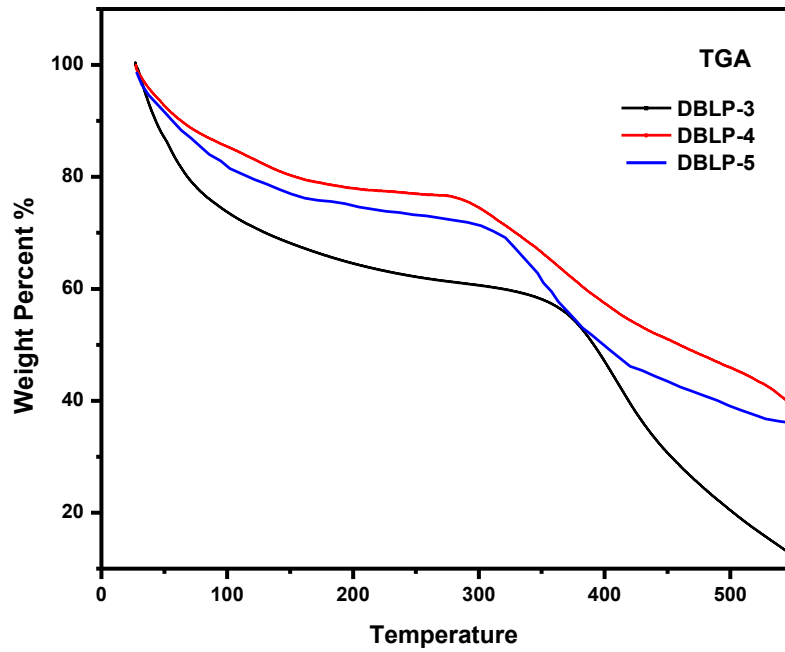


**Figure 3.4:** Thermogravimetric analysis of DBLPs

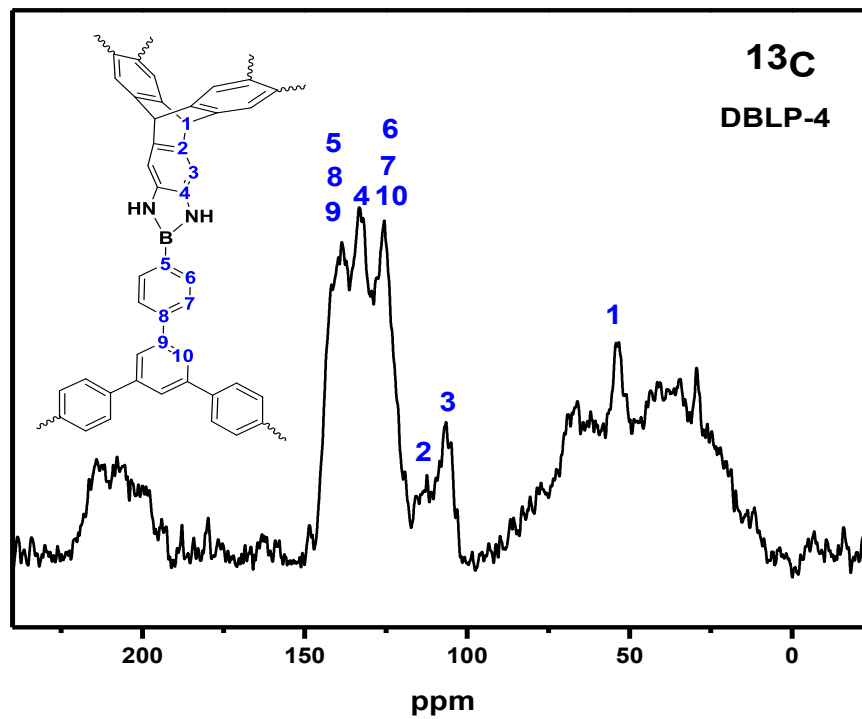
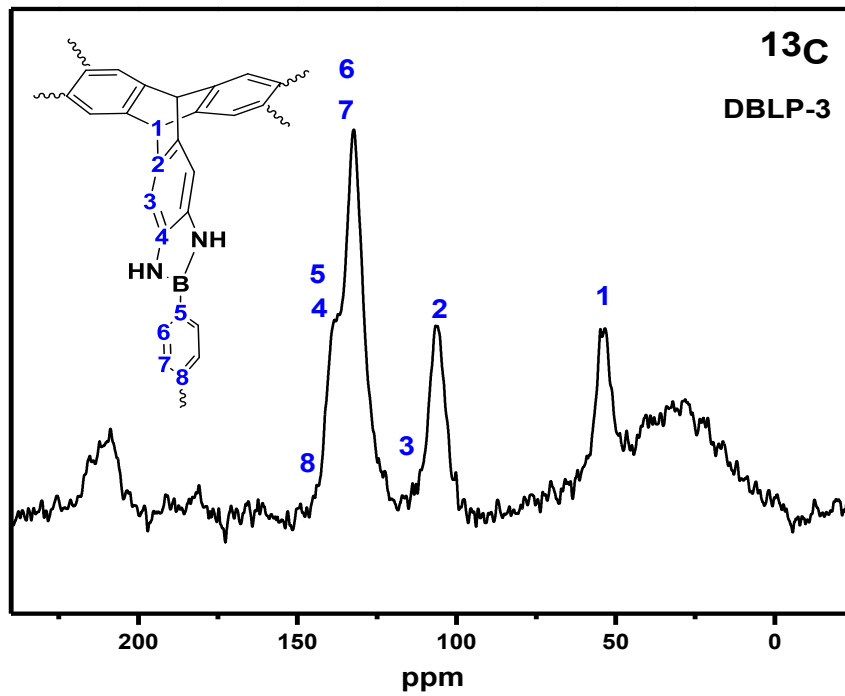


**Figure 3.5:** Solid state <sup>13</sup>C CP-MAS of DBLP 3-4

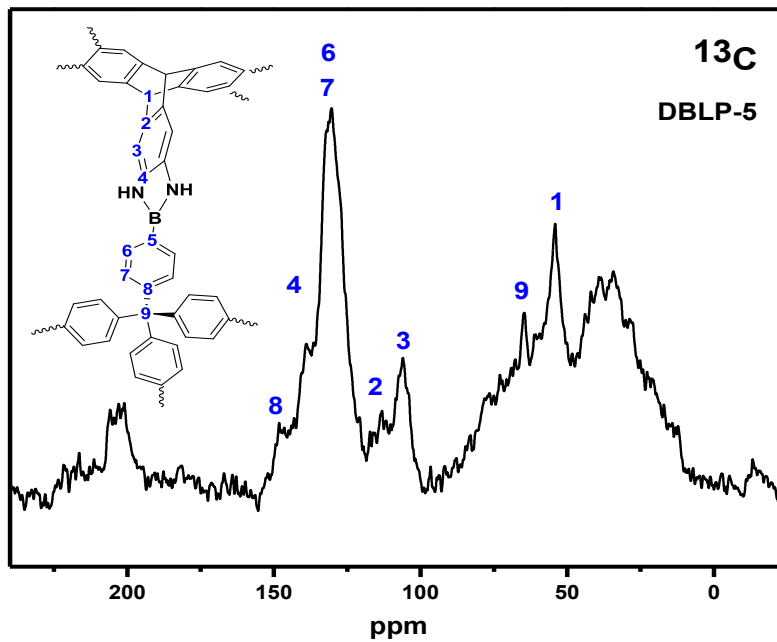


**Figure 3.6:** Solid state  $^{13}\text{C}$  CP-MAS of DBLP-5

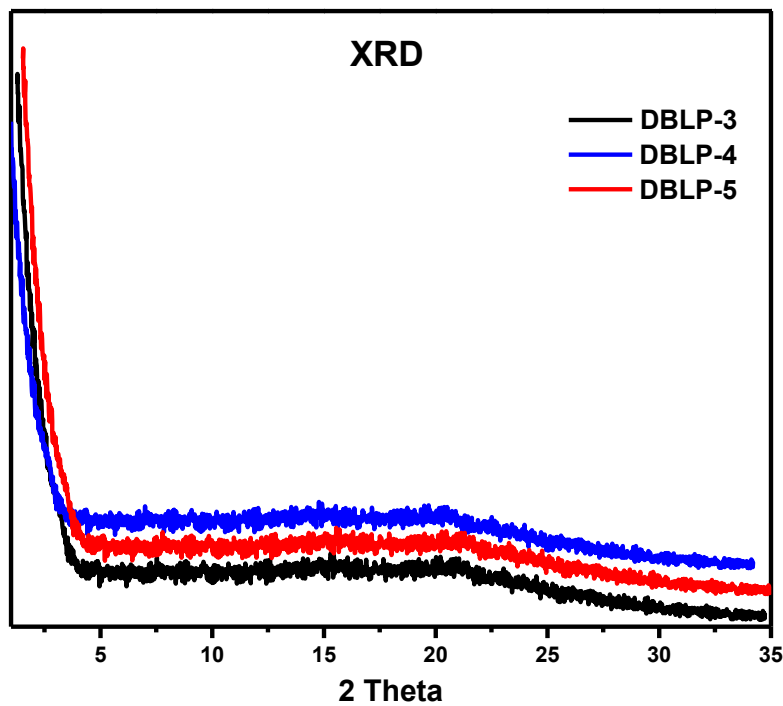


**Figure 3.7:** XRD-patterns for the DBLPs. Broad peak at around  $2\theta = 15$  indicates the amorphous characteristics of DBLPs

### 3.3.2 Porosity Studies of DBLPs

The porosity measurements of DBLPs were investigated by Ar sorption-desorption at 87 K. The pre-activated polymers were degassed at 120 °C overnight under  $1 \times 10^{-5}$  Torr vacuum to remove any remaining guest molecules before sorption measurements. The argon isotherms at 87 K for DBLPs are shown in Figure 3.9. The fully reversible isotherms show a rapid uptake at low pressure ( $P/P_0 = 0$  to 0.05 bar) and are indicative of microporosity in addition to a minor pore size distribution in the mesoporous range.

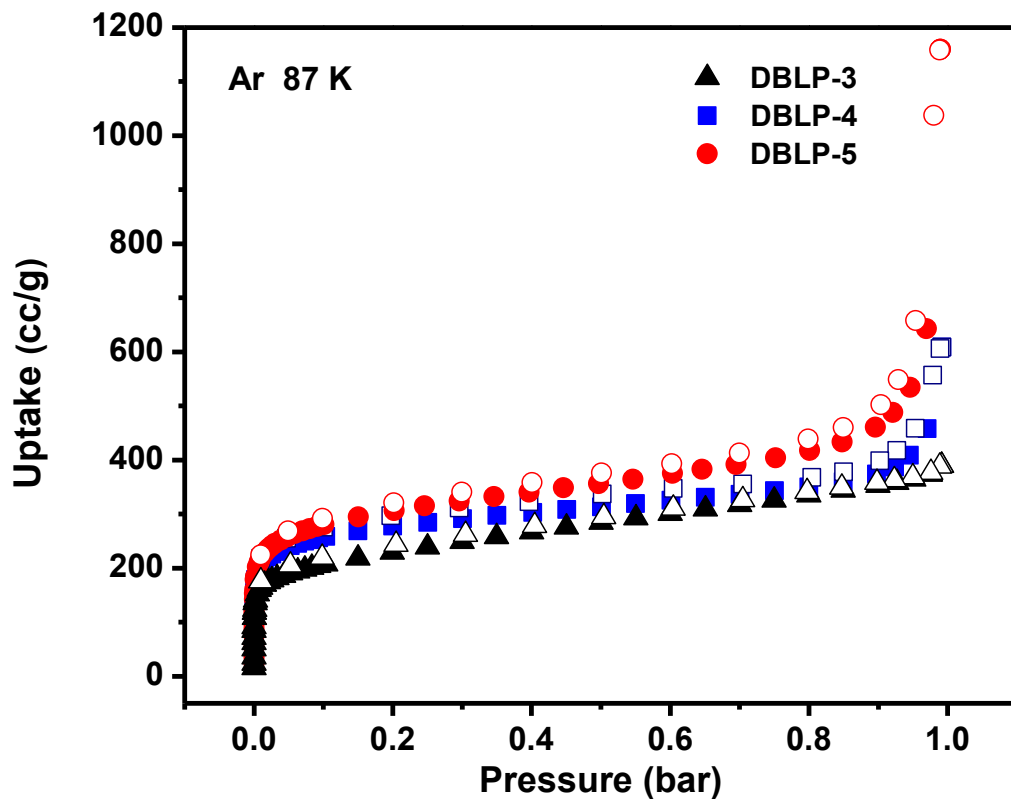


**Figure 3.8:** Ar adsorption isotherm for DBLP-3 (black), DBLP-4 (blue) and DBLP-5 (red) measured at 87 K. The filled markers are adsorption points and the empty markers are desorption points.

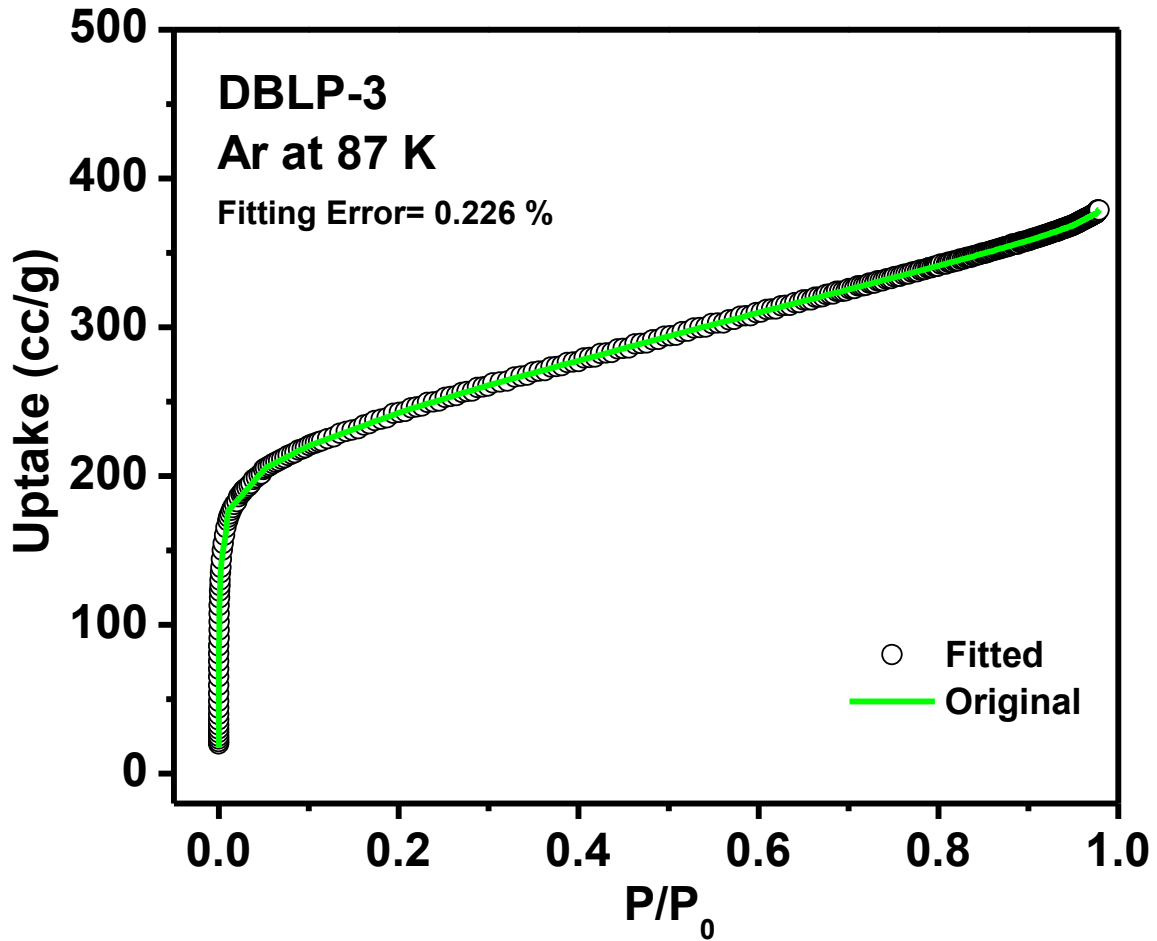


**Figure 3.9:** Experimental Ar adsorption isotherm for, DBLP-3 (black) measured at 87 K. The calculated NLDFT isotherm is overlaid as open circle. Note that a fitting error of < 1 % indicates the validity of using this method for assessing the porosity of DBLPs. The fitting error is indicated.

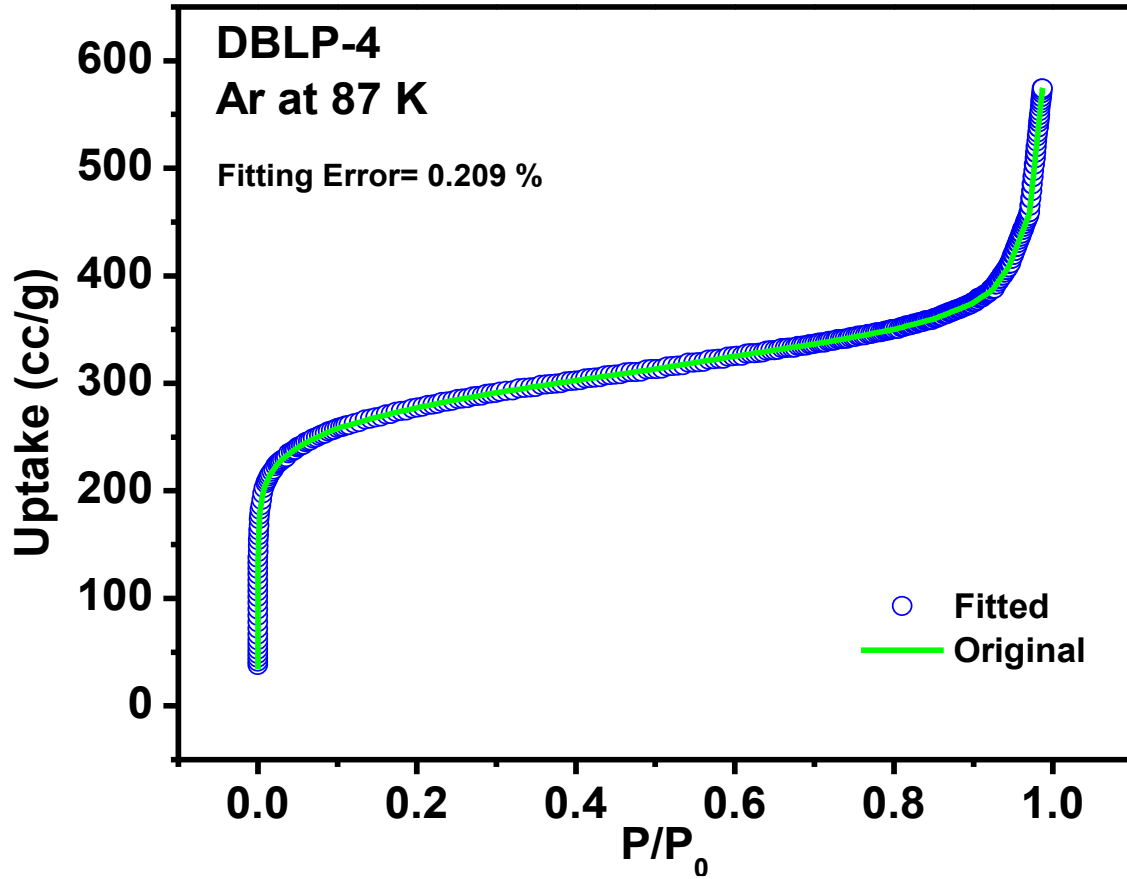


**Figure 3.10:** Experimental Ar adsorption isotherm for DBLP-4 (blue) measured at 87 K. The calculated NLDFT isotherm is overlaid as open circle. Note that a fitting error of < 1 % indicates the validity of using this method for assessing the porosity of DBLPs. The fitting error is indicated.

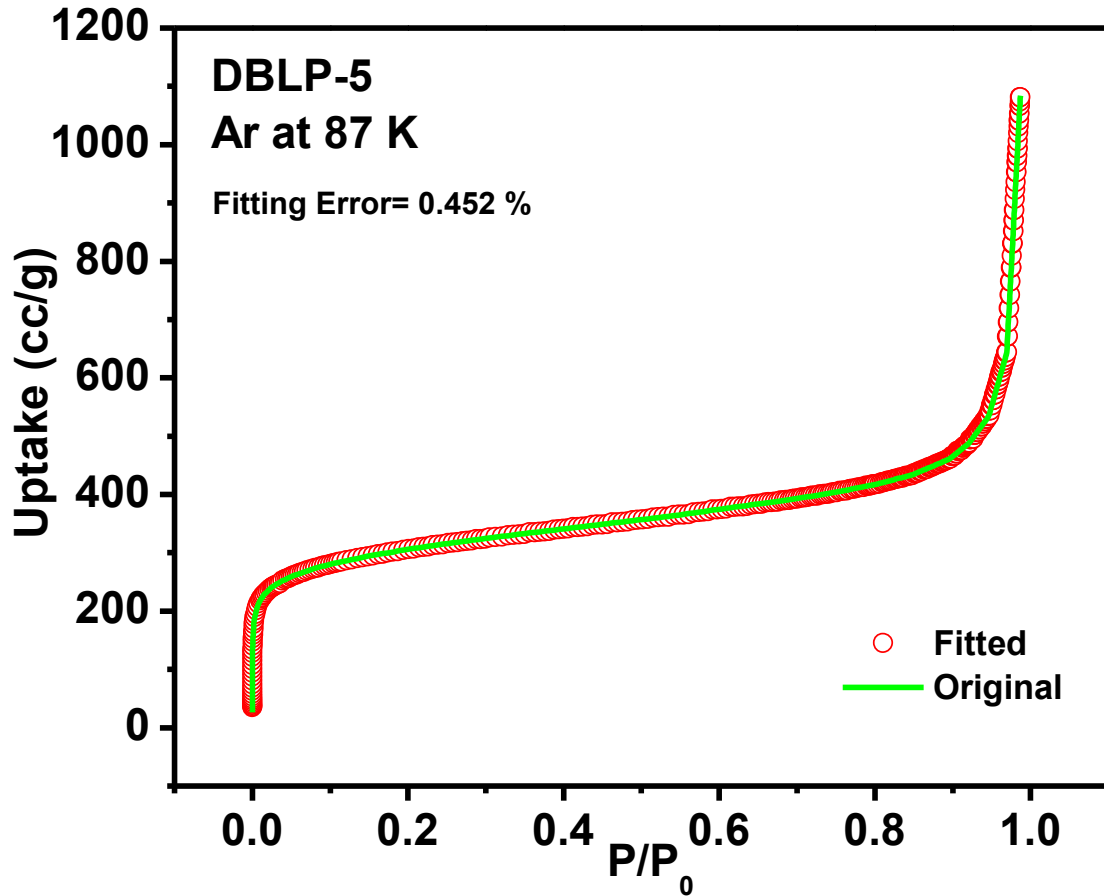


**Figure 3.11:** Experimental Ar adsorption isotherm for DBLP-5 (red) measured at 87 K. The calculated NLDFT isotherm is overlaid as open circle. Note that a fitting error of < 1 % indicates the validity of using this method for assessing the porosity of DBLPs. The fitting error is indicated.

Applying the Brunauer-Emmett-Teller (BET) model to the sorption branch within the pressure range of  $P/P_0 = 0.05-0.15$  resulted in surface areas  $SA_{BET}$  of  $730 \text{ m}^2\text{g}^{-1}$  (DBLP-3),  $904 \text{ m}^2\text{g}^{-1}$  (DBLP-4), and  $986 \text{ m}^2\text{g}^{-1}$  (DBLP-5) as shown in Figure 3.15-16. The lower porosity of 2D DBLPs as compared with 3D is, presumably, due to the favorable  $\pi-\pi$  stacking within the 2D polymers which can also be facilitated by hydrogen bonding between the diazaborole moieties. A minor hysteresis for all samples is consistent with their amorphous, powdery and the flexible nature of organic polymers. Despite their amorphous nature, they are highly porous and their surface areas are in line with a wide range of organic polymers, such as polymers of intrinsic microporosity (PIMs),<sup>55</sup> imine-linked microporous polymer organic frameworks (POFs),<sup>101</sup> diimine-based polymers,<sup>102-104</sup> functionalized conjugated microporous polymer (CMP) networks,<sup>105</sup> and benzimidazole-linked polymers (BILPs).<sup>46-48, 83</sup>

Pore size distribution (PSD) studies using nonlocal density functional theory (NLDFT) (Figure 3.13-14) were used to evaluate the impact of the network interpenetration and crosslinking on the porous nature of the DBLPs. Argon isotherms fitted with NLDFT and PSD were found to be centered around 6.6, 6.7, and 7.4 Å, while pore volume was calculated from single point measurements ( $P/P_0 \sim 0.95$ ) and found to be 0.5, 0.52, and 0.68  $\text{cc g}^{-1}$  for DBLP-3 DBLP-4, and DBLP-5, respectively. The results from PSD studies revealed that the structures of the DBLPs are highly interpenetrated compared to crystalline COF structures; to give an example, TDCOF-5<sup>106</sup> is analogous of DBLP-3 which has much larger pore size (26 Å) and surface area. This is a clear indication that the synthetic strategy used for DBLPs had little control over pore metrics.



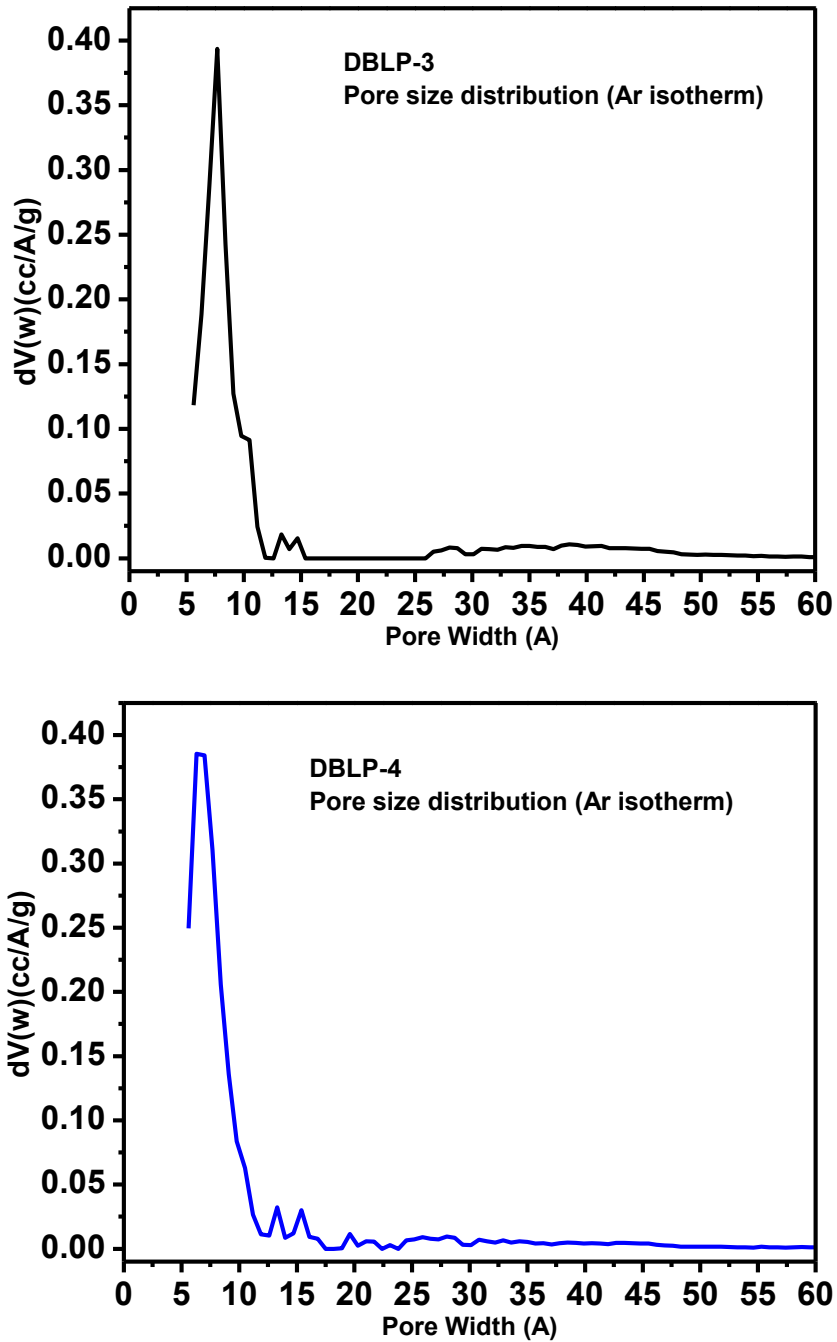


**Figure 3.12:** Pore Size Distribution for DBLP-3 (black) and DBLP-4 (blue) was calculated from the Ar adsorption isotherms by the Non-Local Density Functional Theory (NLDFT) method using a cylindrical pore model.

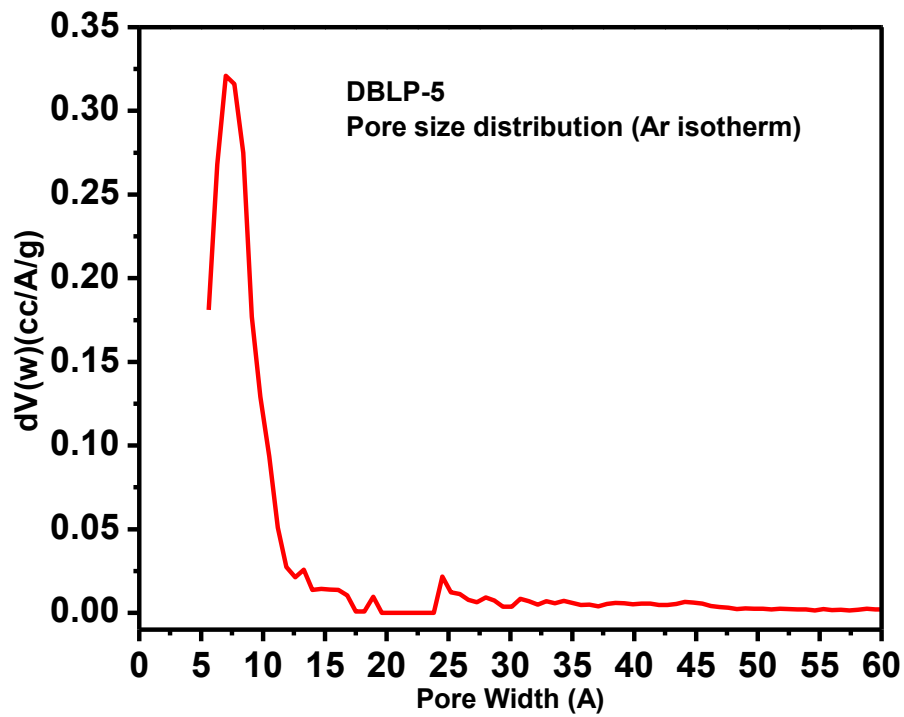


**Figure 3.13:** Pore Size Distribution for DBLP-5 (red) was calculated from the Ar adsorption isotherms by the Non-Local Density Functional Theory (NLDFT) method using a cylindrical pore model.

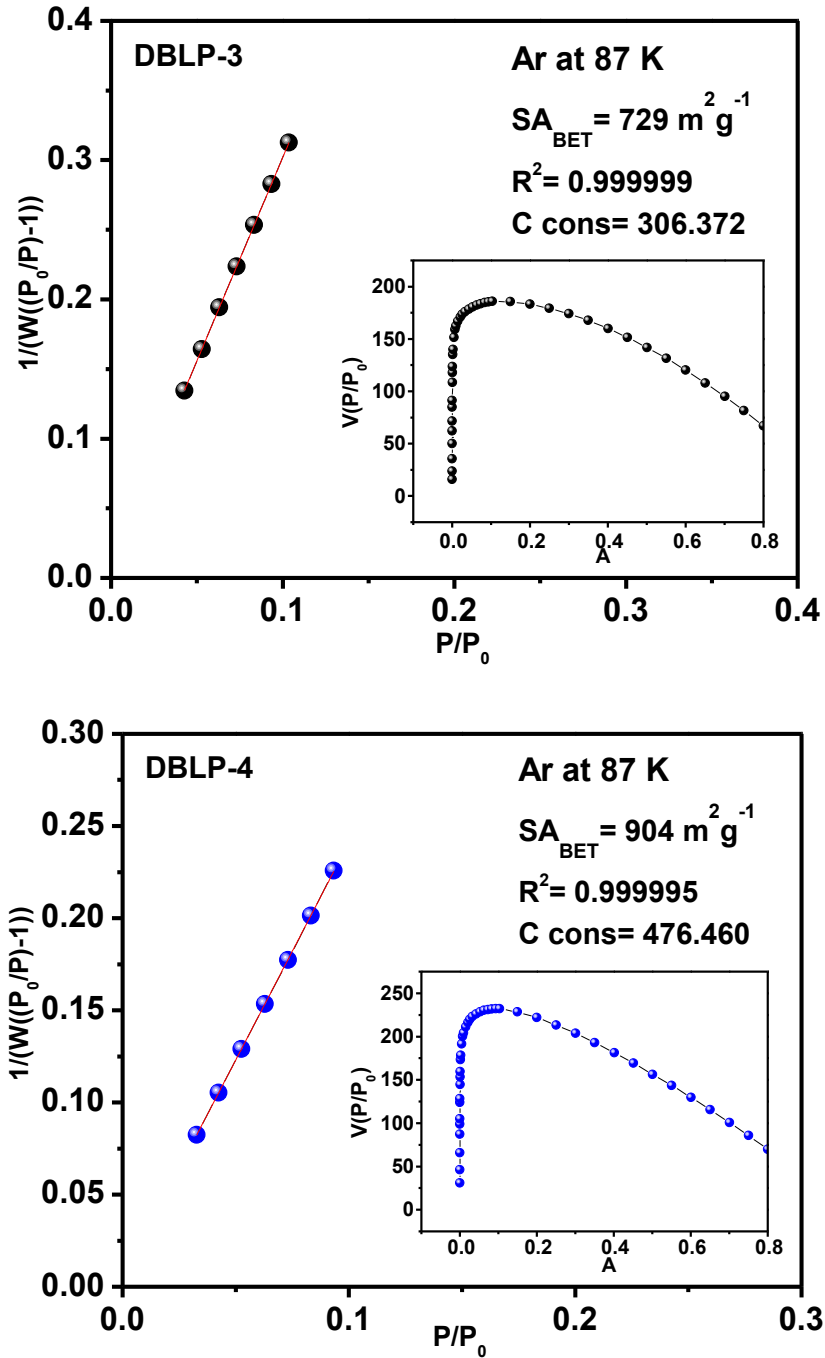


**Figure 3.14:** BET plot for DBLP-3 (black), and DBLP-4 (blue) calculated from the Ar adsorption isotherm at 87 K. The model was applied from  $P/P_0 = 0.04-0.16$ . The correlation factor is indicated. ( $W$  = Weight of gas absorbed at a relative pressure  $P/P_0$ ).

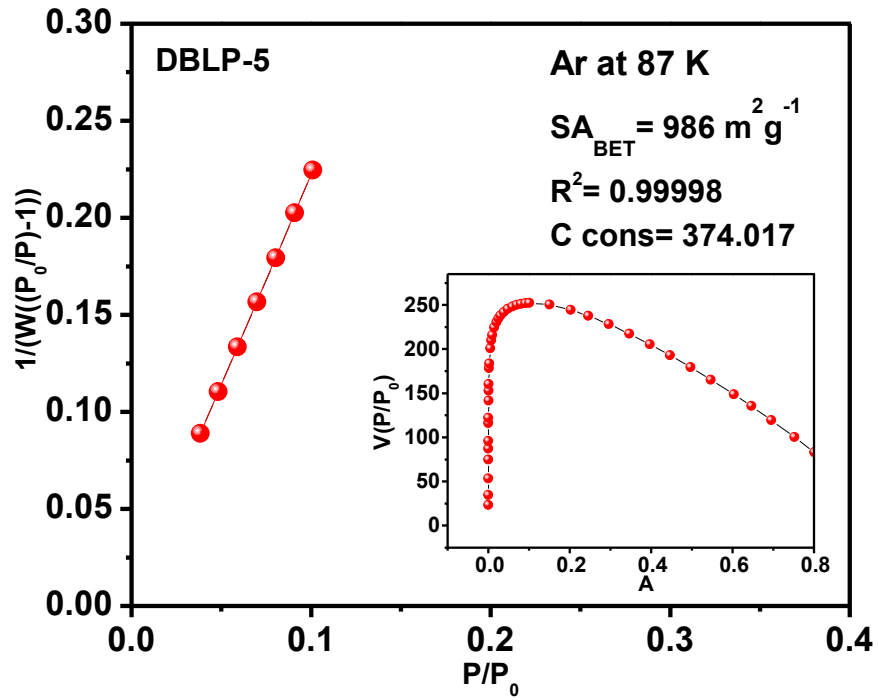


**Figure 3.15:** BET plot for DBLP-5 (red) calculated from the Ar adsorption isotherm at 87 K. The model was applied from  $P/P_0 = 0.04-0.16$ . The correlation factor is indicated. ( $W$  = Weight of gas absorbed at a relative pressure  $P/P_0$ ).

### 3.3.3 Gas Storage Studies of DBLPs

All DBLPs have subnanometer porosity, which provides small pore size and pore volume, and tunability of the chemical structure which are attractive features for gas storage and selectivity of small gases such as N<sub>2</sub>, CO<sub>2</sub>, CH<sub>4</sub> and Ar. N-functionalized pore walls have proven to enhance CO<sub>2</sub> uptakes and selectivity.<sup>5</sup> Accordingly, gas uptake measurements were collected on DBLPs by collecting H<sub>2</sub>, CO<sub>2</sub>, and CH<sub>4</sub> isotherms at low pressure (0-1.0) bar. The CO<sub>2</sub> gas adsorption performances of DBLPs were investigated by CO<sub>2</sub> isotherms at 273 K up to 1 bar and found to be fully reversible and exhibit a steep rise at low pressures (Figure 5C). The CO<sub>2</sub> sorption of the DBLP-4 found to be 198 mg g<sup>-1</sup> (4.50 mmol g<sup>-1</sup>) at 273 K and 1 bar which is higher than BILP-10 (177 mg g<sup>-1</sup>)<sup>48</sup>, and also wide range of porous organic polymers such as and -OH functionalized porous organic frameworks (POFs: 4.2 mmol g<sup>-1</sup>),<sup>107</sup> BPL carbon (3.3 mmol g<sup>-1</sup>),<sup>15</sup> functionalized CMPs (1.6-1.8 mmol g<sup>-1</sup>),<sup>108</sup> porous poly(benzimidazole) PPBIs (1.4-1.8 mmol-g<sup>-1</sup>), triptycene-based microporous poly(benzimidazole) networks TBIs (2.7-3.9 mmol g<sup>-1</sup>).<sup>109</sup> The CO<sub>2</sub> uptake of DBLP-4 is also in-line with BILP-7 (4.5 mmol g<sup>-1</sup>),<sup>83</sup> BILP-4 (5.3 mmol),<sup>83</sup> and carbazole-based porous organic polymers (CPOPs, 4.82 mmolg<sup>-1</sup>). High CO<sub>2</sub> affinity may arise from the possible hydrogen bonding between the CO<sub>2</sub> and diazaborole moiety. In 2011 Nishida *et al.* showed intermolecular hydrogen bonding within their discrete diazaborole containing molecule. According to their studies, one-dimensional hydrogen-bonding network was observed between the hydrogen atoms of the diazaborole and oxygen atoms of the quinone unit (Figure 3.17) in which a  $\pi$ -stacking structure is formed between the molecules with a distance of 3.41 Å. In addition to CO<sub>2</sub> capture, hydrogen storage studies have been considered due to the potential use in automotive applications. Hydrogen uptakes of DBLPs (1.73-2.13 wt. %) at 77 K and 1 bar are higher than most of the microporous organic polymers<sup>55, 110</sup> but lower than BILP-5 (2.30 wt. %). Methane

uptake has been recorded at 273 K at 1 bar. Again methane isotherms are fully reversible due to the physical interaction of methane with the pore walls and exhibit a steep rise at low pressure and reach the maxima of 18-22.4 mg g<sup>-1</sup>.

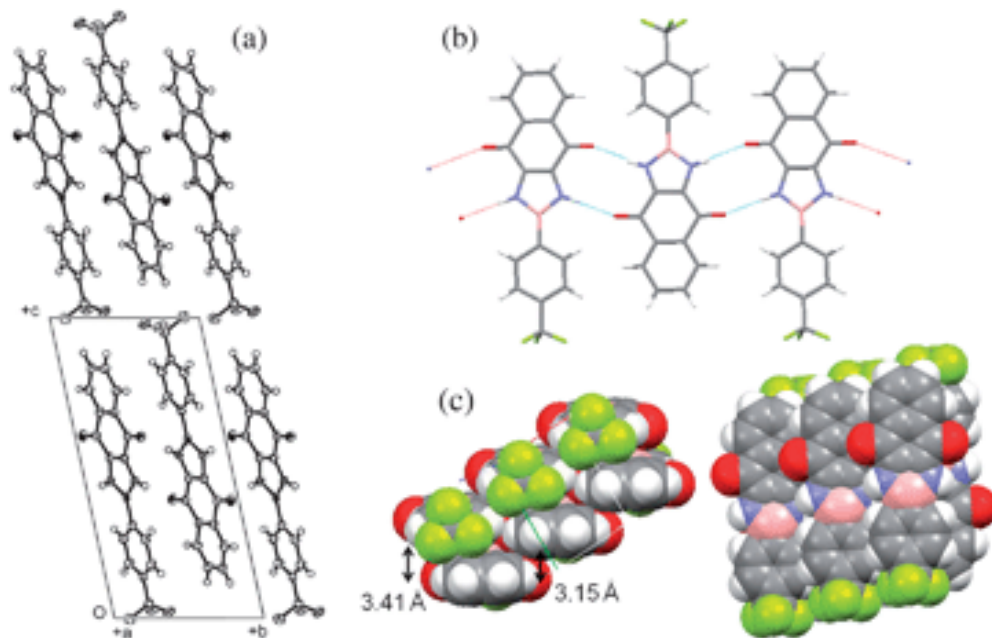


**Figure 3.16:** A) Crystal packing, B) the hydrogen-bonding network, and C) overlapping modes.<sup>9</sup>

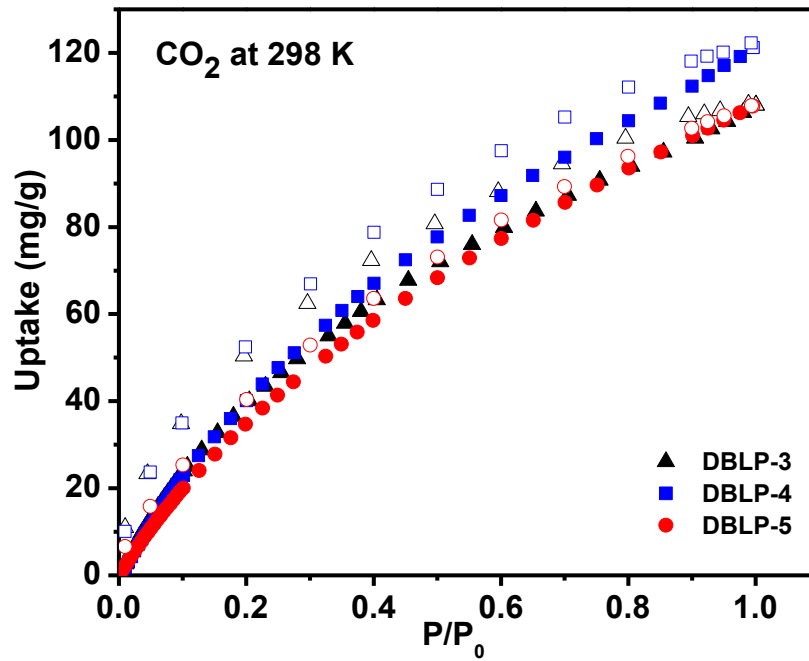
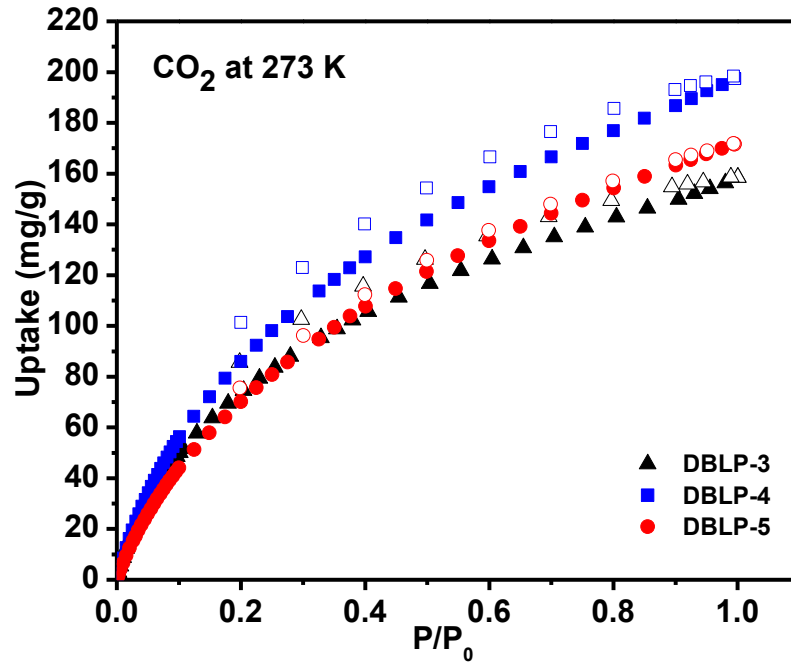


**Figure 3.17:** CO<sub>2</sub> uptake isotherms for DBLP-3 (black), DBLP-4 (blue) and DBLP-5 (red) at 273 and 298 K.

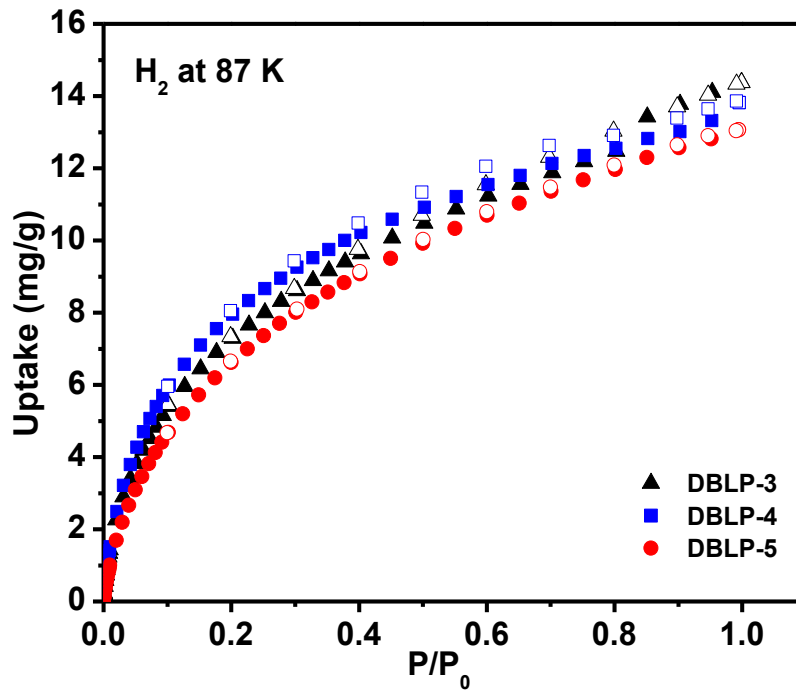
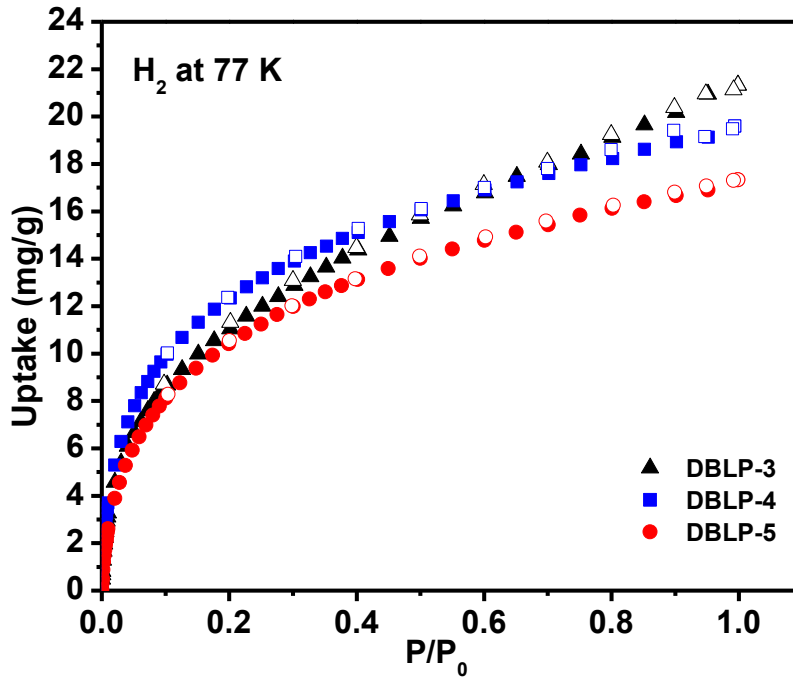


**Figure 3.18:** H<sub>2</sub> uptake isotherms for DBLP-3 (black), DBLP-4 (blue) and DBLP-5 (red) at 77 and 87 K.



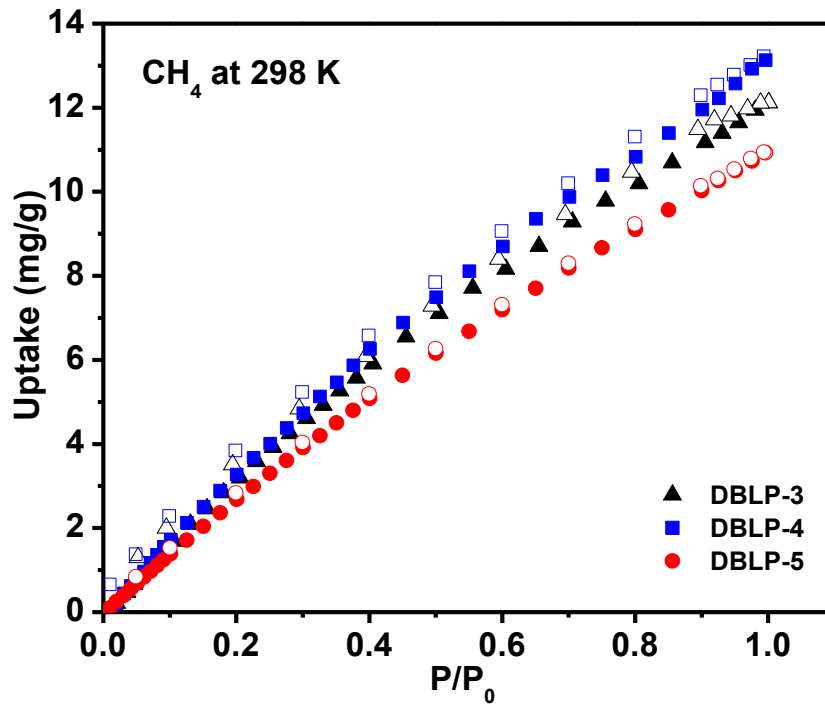
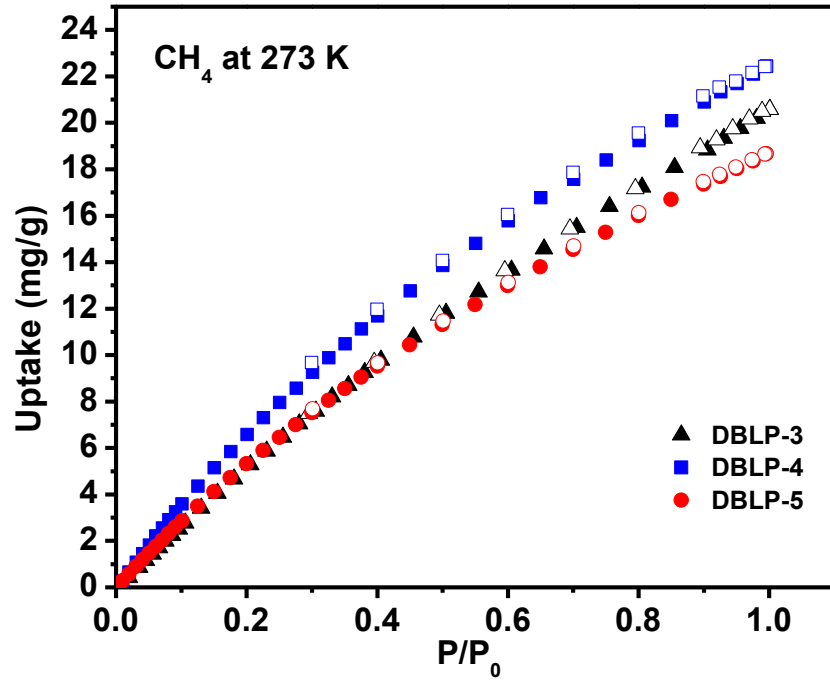


**Figure 3.19:** CH<sub>4</sub> uptake isotherms for DBLP-3 (black), DBLP-4 (blue) and DBLP-5 (red) at 273 and 298 K.

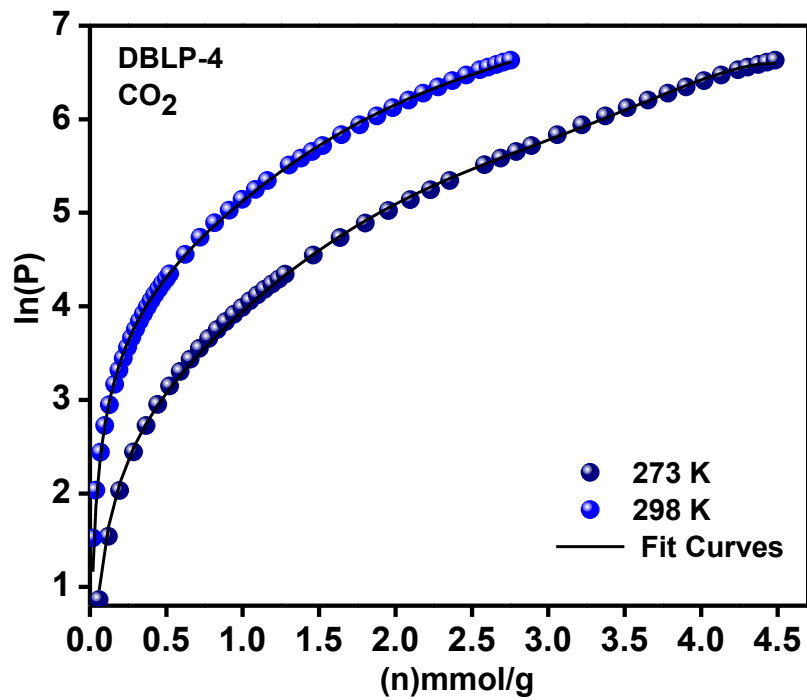
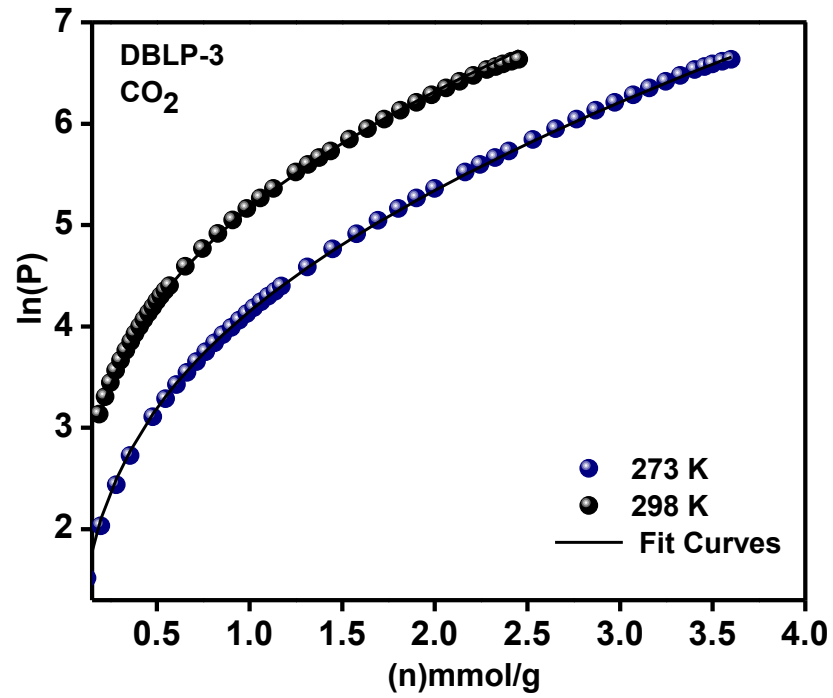
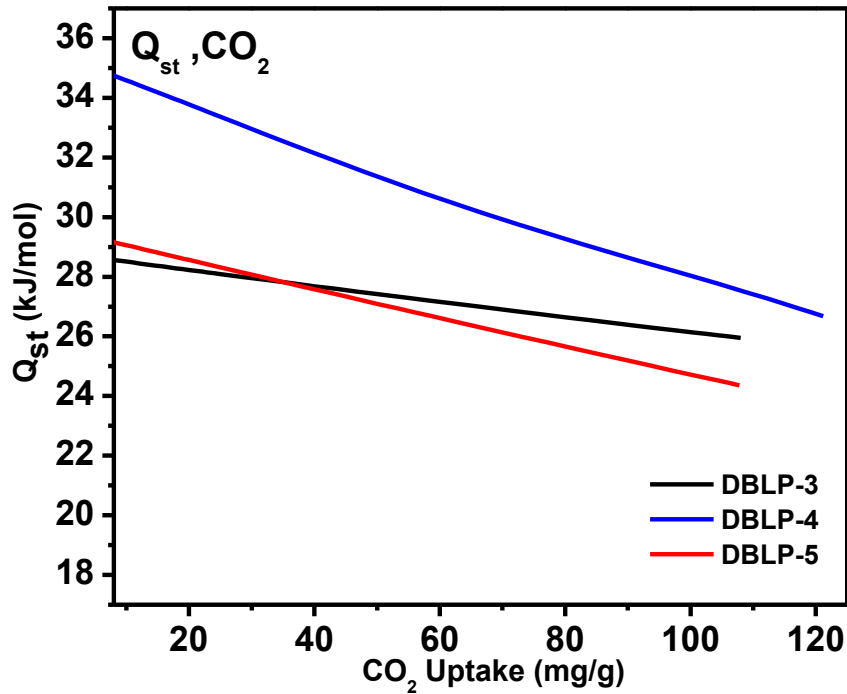
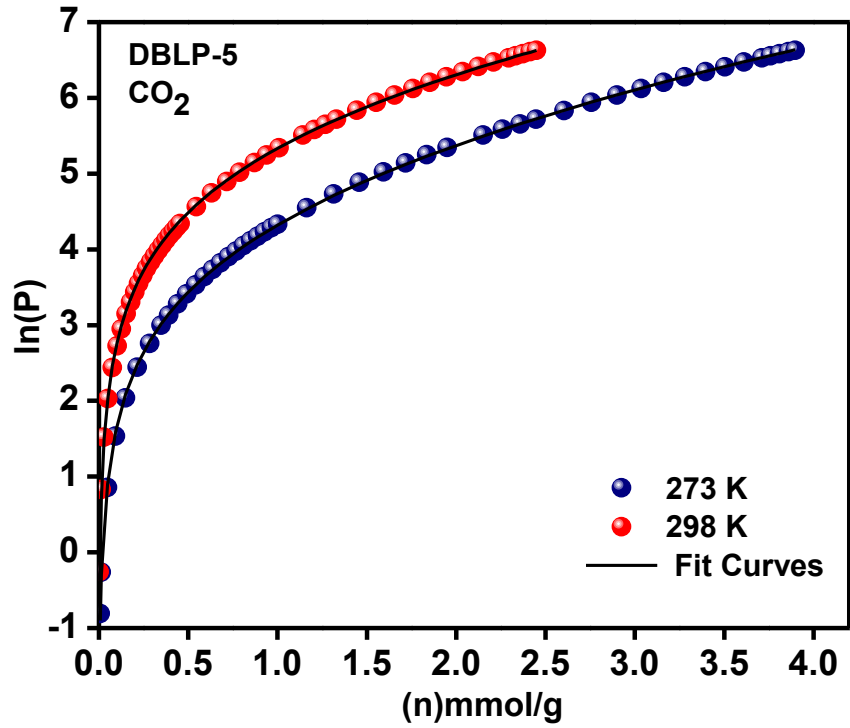


Figure 3.20: Virial analysis of CO<sub>2</sub> adsorption data for DBLP-3, and DBLP-4.



**Figure 3.21:** Virial analysis of CO<sub>2</sub> adsorption data for DBLP-5 and the isosteric heat of adsorption ( $Q_{st}$ ) for DBLP-3, DBLP-4, and DBLP-5.

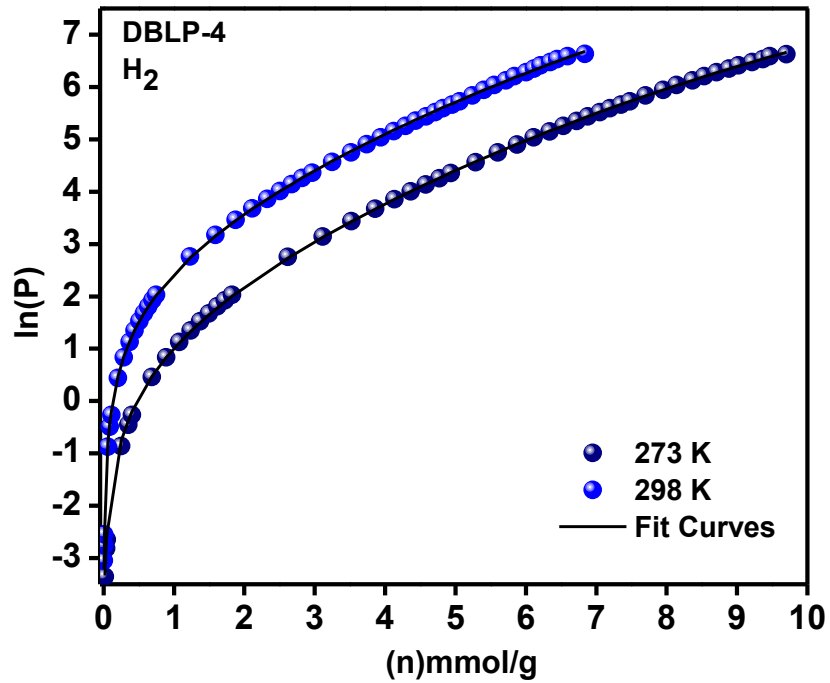
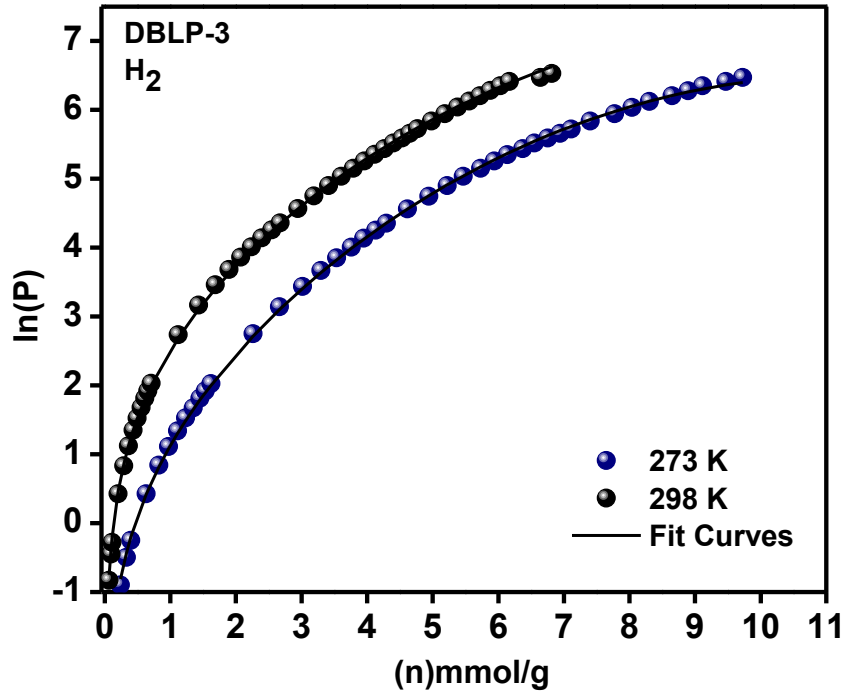
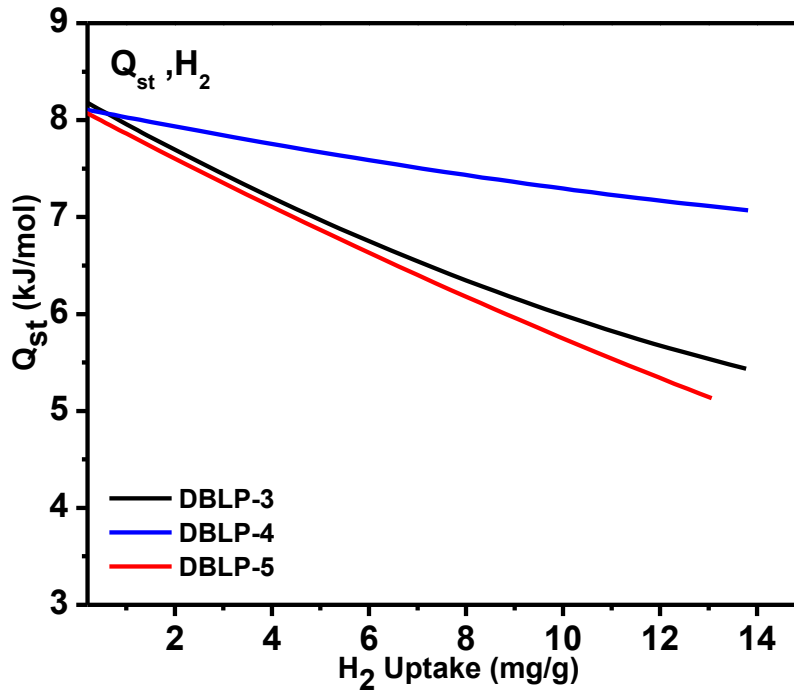
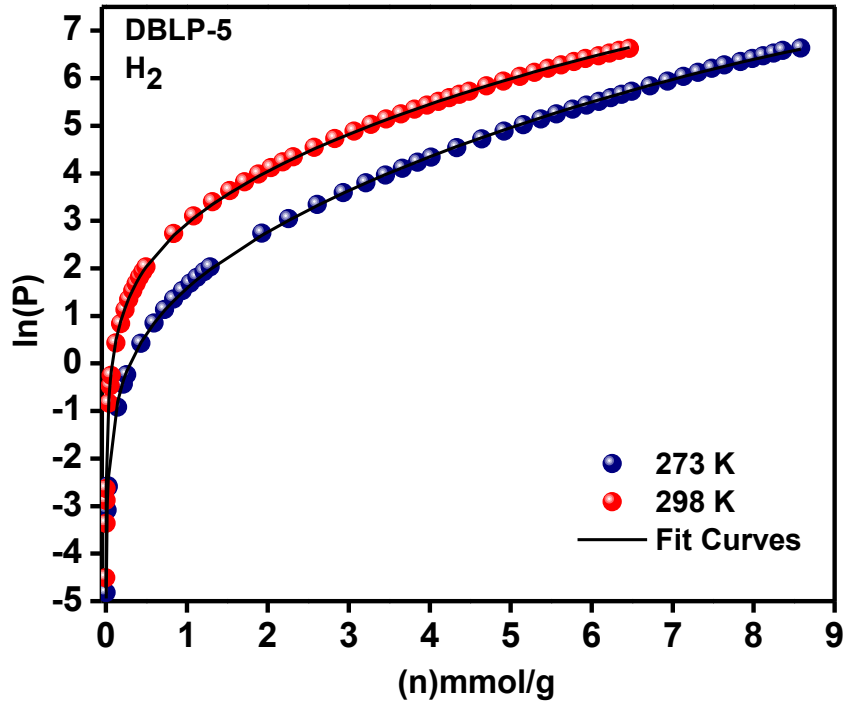


Figure 3.22: Virial analysis of H<sub>2</sub> adsorption data for DBLP-3, and DBLP-4.



**Figure 3.23:** Virial analysis of H<sub>2</sub> adsorption data for DBLP-5 and the isosteric heat of adsorption ( $Q_{st}$ ) for DBLP-3, DBLP-4, and DBLP-5.

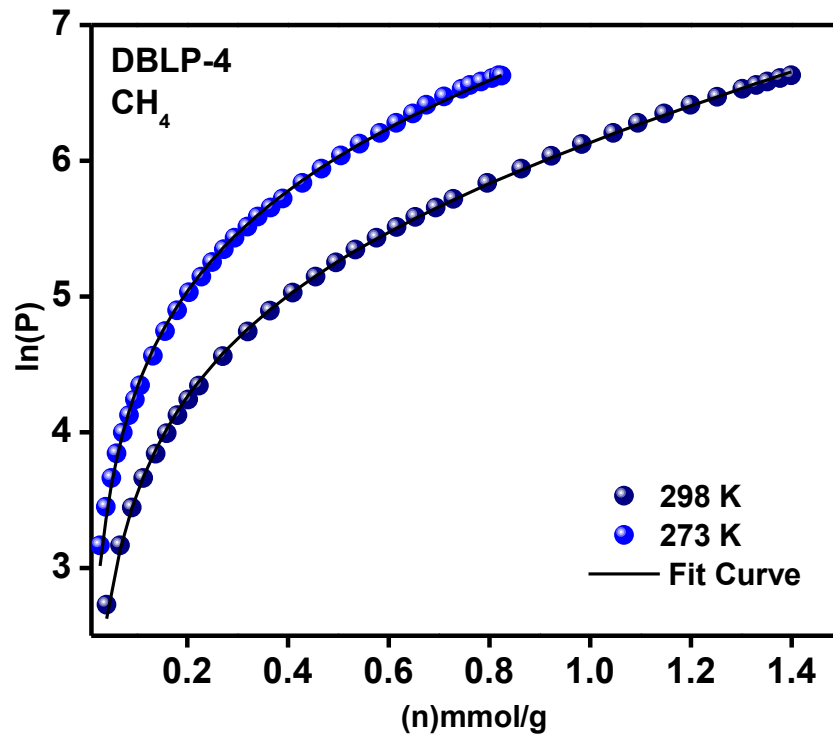
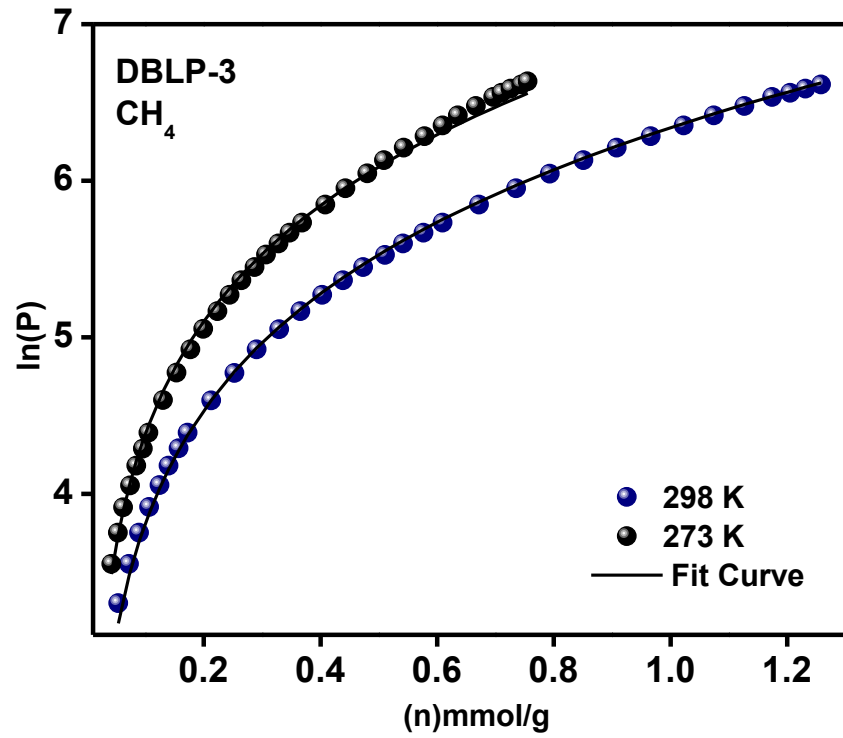
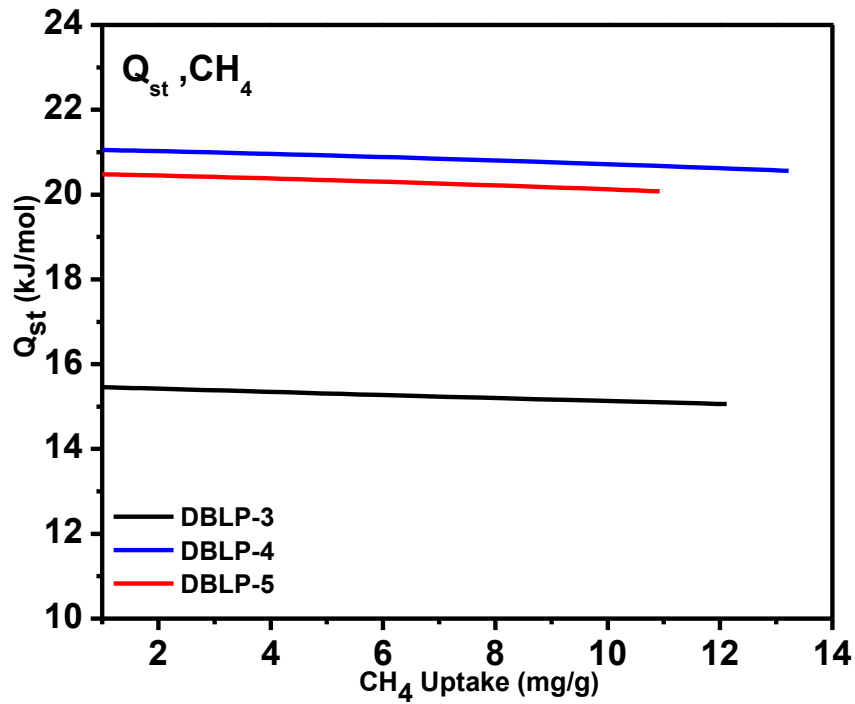
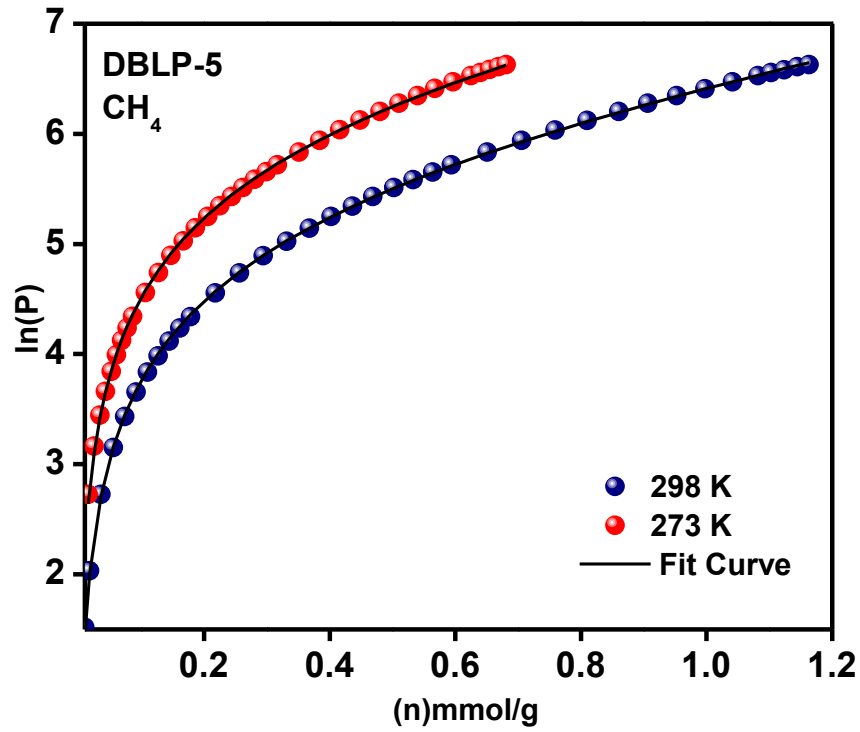


Figure 3.24: Virial analysis of CH<sub>4</sub> adsorption data for DBLP-3, and DBLP-4.



**Figure 3.25:** Virial analysis of CH<sub>4</sub> adsorption data for DBLP-5 and the isosteric heat of adsorption ( $Q_{st}$ ) for DBLP-3, DBLP-4, and DBLP-5.

The binding affinity of DBLPs for CO<sub>2</sub>, CH<sub>4</sub> and H<sub>2</sub> was calculated at 273 K and 298 K by using the virial method.<sup>52</sup> DBLPs exhibited strong heat of adsorption ( $Q_{st}$ ) for CO<sub>2</sub> ranged from 28.6-35.3 kJ mol<sup>-1</sup> at low coverage (Figure 3.21). Similar  $Q_{st}$  ranges have been also reported for several porous materials such as BILPs (26.7-28.8 kJ mol<sup>-1</sup>), PECONFs (26–34)<sup>111</sup>, PI-1 (34)<sup>112</sup> and are comparable to CO<sub>2</sub> selective MOFs<sup>24, 30, 113</sup> which generally feature –NH<sub>2</sub> or –OH functionalized pores. High  $Q_{st}$  values of polymers can be attributed to their narrow pore size distribution and multiple functionalities incorporated into the polymer network.<sup>53, 61</sup> Small depletion in  $Q_{st}$  at higher CO<sub>2</sub> loading suggests the saturation of CO<sub>2</sub> binding sites of DBLPs, which have less accessibility with increasing CO<sub>2</sub> pressure.<sup>114</sup>

In a similar way, hydrogen  $Q_{st}$  values were calculated at zero-coverage, the  $Q_{st}$  values for DBLPs are around 8.1 kJ mol<sup>-1</sup> (Figure 2.23). The  $Q_{st}$  values are higher than the values reported for organic polymers such as polyimide networks (5.3–7.0 kJ mol<sup>-1</sup>),<sup>102-104</sup> porous aromatic frameworks (PAF-1, 4.6 kJ mol<sup>-1</sup>),<sup>115</sup> porous polymer networks (PPNs, 5.5–7.6 kJ mol<sup>-1</sup>),<sup>116</sup> and comparable with BILPs (7.8-8.3 kJ mol<sup>-1</sup>),<sup>4, 7-8</sup> and –OH functionalized POFs (8.3 kJ mol<sup>-1</sup>).<sup>117</sup> The methane  $Q_{st}$  values also calculated at zero coverage were found to be 15.5-21.1 kJ mol<sup>-1</sup>.

High CO<sub>2</sub> uptake and  $Q_{st}$  properties of DBLPs encouraged us to study CO<sub>2</sub> selectivity over N<sub>2</sub> and CH<sub>4</sub>. Henry's law initial slope selectivity calculations were applied to single-component gas adsorption isotherms obtained at 273 K and 298 K (Figure 3.28-29-30). Potential use of DBLPs in flue gas and natural gas separations was examined by selectivity calculations of CO<sub>2</sub>/N<sub>2</sub> and CO<sub>2</sub>/CH<sub>4</sub> (Table 3.1). Recent selectivity studies of several porous adsorbents demonstrated that high CO<sub>2</sub> uptake coupled with narrow pore size endows more selective CO<sub>2</sub> capture.<sup>118-120</sup> Following the same trend, DBILP-4 showed higher CO<sub>2</sub>/N<sub>2</sub> selectivity (51) at 298 K, compared to DBILP-3 (42) and DBILP-5 (35) which possess lower CO<sub>2</sub> uptake and higher pore sizes (Table



3.1). In general, DBILPs showed high selectivity for CO<sub>2</sub>/N<sub>2</sub> (35-51) and CO<sub>2</sub>/CH<sub>4</sub> (5-6) at 298 K which is comparable with those of BILPs,<sup>46-48, 83</sup> MOFs,<sup>53</sup> COPs,<sup>121</sup> NPOFs,<sup>122</sup> and ALPs.<sup>49</sup>

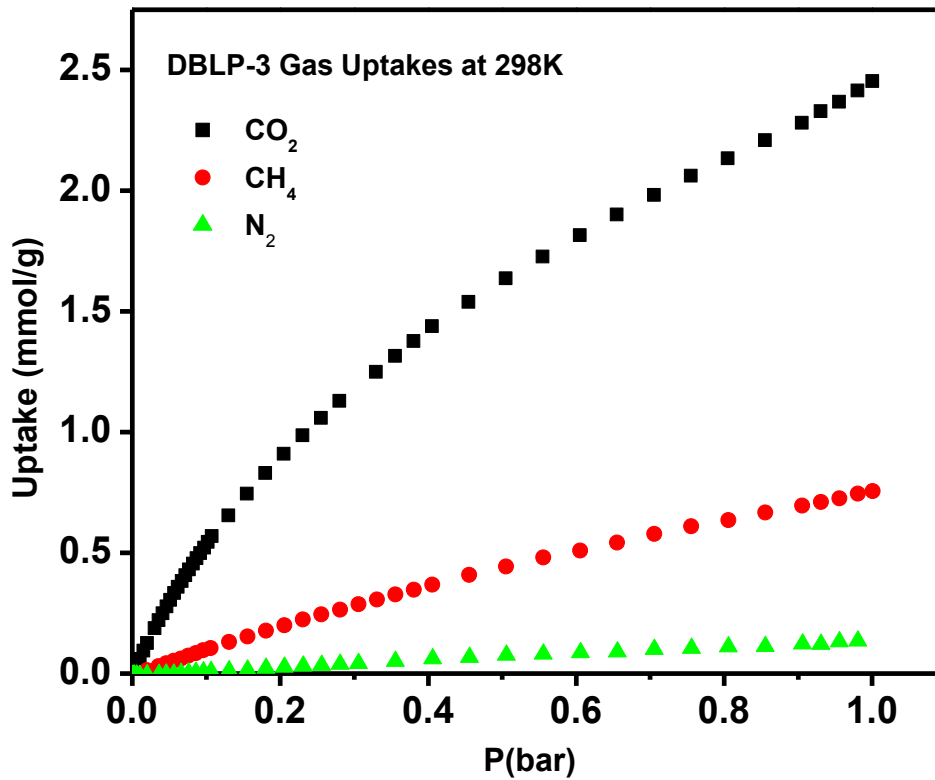


**Figure 3.26:** Gas sorption capacities for DBLP-3 at 298 K. CO<sub>2</sub> (black squares), CH<sub>4</sub> (red circles) and N<sub>2</sub> (green triangle).

Polymers	$S_{A_{BET}}$ ( $m^2 g^{-1}$ )	CO <sub>2</sub> at 1 bar		CH <sub>4</sub> at 35 bar		H <sub>2</sub> at 1 bar		Ref
		Uptake at 273 K (mg/g)	$Q_{st}$ (kJ mol <sup>-1</sup> )	Uptake at 273 K (mg/g)	$Q_{st}$ (kJ mol <sup>-1</sup> )	Uptake at 77 K (wt%)	$Q_{st}$ (kJ mol <sup>-1</sup> )	
COF-1	750	102	-	40 <sup>a</sup>	-	1.13	6.2	53, 123
COF-5	1670	59	-	89 <sup>a</sup>	-	0.87	6.0	53, 123
COF-6	750	169	-	65 <sup>a</sup>	-	1.22	7.0	53, 123
COF-8	1350	63	-	87 <sup>a</sup>	-	0.92	6.3	53, 123
COF-10	1760	53	-	80 <sup>a</sup>	-	0.84	6.6	53, 123
COF-102	3620	69	-	187 <sup>a</sup>	-	1.20	3.9	53, 123
COF-103	3530	75	-	175 <sup>a</sup>	-	1.29	4.4	53, 123
BLP-1(Cl)	1364	114	22.2	4.1	19.4	1.0	7.06	124
BLP-1(Br)	503	72	30.7	1.9	21.0	0.68	7.14	124
BLP-2(Cl)	1174	141	24.1	11.1	17.7	1.30	7.19	124
BLP-1(Br)	849	68	31.7	2.6	21.7	0.98	7.49	124
BLP-10(Br)	520	51	28.6	4.8	17.1	0.72	7.65	124
BLP-12(Cl)	1569	140	23.6	15.2	18.6	1.75	7.08	124
BLP-1(H)	1360	74	25.3	9.8	16.7	1.33	6.8	71
BLP-12(H)	2244	128	25.2	13.0	17.0	1.93	6.0	71
BLP-2(H)	1178	-	-	-	-	1.5	6.8	75

<sup>a</sup> CH<sub>4</sub> uptake at 35 bar and 298 K.

**Table 3.2 Gas Uptake and Selectivity (CO<sub>2</sub>/N<sub>2</sub> and CO<sub>2</sub>/CH<sub>4</sub>) for DBLPs**

polymer	S <sub>ABET</sub> /S <sub>A<sub>Lang</sub></sub> <sup>a</sup>	H <sub>2</sub> at 1 bar <sup>b</sup>			CO <sub>2</sub> at 1 bar <sup>b</sup>			CH <sub>4</sub> at 1 bar <sup>b</sup>			N <sub>2</sub> at 1 bar <sup>b</sup>		Selectivity <sup>c</sup>	
		77 K	87 K	Q <sub>st</sub>	273 K	298 K	Q <sub>st</sub>	273 K	298 K	Q <sub>st</sub>	273 K	298 K	CO <sub>2</sub> /N <sub>2</sub>	CO <sub>2</sub> /CH <sub>4</sub>
DBLP-3	730/893	21.3	14.4	8.1	158.5	108	28.6	20.6	12.2	15.5	16.6	3.8	42	6.2
DBLP-4	904/1040	19.6	13.8	8.1	198	173	35.3	22.4	13.2	21.1	12.0	2.8	51	4.9
DBLP-5	986/1143	17.3	13.0	8.1	171.5	108	29.5	18.7	10.9	20.5	8.6	3.9	35	5.9

<sup>a</sup>Surface area (m<sup>2</sup>g<sup>-1</sup>) was calculated from Ar isotherm. <sup>b</sup>Gas uptake in mg g<sup>-1</sup> and the isosteric enthalpies of adsorption (Q<sub>st</sub>) in kJ mol<sup>-1</sup>. <sup>c</sup>Selectivity (mol mol<sup>-1</sup>) was calculated from initial slope calculations at 298 K.

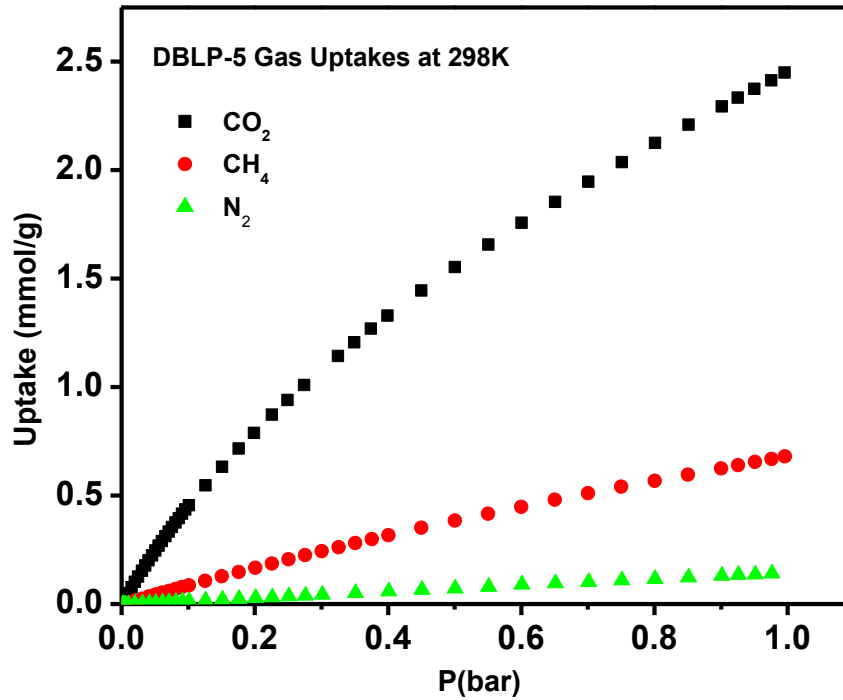
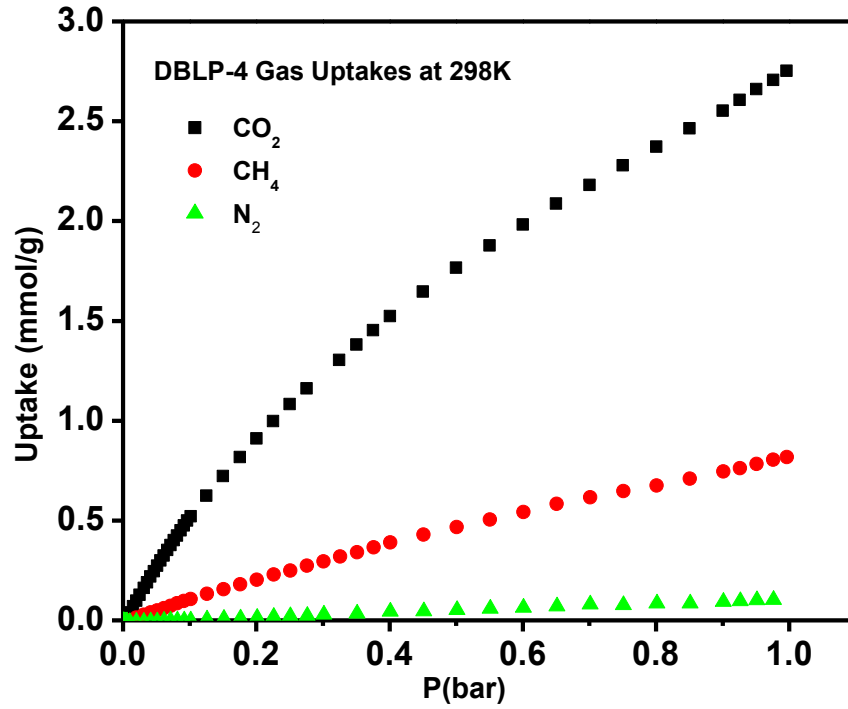


**Figure 3.27:** Gas sorption capacities for DBLP-4, and DBLP-5 at 298 K. CO<sub>2</sub> (black squares), CH<sub>4</sub> (red circles) and N<sub>2</sub> (green triangle).

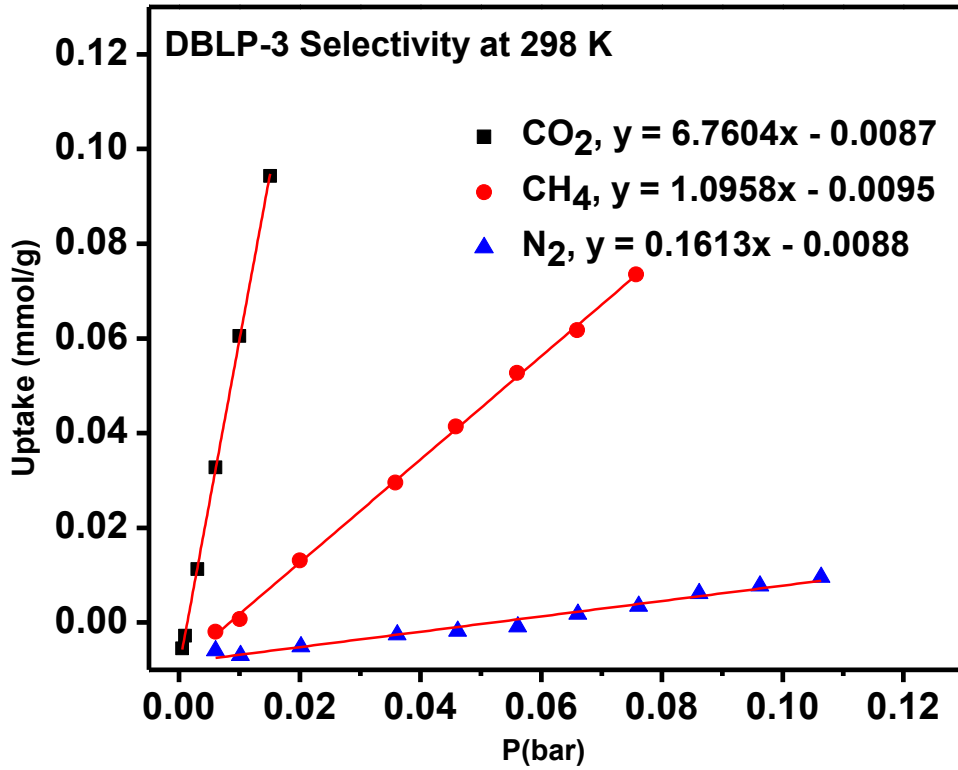


**Figure 3.28:** Adsorption selectivity of CO<sub>2</sub> over N<sub>2</sub> and CH<sub>4</sub> for DBLP-3 from initial slope calculations. CO<sub>2</sub> (black), CH<sub>4</sub> (red) and N<sub>2</sub> (blue) isotherms collected at and 298 K.

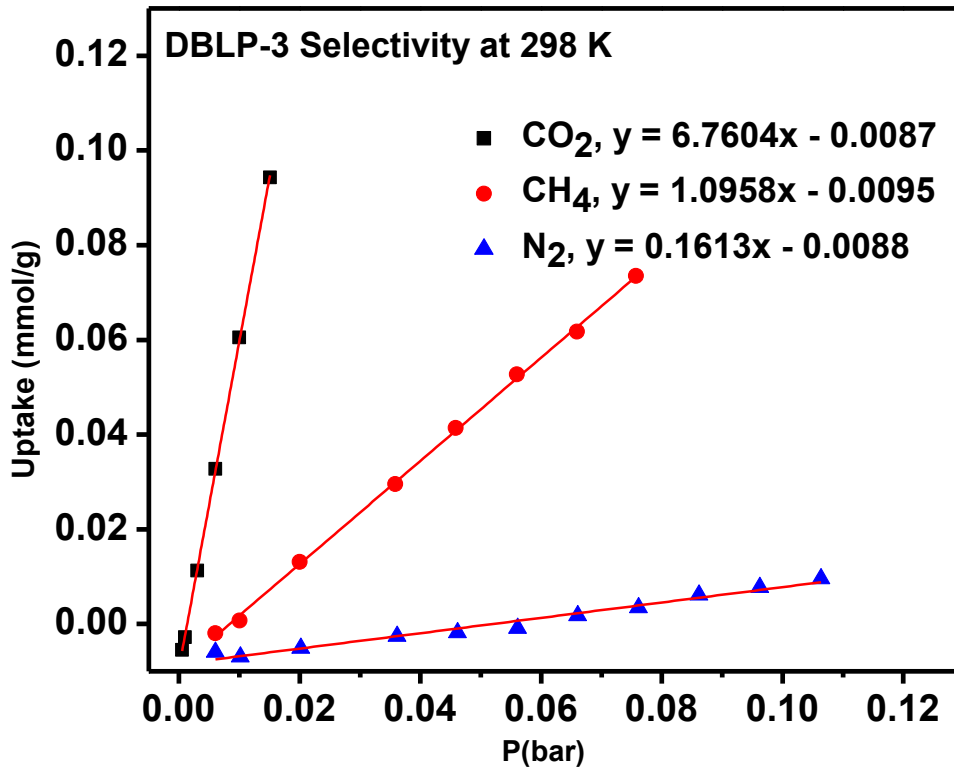


**Figure 3.29:** Adsorption selectivity of CO<sub>2</sub> over N<sub>2</sub> and CH<sub>4</sub> for DBLP-4 from initial slope calculations. CO<sub>2</sub> (black), CH<sub>4</sub> (red) and N<sub>2</sub> (blue) isotherms collected at and 298 K.

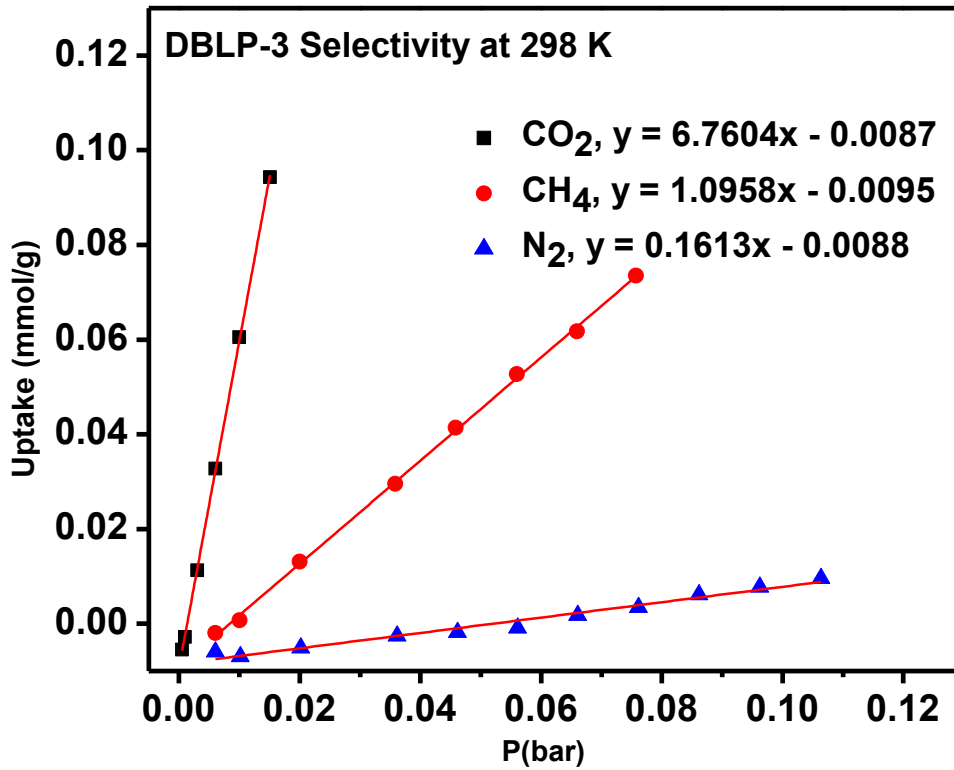


**Figure 3.30:** Adsorption selectivity of CO<sub>2</sub> over N<sub>2</sub> and CH<sub>4</sub> for DBLP-5 from initial slope calculations. CO<sub>2</sub> (black), CH<sub>4</sub> (red) and N<sub>2</sub> (blue) isotherms collected at and 298 K.

### 3.4. Conclusion

The first diazaborole-linked porous polymers (DBLPs) have been synthesized utilizing ortho-diamines and boronic acids. DBLPs exhibit (BET) surface areas in the range of 730 to 986  $\text{m}^2 \text{g}^{-1}$ . The highest storage capacity among newly synthesized DBLPs was observed for the  $\text{CO}_2$  uptake of DBLP-4 (4.5  $\text{mmol g}^{-1}$  at 273 K and 1 bar) and  $\text{H}_2$  uptake of DBLP-3 (2.13% at 77 K at 1 bar). The highest  $\text{CO}_2/\text{N}_2$  selectivity based on the initial slope calculation was recorded for DBLP-4 (51) at 298 K. To conclude we have successfully synthesized and characterized a new class of porous polymers named DBLPs and investigated their potential use in small gas uptake and separation. DBLPs can be synthesized through a condensation reaction between boronic acid building blocks and ortho-diamine-containing monomers with high surface areas and subnanometer pore structures. These thermally and chemically stable polymers can exhibit high  $\text{CO}_2$  uptake (up to 4.5  $\text{mmol g}^{-1}$ ) and exhibit good  $\text{CO}_2$  selectivity over  $\text{N}_2$  that can reach up to 51 at 1 bar and 298 K. In addition to high  $\text{CO}_2$  uptake and selectivity, DBLPs show considerable  $\text{H}_2$  uptake up to 2.3 wt.% at 77 K and 1 bar.



## Chapter 4

### Post-synthesis modification of diazaborole-linked polymers for enhanced chemical stability and CO<sub>2</sub> capture

#### 4.1. Introduction

Conjugated porous polymers have a few attractive features which make them suitable candidates for gas storage and separation, catalysis, drug delivery and ion sensing. These unique features include thermal and photo stability, flexibility, multiple recognition sites, and easy tuning of the polymer architecture by altering the starting precursors in shape, size and geometry. Among this large and diverse library of the porous materials COFs, PIMs, POFs, PPNs, and CMPs offer high porosity, physical and chemical stability and low density which make them attractive especially in small gas adsorption. Incorporation of electron deficient boron containing moieties into the polymeric structure leads to unique electronic and optical properties as well as creating possible interaction sites via open boron centers. COFs based on B-O, and B-N bonds have been reported in the literature, however accessibility of the open boron sites make most of the COFs unstable under atmospheric conditions. Keeping these key considerations in mind, we have designed and synthesized a new class of boron containing porous organic polymers named as diazaborole-linked polymers (DBLPs) prepared by a metal-free polymerization process that led to diazaborole ring linkages as described in the previous section. All DBLPs are moisture sensitive evidenced by surface area measurements after exposing them to the atmospheric conditions. In this study we treated the DBLP-4 with tetramethylammonium fluoride to improve the chemical stability of DBLPs against hydrolysis by taking the advantage of the Lewis acidity of the B sites.

## 4.2. Experimental Section

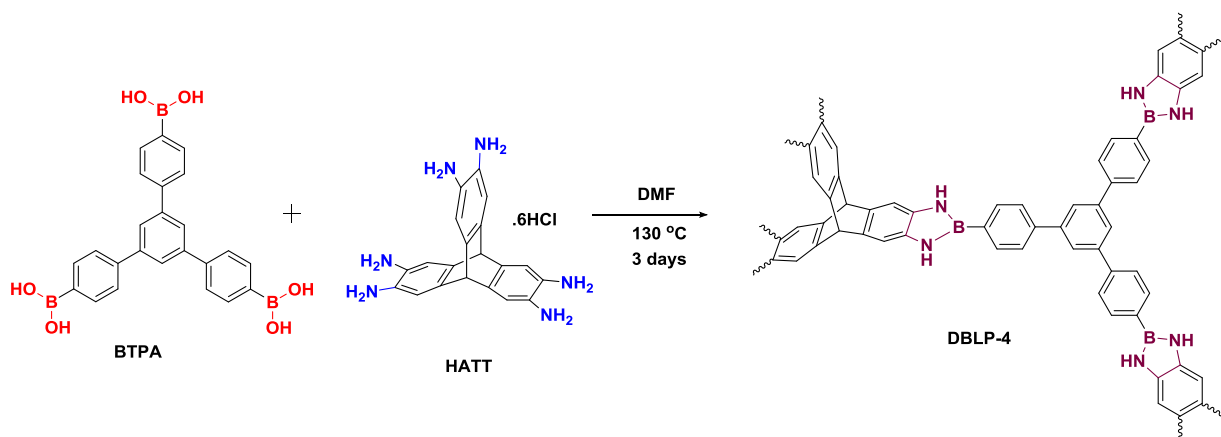
### 4.2.1 Materials and Methods

All starting materials, unless noted otherwise, were obtained from Aldrich Chemicals and used without further purification. Chromatographic separations were performed using standard column chromatography methods using silica gel purchased from Acros Organics (60 Å, 35-70 µm). Solvents were dried by distillation from Na (toluene) or Na/benzophenone (THF). 2, 3, 6, 7, 12, 13-hexahydroxytryptcene was prepared according to literature methods.<sup>55</sup> All products were handled under a nitrogen atmosphere using glovebox or Schlenk line techniques. Solution <sup>1</sup>H and <sup>13</sup>C NMR spectra were obtained on a Varian Mercury-300 MHz NMR spectrometer. Elemental analyses were performed by Midwest Microlab, Indianapolis, IN. Higher carbon and hydrogen contents may result from residual hydrocarbons in the cavities. FT-IR spectra were obtained using a Nicolet-Nexus 670 spectrometer equipped with Smart iTR™. Representative solid-state nuclear magnetic resonance (NMR) spectra were recorded at ambient temperature on a Bruker DSX-300 spectrometer using a Bruker magic angle spinning (MAS) probe with 4 mm (O.D.) 80 µL volume zirconia rotors with Kel-F drive caps at Spectral Data Services, Inc. SEM samples were prepared by dispersing the material onto a sticky carbon surface attached to a flat aluminum sample holder. The samples were then platinum coated using an EMS (Electron Microscopy Sciences) 550x Sputter Coater at 1x10<sup>-1</sup> mbar of pressure in a nitrogen atmosphere for 90 seconds while maintaining 20 mA of current. Samples were analyzed on a Zeiss EVO XVP Scanning Electron Microscope using the SEI detector with accelerating voltages ranging from 10 kV to 20 kV. Powder X-ray diffraction data were collected on a Panalytical X'pert pro multipurpose diffractometer (MPD). Samples were mounted on a sample holder and measured using Cu Kα radiation with a 2θ range of 1.5-35. Thermogravimetric analysis was obtained using a TA

Instruments TGA Q5000 analyzer with 50  $\mu$ L platinum pans to assess the thermal stability of the polymer. Experiments were run at a ramp rate of 5 K/minute under a nitrogen atmosphere. Argon sorption experiments were run using a Quantachrome Autosorb iQ2 analyzer. In a typical experiment, a sample was loaded into a 9 mm large bulb cell (Quantachrome) of known weight and then hooked up to Autosorb IQ2 and degassed at 120 °C for 12 h. The degassed sample was refilled with nitrogen, weighed and then transferred back to the analyzer. The temperatures for adsorption measurements were controlled by using bath of liquid nitrogen (77 K), liquid argon (87 K), or temperature controlled water bath (273 K and 298 K). Hydrogen isotherms were collected at 77 K and 87 K. Carbon dioxide and methane isotherms were collected at 273 and 298 K. Pore Size Distribution (PSD) was calculated using spherical/cylindrical pore (zeolite) NLDFT adsorption model.<sup>83</sup>

#### 4.2.2 Synthesis of DBLP-4

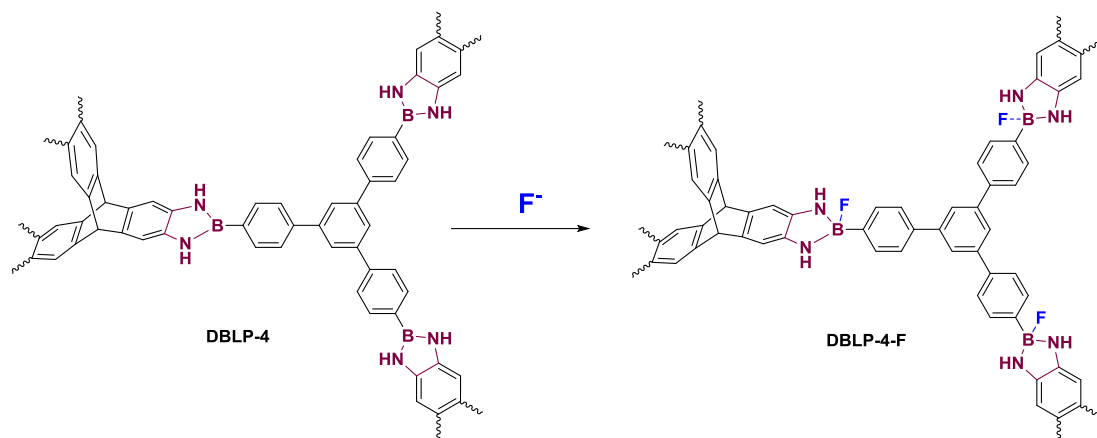
DBLP-4 was synthesized according to the method reported in chapter 3. The solid was then filtered and activated at 110 °C under reduced pressure for 16 hours to afford DBLP-4 (42 mg, 66 % yield) as a greenish solid. Anal. Calcd. for  $C_{44}H_{29}B_3N_6(6H_2O)$ : C, 67.56%; H, 5.28%; N, 10.74%. Found: C, 70.22%; H, 4.99%; N, 8.52%.



**Scheme 4.1:** Synthetic route for DBLP-4

#### 4.2.3 Synthesis of DBLP-4-F

A 30 mg (0.045mmol) DBLP-4 was activated at 110 °C under reduced pressure for 12 h then suspended in 10 ml dry acetone. Tetramethylammonium fluoride 12.5 mg (0.134mmol) was dissolved in 10 ml dry acetone and added to DBLP-4 suspension. The resulting mixture was stirred for 6 h under nitrogen atmosphere, then the brownish product was filtered over a medium glass frit and activated at 110 °C under reduced pressure for 12 h. DBLP-4-F (Scheme 4.2) was obtained as brownish solid (38 mg).



**Scheme 4.2:** Synthetic route for DBLP-4-F

### 4.3. Results and Discussion

#### 4.3.1 Synthesis and Characterization

DBLP-4 was prepared by the hydrothermal treatment of a mixture of 1,3,5-benzenetris(4-phenylboronic acid) (BTPA) and 2,3,6,7,14,15-hexaaminotriptycene in dry DMF for 3 days at 120 °C (Scheme 4.1). DBLP-4 was filtered under inert atmosphere and washed with anhydrous acetone/DMF then isolated and degassed at 120 °C/1.0 x 10<sup>-5</sup> Torr for 12 h. DBLP-4 was investigated by spectral and analytical methods which included FT-IR, solid-state <sup>11</sup>B and <sup>13</sup>C CP-MAS, elemental analysis, and UV-VIS studies. The formation of the diazaborole ring was first established by FT-IR studies (Figure 4.2). The FT-IR spectrum of DBLP-4 revealed N-H stretching at around 3400 cm<sup>-1</sup> (free N-H) and disappearance of the broad OH vibrations arising from the boronic acid units, while intense new bands appeared at 1423 cm<sup>-1</sup> (B-N, double bond character), 1171 cm<sup>-1</sup> (B-N, single bond character), and 1012 cm<sup>-1</sup> (B-C stretch), can be assigned to skeleton vibrations of the diazaborole ring.<sup>9, 97-99</sup> Upon addition of F<sup>-</sup> ions to DBLP-4 the 1171 cm<sup>-1</sup> signal assigned for single bond character of B-N increases in intensity, indicating the loss empty p orbital of the B for conjugation. The solid-state <sup>11</sup>B (Figure 4.3) revealed a broad signal ranging from 19.8

ppm to 8.0 ppm which falls in the reported tri-coordinate boron atoms<sup>100</sup>, whereas; in DBLP-4-F a sharp intense signal appears around 0.75 ppm which is in line with tetra-coordinate boron seen in amine-borane adducts or cycloborazanes (Figure 4.3).

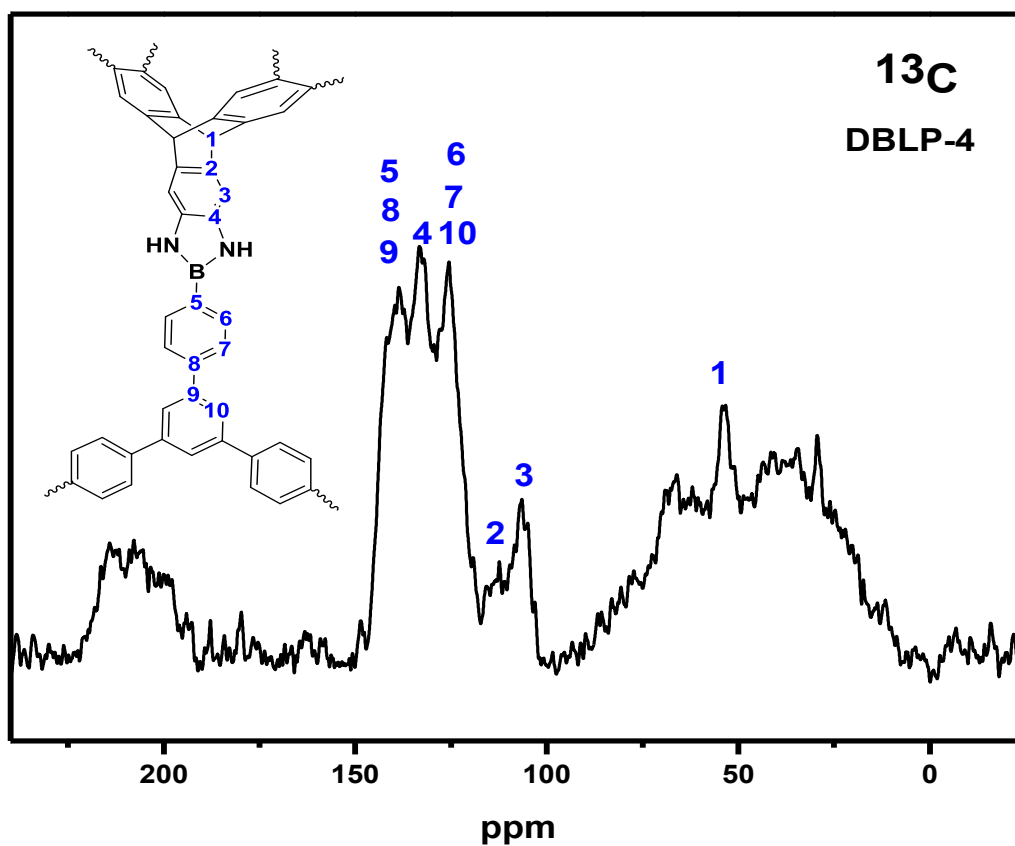


**Figure 4.1.** Solid-State <sup>13</sup>C CP-MAS NMR spectrum for DBLP-4.

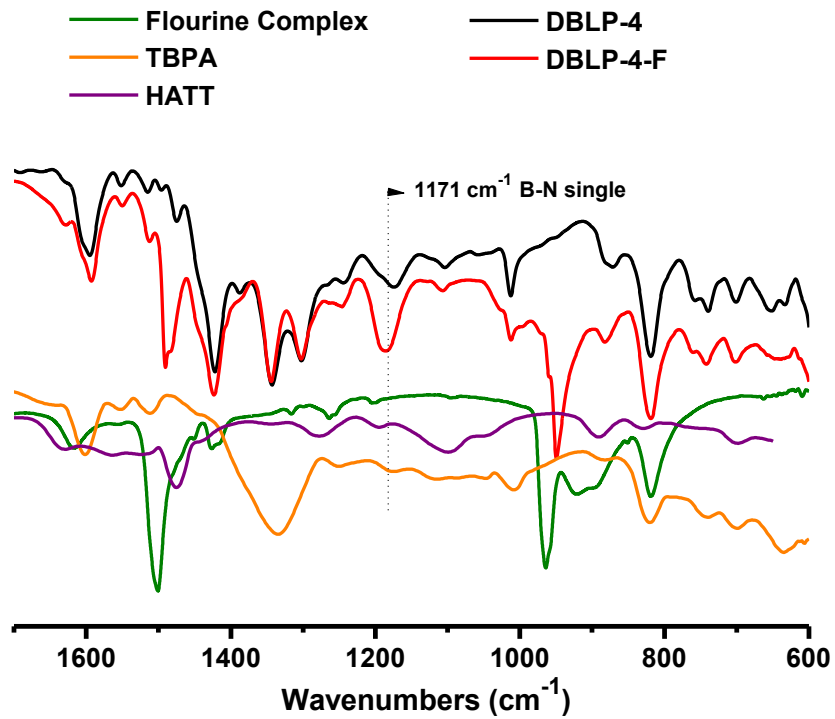
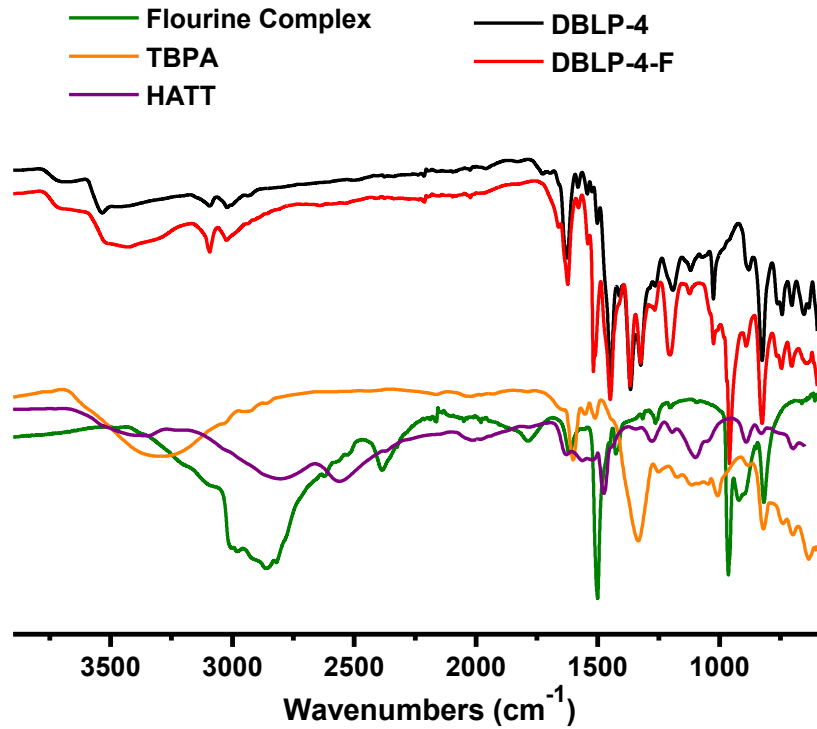
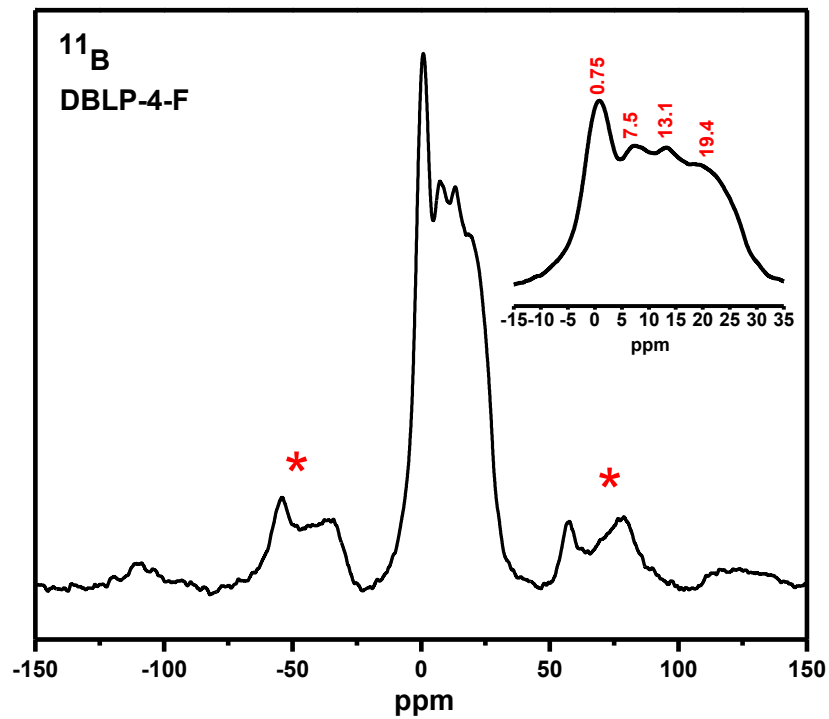
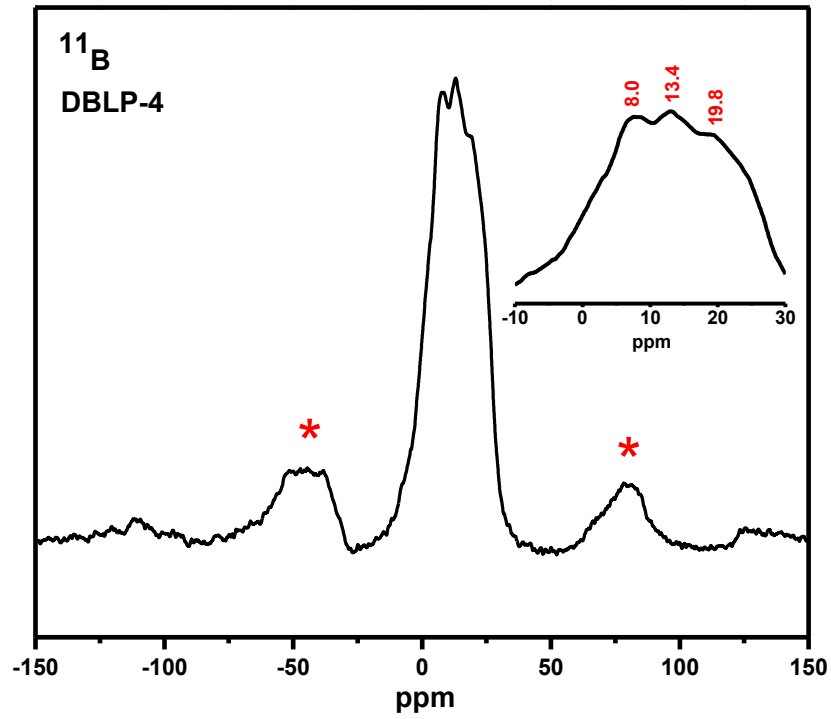


Figure 4.2. FT-IR spectrum for DBLP-4, BTPA and HATT.



**Figure 4.3.** Solid-state <sup>11</sup>B multiple quantum MAS (MQMAS) NMR spectrum of DBLP-4 and DBLP-4-F; asterisks denote spinning-side bands.



Scanning electron microscopy (SEM) of the polymers revealed aggregated particles of variable size in the range of ~0.4 to ~1.0  $\mu\text{m}$  (Figure 4.4). The  $^{13}\text{C}$  CP-MAS NMR spectra of DBLP-4 confirm their successful synthesis with the characteristic peaks triptycene aliphatic C-H, triptycene aromatic C-H, aromatic C-H, and aromatic C peaks are found to be at 54,107,113,127, and 141 ppm, respectively (Figure 4.1) DBLP-4 showed amorphous nature as evidenced by powder-XRD studies (Figure 4.5)



**Figure 4.4.** Scanning Electron Microscopy (SEM) Imaging of DBLP-4: A sample DBLP-4 was prepared by dispersing the material onto a sticky carbon surface attached to a flat aluminum sample holder. The sample was then gold coated using an EMS (Electron Microscopy Sciences) 550x Sputter Coater at  $1 \times 10^{-1}$  mbar of pressure in a nitrogen atmosphere for 90 seconds while maintaining 20 mA of current.

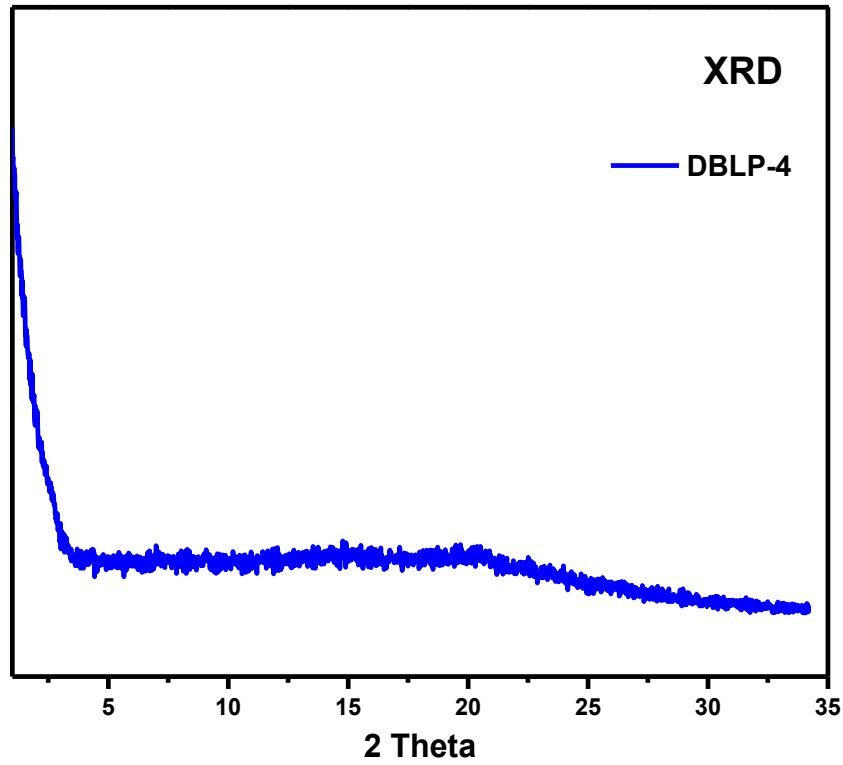


**Figure 4.5.** Powder X-ray Diffraction Analysis of DBLP-4: Powder X-ray diffraction data of DBLP-4 were collected on a Panalytical X'pert Pro Multipurpose Diffractometer (MPD). Samples were mounted on a zero background sample holder measured in transmission mode using Cu K $\alpha$  radiation with a  $2\theta$  range of 1.5-35°.

Addressing the chemical stability of porous adsorbents remains a very important aspect of adsorbents design and development. While the use of boronic acids as precursors for porous COFs and DBLPs has been effective in obtaining low-density polymers, the trigonal planar geometry about B renders COFs and DBLPs susceptible for hydrolysis by moisture. Nucleophilic attack by water or acidic molecules typically encountered in flue gas for example can cause framework collapse and hence loss of porosity. In fact, it is the coordinatively unsaturated nature of B in COFs that enables reversible B-N and B-O bond formation processes needed for the isolation of crystalline networks. At the electronic level, the high Lewis acidity and very effective orbital interaction of B with conjugated  $\pi$ -electron systems make B-containing organic molecules and networks useful in optoelectronics. The fluoride ion is very small and a strong Lewis base, it can easily coordinate to the boron atom in the polymer without any steric hindrance. Tetramethylammonium fluoride has been widely used as a convenient source for  $F^-$ . The formation of the B-F bond can be tracked by using UV-Vis studies as the formation of such bond disrupts the  $\pi$ -electron conjugation. Furthermore, the counter cations ( $Et_4N^+$ ) are expected to occupy the voids of DBLP-4 which will reduce their pore size distribution and make the channels highly charged. Noteworthy, functionalization of the pores with fluoro moieties can lead to improvement in  $CO_2$  uptake capacity and selectivity due to dipole-quadropole interactions between fluoro sites and  $CO_2$ .<sup>125-127</sup> Several MOFs and POPs functionalized with fluorocarbons exhibit enhanced  $CO_2$  uptake capacity and high isosteric heat of adsorption ( $Q_{st}$ ) for  $CO_2$ .<sup>126, 128-130</sup> Likewise, MOFs functionalized with fluorinated ions such as  $PF_6^-$ ,  $SiF_6^{2-}$ , and  $BF_4^-$  show moderate to high  $Q_{st}$  values for  $CO_2$  (34-45 kJ/mol).<sup>131, 132</sup> To explore the porosity of both DBLP-4 and DBLP-4-F, the porosity measurements of DBLPs were investigated by Argon at 87 K. The fully reversible isotherms show a rapid uptake at low pressure ( $P/P_0 = 0$  to 0.05 bar). Applying the Brunauer-

Emmett-Teller (BET) model to the sorption branch within the pressure range of  $P/P_0 = 0.05-0.15$  resulted in surface area of  $904 \text{ m}^2\text{g}^{-1}$  for DBLP-4 (Figure 4.6). DBLP-4 was exposed to air for 2 h to check its stability towards moisture; however, it lost 20% of surface area, presumably due to the open boron sites. After treating DBLP-4 with tetramethylammonium fluoride (DBLP-4-F), surface area of the DBLP-4-F was very low  $\text{N}_2$  uptake at 77 K, presumably due to blocked pore openings by the large counter cations ( $\text{Et}_4\text{N}^+$ ). Thus  $\text{CO}_2$  isotherms for DBLP-4-F and moisture exposed samples were collected at 273 K (Figure 4.9) and data was used for surface area calculations since  $\text{CO}_2$  can penetrate ultra-small pores (0.7 nm). The initial surface area of DBLP-4-F ( $315 \text{ m}^2/\text{g}$ ) seems to be unaffected upon exposure to moisture under ambient atmosphere for 24 h and 48 h. These results indicate that the stability of DBLPs can be enhanced by capping the open boron sites with fluoride ions. We were expecting to see an increase in the  $\text{CO}_2$  uptake while we have positive charge decorated pore walls. Unfortunately,  $\text{CO}_2$  uptake decreased upon addition of fluoride ions. Presumably, it is because of the decreased surface area by large counter cations in the pores.

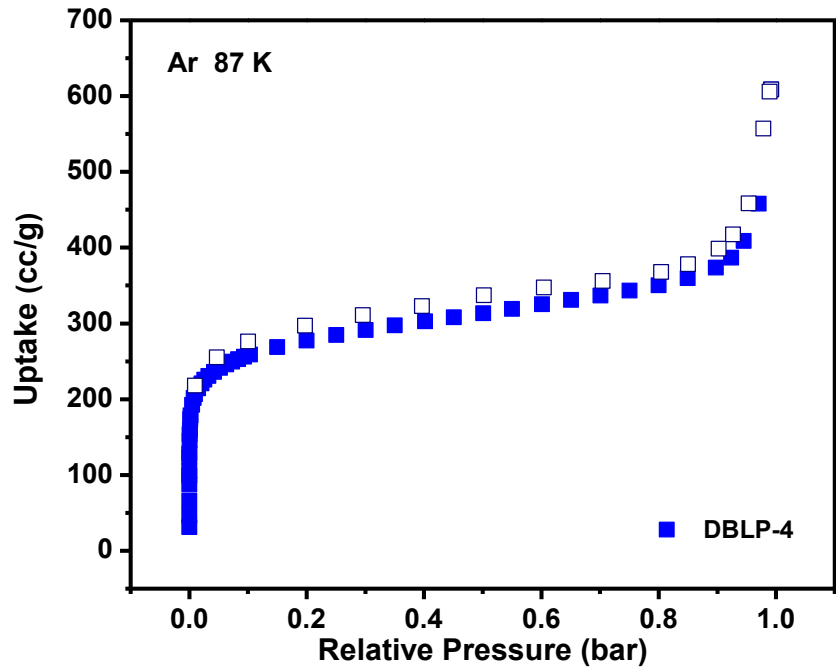


**Figure 4.6.** Argon isotherm for DBLP-4 measured at 87 K. The filled squares are adsorption points and the empty squares are desorption points.

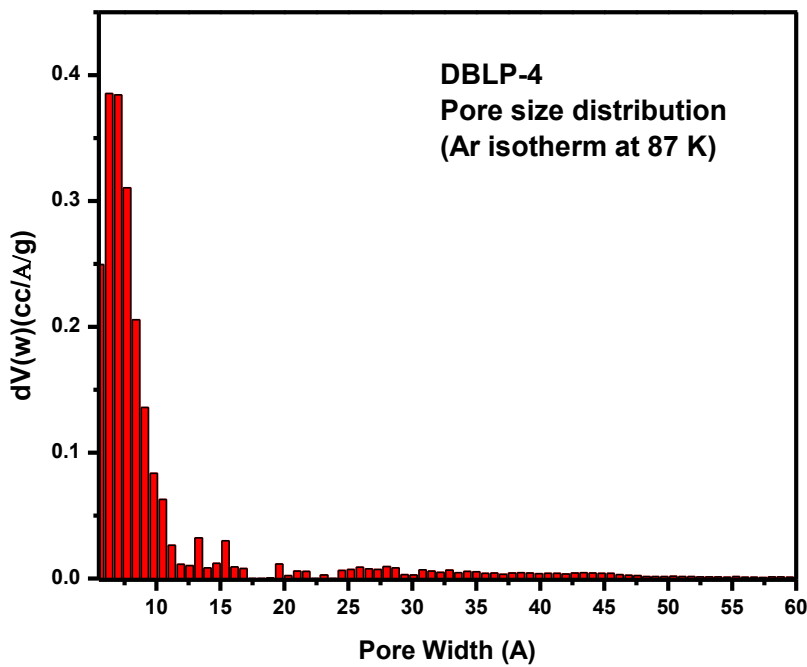


**Figure 4.7.** Pore Size Distribution (PSD) for DBLP-4 from NLDFT.

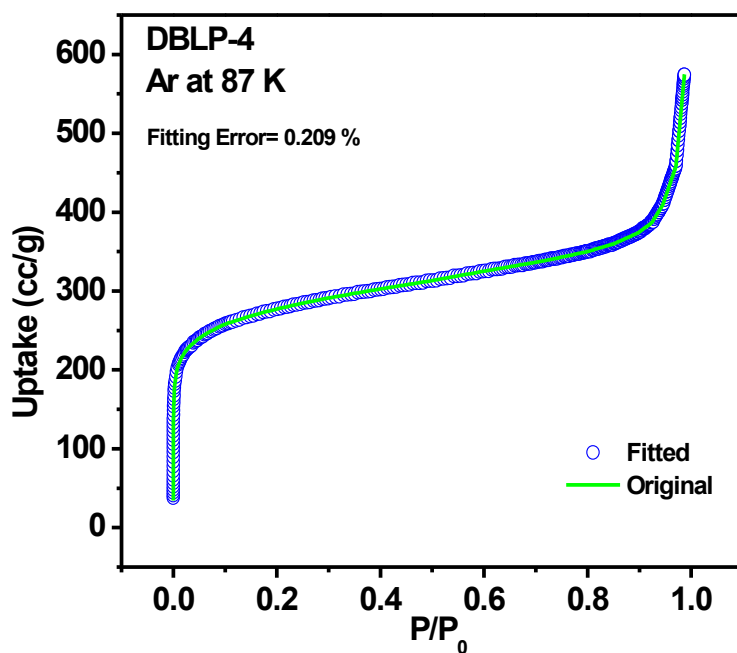


**Figure 4.7.** NLDFT calculated isotherm for DBLP-4 overlaid with the experimental argon isotherm. A fitting error less than 1% indicates validity of the model.

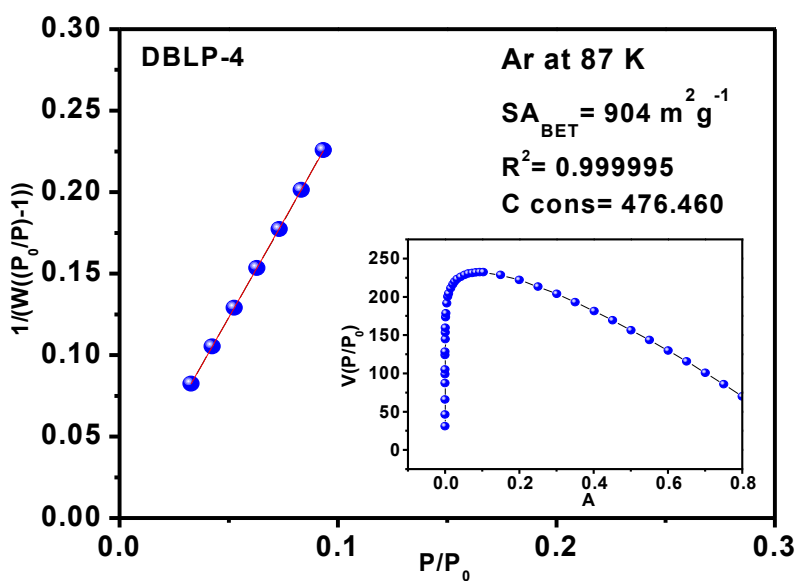


**Figure 4.8.** Multipoint BET plot for DBLP-4 calculated from the argon adsorption.

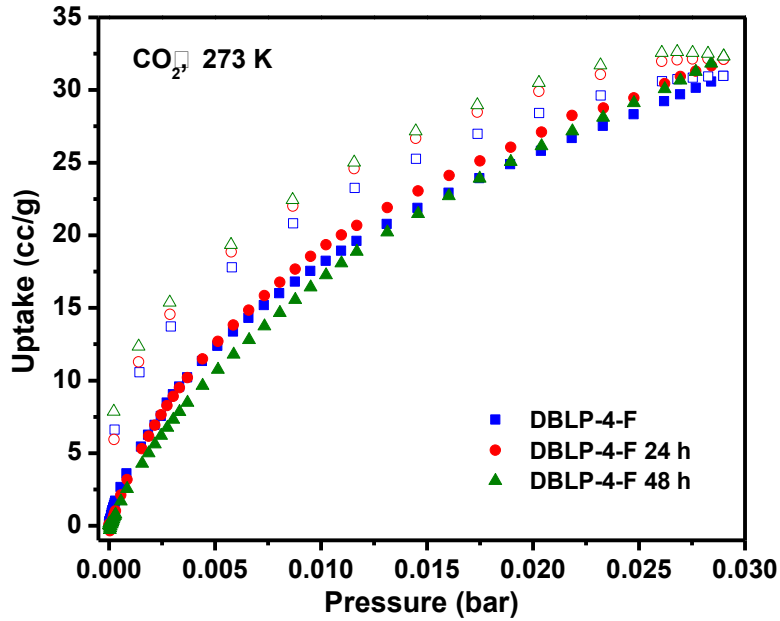


**Figure 4.9.** CO<sub>2</sub> isotherms for DBLP-4-F as synthesized, 24 h and 48 h exposed to air at 273K. The filled points are adsorption and the empty points are desorption.

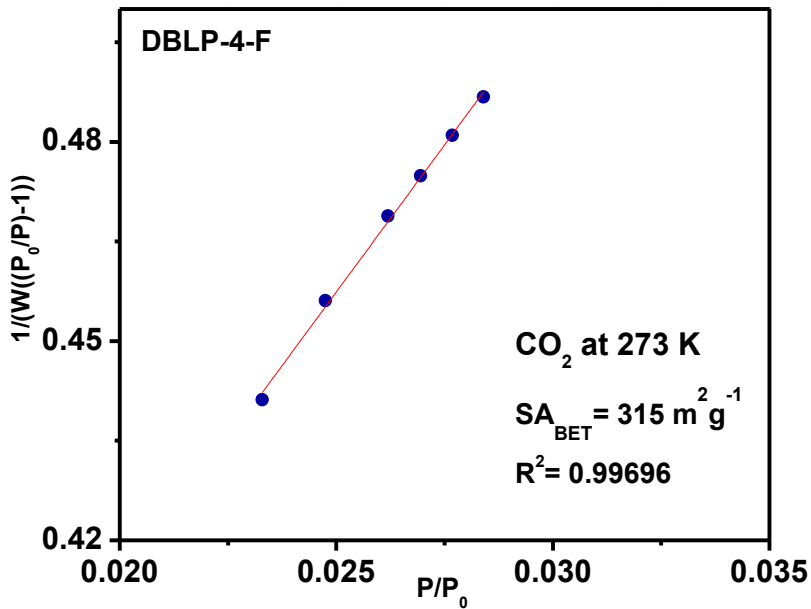


**Figure 4.10.** Multipoint BET plots for DBLP-4-F as synthesized calculated with CO<sub>2</sub> at 273K

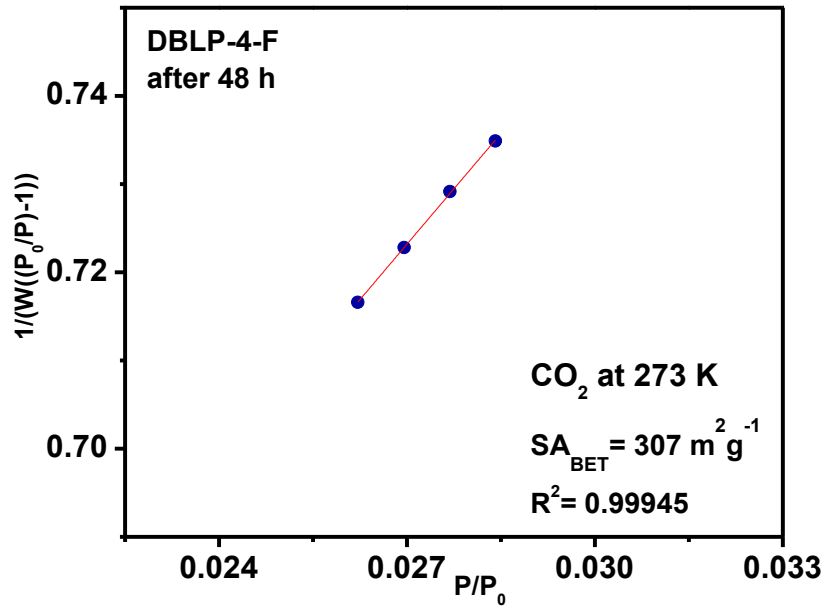
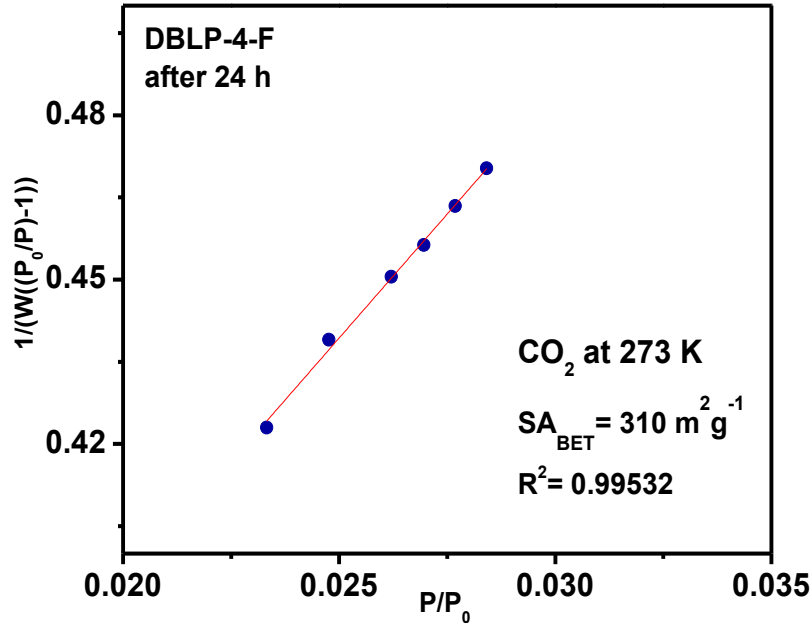


**Figure 4.11.** Multipoint BET plots for DBLP-4-F, which are 24 h and 48 h exposed to air that are calculated from the CO<sub>2</sub> adsorption.



### 4.3.2 UV-VIS Studies

To characterize DBLP-4 and DBLP-4-F, we studied the UV-Vis properties of triphenyl boronic acid, hexaaminotriptycene, DBLP-4, DBLP-4-F and self-condensation product of the triphenyl boronic. One concern was the possible self-condensation of the triphenyl boronic acid during the synthesis of DBLP-4. As clearly seen in the Figures 4.13 and 4.14 excitation and emission peaks for the starting materials and products are distinctively separate from each other. UV-visible absorption spectra were recorded using a Cary 6000i UV-Vis-NIR spectrophotometer (Agilent Technologies) by using 10 mm quartz cuvettes. For the solution UV-visible absorption and emission spectra, ~0.005 g of the polymers were dispersed in DMF and sonicated for 2 min, and the solution was allowed to settle for a couple of minutes. Supernatant of the solution was used to carry out the UV-vis measurements.

We have recorded the photoluminescence, and photoluminescence excitation spectra of the DBLP-4 and corresponding monomers to investigate the electronic structure of DBLP-4. The absorption spectrum of DBLP-4 shows excitonic features at 340 nm, 275 nm, and a low intensity hump at 314 nm. In contrast, corresponding monomers exhibit well-defined peaks at 320 nm for BTPA, in addition 328 nm and a low intensity shoulder at 275 nm for HATT. For the tetra-amine building block, corresponding peaks can be assigned to  $n-\pi^*$  electronic transitions.<sup>133</sup> Similarly, the observed peaks for the DBLP-4 at 340, 314, and 275 nm likely arise from  $\pi-\pi^*$  optical transitions.<sup>133</sup>

Upon exciting the DBLP-4 polymer with 340 nm in DMF, green emission with broad peak ranging from 350 to 680 nm was observed (Figure 4.12). Compared to both triptycene and the triphenyl boronic acid, the excitation peak of DBLP-4 exhibits a bathochromic shift (Figure 4.13-14). Similarly, the emission peak in DBLP-4 is showing a red shift. The red shift in both excitation

and emission indicates an increased conjugation due to the formation of a diazaborole link involving one of the benzene rings from triptycene and the boron part of the triphenyl boronic acid.

Although it was not the main objective of the project, it is worth to mention that DBLP-4 can be used as a fluoride ion sensor according to the results we obtained from UV-Vis studies. As can be seen in Figure 4.12, upon incremental addition of fluoride anion to DBLP-4 suspension, the intensity of the DBLP-4 peak at 485 nm gradually increased. This enhancement of fluorescence of DBLP-4 polymer is attributed to the coordination of fluoride ion with the boron in the polymer. This coordination of fluoride is not affecting the conjugation of the DBLP-4 polymer, hence no peak shifts in emission was observed.<sup>134</sup> Boron is  $sp^2$  hybridized with an empty p orbital which is populated by the donation of an electron pair from the fluoride ion. Thus, the boron in the DBLP-4 polymer acts as a Lewis acid. As fluoride ion is very small and a strong Lewis base, it can easily coordinate to the boron atom in the polymer without any steric hindrance offered by the bulky triphenyl groups and the triptycene. Furthermore, fluoride ion is known to cause cleavage of bond between Si-O/Si-C<sup>135, 136</sup> and thus can be detected. The cleavage of B-N bond in DBLP-4 has been excluded, as there is no shift in the emission peak while fluoride ion titration was carried out. The monomers triphenyl boronic acid and the triptycene emits at 361 nm and 350 nm, respectively (Figure 4.13-14).

Apart from the chemical stability of the DBLP-4 polymer upon addition of fluoride, it is also stable to light without any degradation as evidenced by the sample being exposed to UV light for 40 minutes (Figure 4.15), this stability is most likely imparted by B-F bond formation.

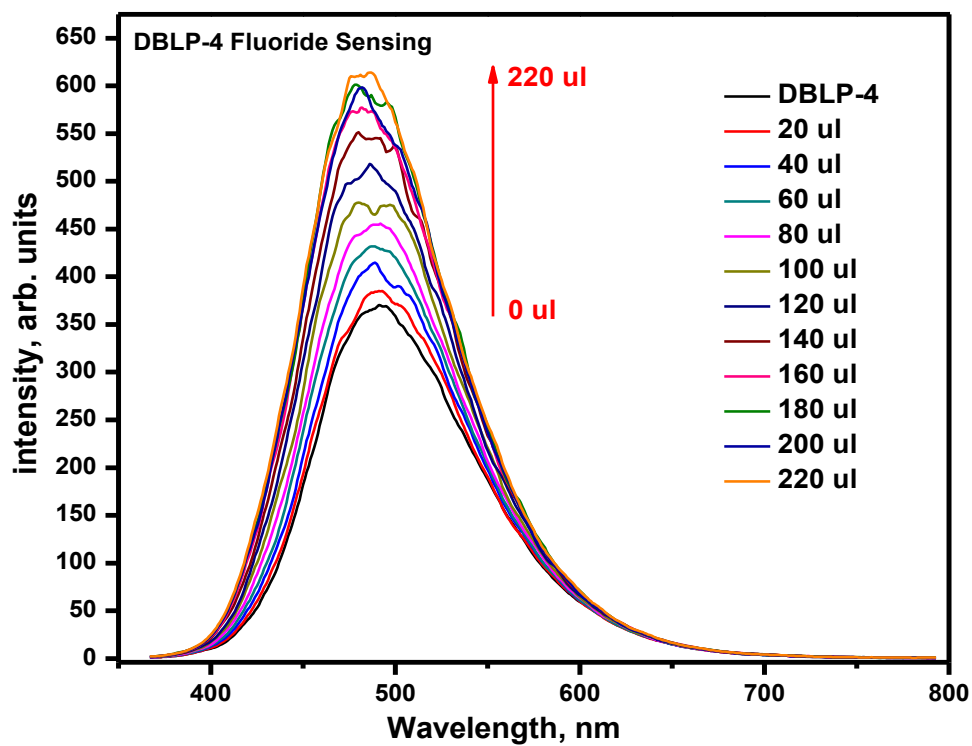


**Figure 4.12.** Fluorescence enhancement of the DBLP-4 polymer upon the incremental addition of the  $10^{-2}$  M fluoride anion in dimethylformamide.

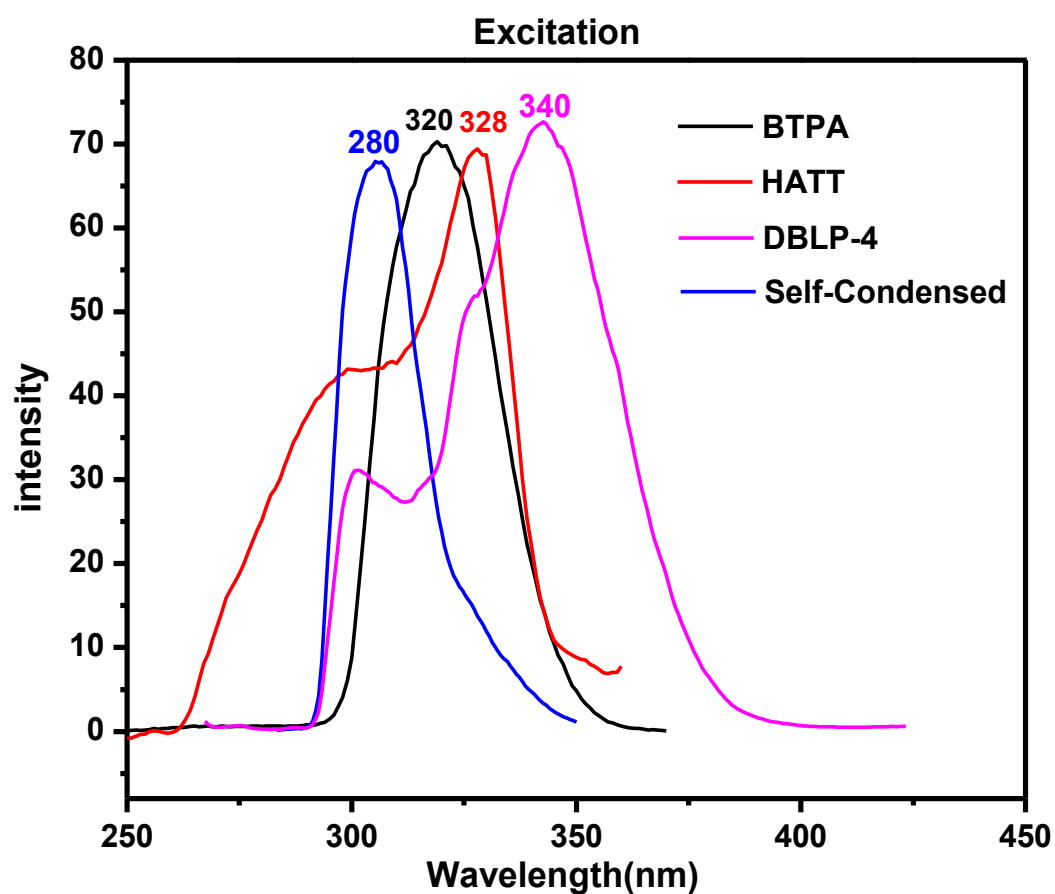


**Figure 4.13.** Excitation Properties of BTPA, HATT, DBLP-4 and Self-Condensed BTPA in DMF.

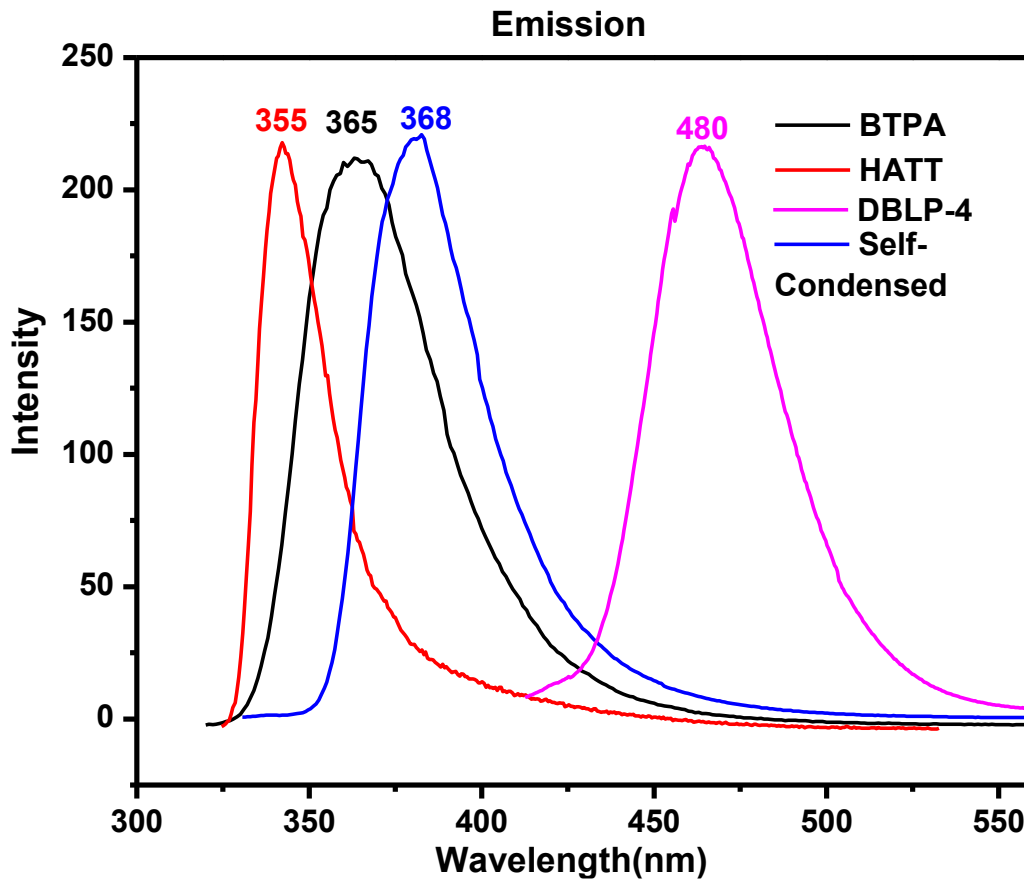


**Figure 4.14.** Emission Properties of BTPA, HATT, DBLP-4 and Self-Condensed BTPA in DMF.

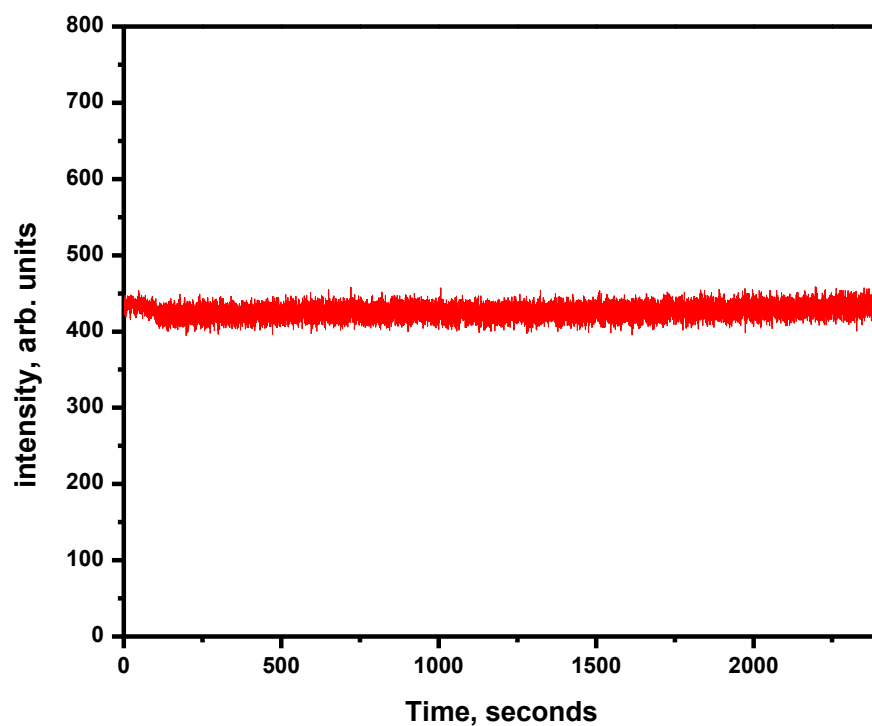


**Figure 4.15.** Photobleaching experiment of DBLP-4 polymer in dimethylformamide upon exposure to UV light for 40 minutes.

#### 4.4 Conclusion

In this study, we have synthesized diazaborole linked polymers and investigated their stability under atmospheric conditions and upon treatment with fluoride ions. The moisture stability of DBLP-4 is dramatically increased upon treating with fluoride ions which leads to DBLP-4-F formation. The fluoride ions coordinate to the boron sites and prevent B-N bond hydrolysis by moisture. In addition to the moisture stability, DBLP-4-F showed very high light stability without any degradation upon irradiation with UV light. The outcome of this study indicates that DBLPs can be post-synthetically modified to improve their stability.

## Chapter 5

### Concluding Remarks

The research presented in this dissertation entails the design and synthesis of porous polymers and application in the small gas storage and separation. Two classes of porous polymers; diazaborole linked polymers (DBLPs) and covalent organic frameworks (COFs) were designed, synthesized and investigated for potential use in gas storage and separation applications. The important aspects of this dissertation are summarized below.

High atmospheric CO<sub>2</sub> concentration is the greatest factor presently contributing to global warming. An immediate action is required to solve this issue. Switching to energy sources other than fossil fuels is one option but finding alternative sources that are abundant and renewable remains a great challenge. Furthermore, fossil fuels consumption will continue to increase in future which will lead to increased CO<sub>2</sub> release and thus CO<sub>2</sub> capture and sequestration (CCS) is vital. Porous organic polymers are among the promising candidates for gas storage because of their unique properties, such as low density, superior stability, adjustable pore size and functionality, very high surface area and recyclability. Our recently reported porous polymer families; BILPs and ALPs have shown impressive CO<sub>2</sub> uptake and can selectively capture CO<sub>2</sub> over N<sub>2</sub> and CH<sub>4</sub>. However, due to their amorphous structure, which limits control over pore shape and size and lead to moderate surface area, their CO<sub>2</sub> capture performances under elevated pressure remains modest. On the other hand, hydrogen is a promising replacement for fossil fuels, because of its high energy capacity, abundance and cleanness, with only water being the by-product after combustion. However, due to the high volumetric density, storage is a real challenge for on-board applications. In the second chapter of the dissertation we introduced a new porous organic polymer, called triptycene-derived covalent organic framework (TDCOF-5), which has highly ordered



microcrystalline structure and a very high surface area of  $2497 \text{ m}^2 \text{ g}^{-1}$ . TDCOF-5 was synthesized through a condensation reaction between 1,4-benzenediboronic acid and hexahydroxytritycene which leads to boronate ester linkage formation. Because of the unique structure of the triptycene, it is known to allow for a high degree of internal free volume, which increases the number of exposed latent edges of building units and thus the interaction with gas molecules. TDCOF-5 has the highest  $\text{H}_2$  uptake under 1 atm at 77K (1.6%) among all known 2D and 3D COFs derived from B–O bond formation and moderate  $\text{CO}_2$  uptake ( $2.1 \text{ mmol g}^{-1}$ ) with the  $Q_{st}$  values of  $6.6 \text{ kJ mol}^{-1}$  and  $21.8 \text{ kJ mol}^{-1}$ , respectively. However,  $\text{CO}_2$  and  $\text{H}_2$  uptakes fall behind the practical application targets. One disadvantage of COFs is their high moisture sensitivity due to the vacant boron p-orbital which allow for nucleophilic attack by water. To overcome this problem, we have designed a new type of porous organic polymer, named diazaborole-linked polymers (DBLPs) and successfully developed a synthetic procedure which was presented in the third chapter. In the Diazaborole-Linked Polymers (DBLPs), including a bulky group on nitrogen or boron will retard the interaction of the incoming water molecules with the vacant boron p-orbital making these polymers more chemically robust than COFs. In order to mask the open boron sites, we have used fluoride ions. As the fluoride ion is very small and a strong Lewis base, it can easily coordinate to the boron atom in the polymer without any steric hindrance. One other advantage of diazaborole decorated pore channels is having high number of accessible nitrogen interaction sites since it has been evident that nitrogen rich porous structure has enhanced gas uptakes, especially towards  $\text{CO}_2$  through hydrogen bonding. For this purpose, 2, 3, 6, 7, 14, 15-hexaaminotriptycene (HATT) hexahydrochloride was synthesized and reacted with different boronic acid derivatives to produce three different porous polymer architectures. The 2, 3, 6, 7, 14, 15-hexaaminotriptycene (HATT) hexahydrochloride combined with 1,4-benzenediboronic acid (BDBA), 1,3,5-benzenetriboronic

acid (BTBA), and tetra(4-dihydroxyborylphenyl)methane (TBPM) to afford DBLP-3, -4 and -5 with the surface areas of 730, 904, and 986 m<sup>2</sup> g<sup>-1</sup>, respectively. DBLP-3, -4 and -5 have high CO<sub>2</sub> uptakes (158.5, 198, and 171.5 mg g<sup>-1</sup>) at 1 bar 273 K which compare well with the best porous organic polymers in the field.

Overall, we have demonstrated the synthesis of highly porous covalent organic framework and diazaborole linked polymers by solvothermolysis of a variety of organic building units and investigated their gas storage performance under ambient pressure and cryogenic conditions. Stability towards ambient moisture is problematic for most of the boron containing porous polymers, yet we designed a new method to stabilize them by capping the boron open sites with fluoride ions. The work presented here signifies a major advance in the development of porous materials, making DBLPs among attractive candidates for clean energy applications. Future work in this field should focus on new synthetic routes that enable higher porosity levels as well as the isolation of crystalline frameworks as in the case of B-O linked COFs.

## References

1. Côté, A. P.; Benin, A. I.; Ockwig, N. W.; O'Keeffe, M.; Matzger, A. J.; Yaghi, O. M., Porous, Crystalline, Covalent Organic Frameworks. *Science* **2005**, *310*, (5751), 1166-1170.
2. El-Kaderi, H. M.; Hunt, J. R.; Mendoza-Cortés, J. L.; Côté, A. P.; Taylor, R. E.; O'Keeffe, M.; Yaghi, O. M., Designed Synthesis of 3D Covalent Organic Frameworks. *Science* **2007**, *316*, (5822), 268-272.
3. Cote, A. P.; El-Kaderi, H. M.; Furukawa, H.; Hunt, J. R.; Yaghi, O. M., Reticular synthesis of microporous and mesoporous 2D covalent organic frameworks. *Journal of the American Chemical Society* **2007**, *129*, (43), 12914-+.
4. Hunt, J. R.; Doonan, C. J.; LeVangie, J. D.; Cote, A. P.; Yaghi, O. M., Reticular synthesis of covalent organic borosilicate frameworks. *Journal of the American Chemical Society* **2008**, *130*, (36), 11872-11873.
5. Ding, S.-Y.; Wang, W., Covalent organic frameworks (COFs): from design to applications. *Chem. Soc. Rev.* **2013**, *42*, (2), 548-568.
6. Makal, T. A.; Li, J.-R.; Lu, W.; Zhou, H.-C., Methane storage in advanced porous materials. *Chem. Soc. Rev.* **2012**, *41*, (23), 7761-7779.
7. Weber, L.; Böhlring, L., The role of 2,3-dihydro-1-H-1,3,2-diazaboroles in luminescent molecules. *Coordin Chem Rev* **2015**, *284*, (0), 236-275.
8. Furukawa, H.; Yaghi, O. M., Storage of Hydrogen, Methane, and Carbon Dioxide in Highly Porous Covalent Organic Frameworks for Clean Energy Applications. *J. Am. Chem. Soc.* **2009**, *131*, (25), 8875-8883.

9. Nishida, J.-i.; Fujita, T.; Fujisaki, Y.; Tokito, S.; Yamashita, Y., Diazaboroles with quinone units: hydrogen bonding network and n-type FETs involving a three-coordinate boron atom. *J. Mater. Chem.* **2011**, *21*, (41), 16442-16447.
10. Kitagawa, S.; Kitaura, R.; Noro, S.-i., Functional Porous Coordination Polymers. *Angew. Chem. Int. Ed.* **2004**, *43*, (18), 2334-2375.
11. Colson, J. W.; Dichtel, W. R., Rationally synthesized two-dimensional polymers. *Nat Chem* **2013**, *5*, (6), 453-465.
12. Sumida, K.; Bloch, E. D.; Mason, J. A.; Herm, Z. R.; Queen, W. L.; Rogow, D. L.; Brown, C. M.; Long, J. R., Hydrogen storage in metal-organic frameworks. *Abstr Pap Am Chem S* **2012**, *244*.
13. Mason, J. A.; Sumida, K.; Herm, Z. R.; Krishna, R.; Long, J. R., Evaluating metal-organic frameworks for post-combustion carbon dioxide capture via temperature swing adsorption. *Energy Environ. Sci.* **2011**, *4*, (8), 3030-3040.
14. Dinca, M.; Dailly, A.; Tsay, C.; Long, J. R., Expanded sodalite-type metal-organic frameworks: Increased stability and H<sub>2</sub> adsorption through ligand-directed catenation. *Inorg. Chem.* **2008**, *47*, (1), 11-13.
15. Dawson, R.; Cooper, A. I.; Adams, D. J., Nanoporous organic polymer networks. *Prog. Polym. Sci.* **2012**, *37*, (4), 530-563.
16. Greene, D. L.; Kahn, J. R.; Gibson, R. C., Fuel economy rebound effect for US household vehicles. *Energy J* **1999**, *20*, (3), 1-31.
17. Sumida, K.; Rogow, D. L.; Mason, J. A.; McDonald, T. M.; Bloch, E. D.; Herm, Z. R.; Bae, T.-H.; Long, J. R., Carbon Dioxide Capture in Metal–Organic Frameworks. *Chem. Rev.* **2011**, *112*, (2), 724-781.

18. Tokushige, K.; Akimoto, K., Role and Issues of CCS in Long-term Sustainable Emission Reductions and toward Sustainable Development. *Energy Proced* **2011**, *4*, 5889-5894.
19. <http://www.worldcoal.org/>.
20. Züttel, A., Materials for hydrogen storage. *Materials Today* **2003**, *6*, (9), 24-33.
21. Schlapbach, L.; Züttel, A., Hydrogen-storage materials for mobile applications. *Nature* **2001**, *414*, (6861), 353-358.
22. Xiang, Z.; Cao, D., Porous covalent-organic materials: synthesis, clean energy application and design. *J. Mater. Chem. A* **2013**, *1*, (8), 2691-2718.
23. Songolzadeh, M.; Soleimani, M.; Takht Ravanchi, M.; Songolzadeh, R., Carbon Dioxide Separation from Flue Gases: A Technological Review Emphasizing Reduction in Greenhouse Gas Emissions. *The Scientific World Journal* **2014**, *2014*, 34.
24. D'Alessandro, D. M.; Smit, B.; Long, J. R., Carbon Dioxide Capture: Prospects for New Materials. *Angew. Chem. Int. Ed.* **2010**, *49*, (35), 6058-6082.
25. Drage, T. C.; Snape, C. E.; Stevens, L. A.; Wood, J.; Wang, J.; Cooper, A. I.; Dawson, R.; Guo, X.; Satterley, C.; Irons, R., Materials challenges for the development of solid sorbents for post-combustion carbon capture. *J. Mater. Chem.* **2012**, *22*, (7), 2815-2823.
26. Gottschalk, A., CACHET: R&D of Pre-combustion CO<sub>2</sub> Capture Technologies Treating Gaseous Fuels. *Chem-Ing-Tech* **2007**, *79*, (9), 1321-1322.
27. Benson, S. M.; Surles, T., *Proc. IEEE* **2006**, *94*, 1795.
28. Chiesa, P.; Consonni, S.; Kreutz, T.; Robert, W., Co-production of hydrogen, electricity and CO<sub>2</sub> from coal with commercially ready technology. Part A: Performance and emissions. *Int. J. Hydrogen Energy* **2005**, *30*, (7), 747-767.

29. Stolaroff, J. K.; Keith, D. W.; Lowry, G. V., Carbon Dioxide Capture from Atmospheric Air Using Sodium Hydroxide Spray. *Environ. Sci. Technol.* **2008**, *42*, (8), 2728-2735.
30. Rochelle, G. T., Amine Scrubbing for CO<sub>2</sub> Capture. *Science* **2009**, *325*, (5948), 1652-1654.
31. Keskin, S.; van Heest, T. M.; Sholl, D. S., Can Metal–Organic Framework Materials Play a Useful Role in Large-Scale Carbon Dioxide Separations? *ChemSusChem* **2010**, *3*, (8), 879-891.
32. Konduru, N.; Lindner, P.; Assaf-Anid, N. M., Curbing the greenhouse effect by carbon dioxide adsorption with Zeolite 13X. *Aiche J* **2007**, *53*, (12), 3137-3143.
33. Okubo, T.; Inoue, H., Introduction of specific gas selectivity to porous glass membranes by treatment with tetraethoxysilane. *Journal of Membrane Science* **1989**, *42*, (1–2), 109-117.
34. Bastos-Neto, M.; Patzschke, C.; Lange, M.; Mollmer, J.; Moller, A.; Fichtner, S.; Schrage, C.; Lassig, D.; Lincke, J.; Staudt, R.; Krautscheid, H.; Glaser, R., Assessment of hydrogen storage by physisorption in porous materials. *Energy Environ. Sci.* **2012**, *5*, (8), 8294-8303.
35. Zhao, H.; Jin, Z.; Su, H.; Zhang, J.; Yao, X.; Zhao, H.; Zhu, G., Target synthesis of a novel porous aromatic framework and its highly selective separation of CO<sub>2</sub>/CH<sub>4</sub>. *Chem. Commun.* **2013**, *49*, (27), 2780-2782.
36. Jin, Y.; Zhu, Y.; Zhang, W., Development of organic porous materials through Schiff-base chemistry. *CrystEngComm* **2013**, *15*, (8), 1484-1499.
37. Furukawa, H.; Ko, N.; Go, Y. B.; Aratani, N.; Choi, S. B.; Choi, E.; Yazaydin, A. Ö.; Snurr, R. Q.; O’Keeffe, M.; Kim, J.; Yaghi, O. M., Ultrahigh Porosity in Metal-Organic Frameworks. *Science* **2010**, *329*, (5990), 424-428.
38. Serna-Guerrero, R.; Da’na, E.; Sayari, A., New Insights into the Interactions of CO<sub>2</sub> with Amine-Functionalized Silica. *Ind Eng Chem Res* **2008**, *47*, (23), 9406-9412.

39. Finsky, V.; Ma, L.; Alaerts, L.; De Vos, D. E.; Baron, G. V.; Denayer, J. F. M., Separation of CO<sub>2</sub>/CH<sub>4</sub> mixtures with the MIL-53(Al) metal–organic framework. *Microporous Mesoporous Mater.* **2009**, *120*, (3), 221-227.
40. Xu, C.; Hedin, N., Synthesis of microporous organic polymers with high CO<sub>2</sub>-over-N<sub>2</sub> selectivity and CO<sub>2</sub> adsorption. *J. Mater. Chem. A* **2013**, *1*, (10), 3406-3414.
41. El-Kaderi, H. M.; Hunt, J. R.; Mendoza-Cortes, J. L.; Cote, A. P.; Taylor, R. E.; O'Keeffe, M.; Yaghi, O. M., Designed synthesis of 3D covalent organic frameworks. *Science* **2007**, *316*, (5822), 268-72.
42. Uribe-Romo, F. J.; Hunt, J. R.; Furukawa, H.; Klöck, C.; O'Keeffe, M.; Yaghi, O. M., A Crystalline Imine-Linked 3-D Porous Covalent Organic Framework. *J. Am. Chem. Soc.* **2009**, *131*, (13), 4570-4571.
43. Sumida, K.; Rogow, D. L.; Mason, J. A.; McDonald, T. M.; Bloch, E. D.; Herm, Z. R.; Bae, T. H.; Long, J. R., Carbon dioxide capture in metal-organic frameworks. *Chem. Rev.* **2012**, *112*, (2), 724-81.
44. Plaza, M. G.; García, S.; Rubiera, F.; Pis, J. J.; Pevida, C., Post-combustion CO<sub>2</sub> capture with a commercial activated carbon: Comparison of different regeneration strategies. *Chem Eng J* **2010**, *163*, (1–2), 41-47.
45. Li, H.; Eddaoudi, M.; O'Keeffe, M.; Yaghi, O. M., Design and synthesis of an exceptionally stable and highly porous metal-organic framework. *Nature* **1999**, *402*, (6759), 276-279.
46. Rabbani, M. G.; El-Kaderi, H. M., Template-Free Synthesis of a Highly Porous Benzimidazole-Linked Polymer for CO<sub>2</sub> Capture and H<sub>2</sub> Storage. *Chemistry of Materials* **2011**, *23*, (7), 1650-1653.

47. Rabbani, M. G.; Reich, T. E.; Kassab, R. M.; Jackson, K. T.; El-Kaderi, H. M., High CO<sub>2</sub> uptake and selectivity by triptycene-derived benzimidazole-linked polymers. *Chem Commun* **2012**, 48, (8), 1141-1143.
48. Rabbani, M. G.; Sekizkardes, A. K.; El-Kadri, O. M.; Kaafarani, B. R.; El-Kaderi, H. M., Pyrene-directed growth of nanoporous benzimidazole-linked nanofibers and their application to selective CO<sub>2</sub> capture and separation. *Journal of Materials Chemistry* **2012**, 22, (48), 25409-25417.
49. Arab, P.; Rabbani, M. G.; Sekizkardes, A. K.; İslamoğlu, T.; El-Kaderi, H. M., Copper(I)-Catalyzed Synthesis of Nanoporous Azo-Linked Polymers: Impact of Textural Properties on Gas Storage and Selective Carbon Dioxide Capture. *Chem. Mater.* **2014**, 26, (3), 1385-1392.
50. Rabbani, M. G.; El-Kaderi, H. M., Template-Free Synthesis of a Highly Porous Benzimidazole-Linked Polymer for CO<sub>2</sub> Capture and H<sub>2</sub> Storage. *Chem. Mater.* **2011**, 23, (7), 1650-1653.
51. Arab, P.; Rabbani, M. G.; Sekizkardes, A. K.; Islamoglu, T.; El-Kaderi, H. M., Copper(I)-Catalyzed Synthesis of Nanoporous Azo-Linked Polymers: Impact of Textural Properties on Gas Storage and Selective Carbon Dioxide Capture. *Chem. Mater.* **2014**, 26, (3), 1385-1392.
52. Rabbani, M. G.; El-Kaderi, H. M., Synthesis and Characterization of Porous Benzimidazole-Linked Polymers and Their Performance in Small Gas Storage and Selective Uptake. *Chem. Mater.* **2012**, 24, (8), 1511-1517.
53. Dawson, R.; Cooper, A. I.; Adams, D. J., Chemical functionalization strategies for carbon dioxide capture in microporous organic polymers. *Polym Int* **2013**, 62, (3), 345-352.
54. Liebl, M. R.; Senker, J., Microporous Functionalized Triazine-Based Polyimides with High CO<sub>2</sub> Capture Capacity. *Chem. Mater.* **2013**, 25, (6), 970-980.



55. Ghanem, B. S.; Hashem, M.; Harris, K. D. M.; Msayib, K. J.; Xu, M.; Budd, P. M.; Chaukura, N.; Book, D.; Tedds, S.; Walton, A.; McKeown, N. B., Triptycene-Based Polymers of Intrinsic Microporosity: Organic Materials That Can Be Tailored for Gas Adsorption. *Macromolecules* **2010**, *43*, (12), 5287-5294.
56. Chen, Q.; Luo, M.; Hammershøj, P.; Zhou, D.; Han, Y.; Laursen, B. W.; Yan, C.-G.; Han, B.-H., Microporous Polycarbazole with High Specific Surface Area for Gas Storage and Separation. *J. Am. Chem. Soc.* **2012**, *134*, (14), 6084-6087.
57. Rabbani, M. G.; Sekizkardes, A. K.; Kahveci, Z.; Reich, T. E.; Ding, R.; El-Kaderi, H. M., A 2D mesoporous imine-linked covalent organic framework for high pressure gas storage applications. *Chem. - Eur. J.* **2013**, *19*, (10), 3324-3328.
58. Pandey, P.; Katsoulidis, A. P.; Eryazici, I.; Wu, Y.; Kanatzidis, M. G.; Nguyen, S. B. T., Imine-linked microporous polymer organic frameworks. *Chem. Mater.* **2010**, *22*, (17), 4974-4979.
59. Rabbani, M. G.; Sekizkardes, A. K.; El-Kadri, O. M.; Kaafarani, B. R.; El-Kaderi, H. M., Pyrene-directed growth of nanoporous benzimidazole-linked nanofibers and their application to selective CO<sub>2</sub> capture and separation. *J. Mater. Chem.* **2012**, *22*, (48), 25409-25417.
60. Rabbani, M. G.; Reich, T. E.; Kassab, R. M.; Jackson, K. T.; El-Kaderi, H. M., High CO<sub>2</sub> uptake and selectivity by triptycene-derived benzimidazole-linked polymers. *Chem Commun (Camb)* **2012**, *48*, (8), 1141-3.
61. Altarawneh, S.; Behera, S.; Jena, P.; El-Kaderi, H. M., New Insights into carbon dioxide interactions with benzimidazole-linked polymers. *Chem. Commun.* **2014**.
62. Doonan, C. J.; Tranchemontagne, D. J.; Glover, T. G.; Hunt, J. R.; Yaghi, O. M., Exceptional ammonia uptake by a covalent organic framework. *Nat Chem* **2010**, *2*, (3), 235-238.

63. Weber, L.; Werner, V.; Fox, M. A.; Marder, T. B.; Schwedler, S.; Brockhinke, A.; Stammler, H. G.; Neumann, B., Synthetic, structural, photophysical and computational studies of pi-conjugated bis- and tris-1,3,2-benzodiazaboroles and related bis(boryl) dithiophenes. *Dalton transactions* **2009**, (8), 1339-1351.
64. Jakle, F., Lewis acidic organoboron polymers. *Coordin Chem Rev* **2006**, *250*, (9-10), 1107-1121.
65. Matsumi, N.; Kotera, K.; Naka, K.; Chujo, Y., Boration copolymerization between diynes and diisocyanates. Novel alternating copolymerization strategy. *Macromolecules* **1998**, *31*, (9), 3155-3157.
66. Dawson, R.; Stockel, E.; Holst, J. R.; Adams, D. J.; Cooper, A. I., Microporous organic polymers for carbon dioxide capture. *Energy & Environmental Science* **2011**, *4*, (10), 4239-4245.
67. Lu, W.; Sculley, J. P.; Yuan, D.; Krishna, R.; Wei, Z.; Zhou, H.-C., Polyamine-Tethered Porous Polymer Networks for Carbon Dioxide Capture from Flue Gas. *Angew. Chem. Int. Ed.* **2012**, *51*, (30), 7480-7484.
68. Maruyama, S.; Kawanishi, Y., Syntheses and emission properties of novel violet-blue emissive aromatic bis(diazaborole)s. *J. Mater. Chem.* **2002**, *12*, (8), 2245-2249.
69. Space, B.; Belof, J. L.; Stern, A. C.; Eddaoudi, M., On the mechanism of hydrogen storage in a metal-organic framework material. *J Am Chem Soc* **2007**, *129*, (49), 15202-15210.
70. Reich, T. E.; Jackson, K. T.; Li, S.; Jena, P.; El-Kaderi, H. M., Synthesis and characterization of highly porous borazine-linked polymers and their performance in hydrogen storage application. *J. Mater. Chem.* **2011**, *21*, (29), 10629-10632.

71. Jackson, K. T.; Rabbani, M. G.; Reich, T. E.; El-Kaderi, H. M., Synthesis of highly porous borazine-linked polymers and their application to H<sub>2</sub>, CO<sub>2</sub>, and CH<sub>4</sub> storage. *Polym. Chem.* **2011**, *2*, (12), 2775-2777.
72. Kuhn, P.; Antonietti, M.; Thomas, A., Porous, covalent triazine-based frameworks prepared by ionothermal synthesis. *Angew. Chem. Int. Ed.* **2008**, *47*, (18), 3450-3453.
73. Feng, X.; Ding, X.; Jiang, D., Covalent organic frameworks. *Chem. Soc. Rev.* **2012**, *41*, (18), 6010-6022.
74. Uribe-Romo, F. J.; Doonan, C. J.; Furukawa, H.; Oisaki, K.; Yaghi, O. M., Crystalline Covalent Organic Frameworks with Hydrazone Linkages. *Journal of the American Chemical Society* **2011**, *133*, (30), 11478-11481.
75. Jackson, K. T.; Reich, T. E.; El-Kaderi, H. M., Targeted synthesis of a porous borazine-linked covalent organic framework. *Chem. Commun.* **2012**, *48*, (70), 8823-8825.
76. Reich, T. E.; Behera, S.; Jackson, K. T.; Jena, P.; El-Kaderi, H. M., Highly selective CO<sub>2</sub>/CH<sub>4</sub> gas uptake by a halogen-decorated borazine-linked polymer. *J. Mater. Chem.* **2012**, *22*, (27), 13524-13528.
77. Chae, H. K.; Siberio-Perez, D. Y.; Kim, J.; Go, Y.; Eddaoudi, M.; Matzger, A. J.; O'Keeffe, M.; Yaghi, O. M., A route to high surface area, porosity and inclusion of large molecules in crystals. *Nature* **2004**, *427*, (6974), 523-527.
78. Tsui, N. T.; Paraskos, A. J.; Torun, L.; Swager, T. M.; Thomas, E. L., Minimization of Internal Molecular Free Volume: A Mechanism for the Simultaneous Enhancement of Polymer Stiffness, Strength, and Ductility. *Macromolecules* **2006**, *39*, (9), 3350-3358.
79. Chen, C.-F., Novel triptycene-derived hosts: synthesis and their applications in supramolecular chemistry. *Chem. Commun.* **2011**, *47*, (6), 1674-1688.

80. Mastalerz, M.; Schneider, M. W.; Oppel, I. M.; Presly, O., A Salicylbisimine Cage Compound with High Surface Area and Selective CO<sub>2</sub>/CH<sub>4</sub> Adsorption. *Angew. Chem. Int. Ed.* **2011**, *50*, (5), 1046-1051.
81. Chong, J. H.; Ardakani, S. J.; Smith, K. J.; MacLachlan, M. J., Triptycene-Based Metal Salphens—Exploiting Intrinsic Molecular Porosity for Gas Storage. *Chem. Eur. J.* **2009**, *15*, (44), 11824-11828.
82. Vagin, S. I.; Ott, A. K.; Hoffmann, S. D.; Lanzinger, D.; Rieger, B., Synthesis and Properties of (Triptycenedicarboxylato)zinc Coordination Networks. *Chem. Eur. J.* **2009**, *15*, (23), 5845-5853.
83. Rabbani, M. G.; El-Kaderi, H. M., Synthesis and Characterization of Porous Benzimidazole-Linked Polymers and Their Performance in Small Gas Storage and Selective Uptake. *Chem Mater* **2012**, *24*, (8), 1511-1517.
84. Hilton, C. L.; Jamison, C. R.; Zane, H. K.; King, B. T., A Triphenylene-Based Triptycene with Large Free Volume Synthesized by Zirconium-Mediated Biphenylation. *The Journal of organic chemistry* **2009**, *74*, (1), 405-407.
85. Zhu, X.-Z.; Chen, C.-F., A Highly Efficient Approach to [4]Pseudocatenanes by Threefold Metathesis Reactions of a Triptycene-Based Tris[2]pseudorotaxane. *J. Am. Chem. Soc.* **2005**, *127*, (38), 13158-13159.
86. Furukawa, H.; Yaghi, O. M., Storage of Hydrogen, Methane, and Carbon Dioxide in Highly Porous Covalent Organic Frameworks for Clean Energy Applications. *Journal of the American Chemical Society* **2009**, *131*, (25), 8875-8883.

87. Rowsell, J. L. C.; Yaghi, O. M., Effects of Functionalization, Catenation, and Variation of the Metal Oxide and Organic Linking Units on the Low-Pressure Hydrogen Adsorption Properties of Metal–Organic Frameworks. *J. Am. Chem. Soc.* **2006**, *128*, (4), 1304-1315.
88. Mastalerz, M.; Oppel, I. M., Rational Construction of an Extrinsic Porous Molecular Crystal with an Extraordinary High Specific Surface Area. *Angew. Chem. Int. Ed.* **2012**, *51*, (21), 5252-5255.
89. Furukawa, H.; Yaghi, O. M., Storage of Hydrogen, Methane, and Carbon Dioxide in Highly Porous Covalent Organic Frameworks for Clean Energy Applications. *Journal of the American Chemical Society* **2009**, *131*, (25), 8875-8883.
90. Reich, T. E.; Behera, S.; Jackson, K. T.; Jena, P.; El-Kaderi, H. M., Highly selective CO<sub>2</sub>/CH<sub>4</sub> gas uptake by a halogen-decorated borazine-linked polymer. *Journal of Materials Chemistry* **2012**, *22*, (27), 13524-13528.
91. Zhao, X. B.; Villar-Rodil, S.; Fletcher, A. J.; Thomas, K. M., Kinetic isotope effect for H-2 and D-2 quantum molecular sieving in adsorption/desorption on porous carbon materials. *J Phys Chem B* **2006**, *110*, (20), 9947-9955.
92. Accelrys, I. M. S. V. A., Inc San Diego, CA, , **2003**.
93. Rietveld, H. M., Line profiles of neutron powder-diffraction peaks for structure refinement. *Acta Cryst.* **1967**, *22*, 151-152.
94. Reticular Chemistry Structure Resource (RCSR), h. r. a. e. a.
95. Coutts, I. G. C.; Goldschm.Hr; Musgrave, O. C., Organoboron Compounds .8. Aliphatic and Aromatic Diboronic Acids. *J Chem Soc C* **1970**, (3), 488-&.
96. Morgan, A. B.; Jurs, J. L.; Tour, J. M., Synthesis, flame-retardancy testing, and preliminary mechanism studies of nonhalogenated aromatic boronic acids: A new class of condensed-phase

polymer flame-retardant additives for acrylonitrile-butadiene-styrene and polycarbonate. *Journal of Applied Polymer Science* **2000**, 76, (8), 1257-1268.

97. Doerksen, R. J.; Thakkar, A. J., Structures, Vibrational Frequencies and Polarizabilities of Diazaborinines, Triazadiborinines, Azaboroles, and Oxazaboroles. *The Journal of Physical Chemistry A* **1999**, 103, (13), 2141-2151.

98. Yamaguchi, I.; Tominaga, T.; Sato, M., Pd-complex-catalyzed synthesis of oligomers having a recurring benzodiazaborole unit in the main chain. *Polym Int* **2009**, 58, (1), 17-21.

99. Paetzold, P. I., Beiträge zur Chemie der Bor-Azide. IV. Mechanismus des thermischen Zerfalls von Diphenylborazid-Pyridin. *Z Anorg Allg Chem* **1963**, 326, (1-2), 64-69.

100. Jaschke, T.; Jansen, M., A new borazine-type single source precursor for Si/B/N/C ceramics. *J. Mater. Chem.* **2006**, 16, (27), 2792-2799.

101. Pandey, P.; Katsoulidis, A. P.; Eryazici, I.; Wu, Y.; Kanatzidis, M. G.; Nguyen, S. T., Imine-Linked Microporous Polymer Organic Frameworks. *Chem. Mater.* **2010**, 22, (17), 4974-4979.

102. Wang, Z.; Zhang, B.; Yu, H.; Sun, L.; Jiao, C.; Liu, W., Microporous polyimide networks with large surface areas and their hydrogen storage properties. *Chem. Commun.* **2010**, 46, (41), 7730-7732.

103. Farha, O. K.; Spokoyny, A. M.; Hauser, B. G.; Bae, Y.-S.; Brown, S. E.; Snurr, R. Q.; Mirkin, C. A.; Hupp, J. T., Synthesis, Properties, and Gas Separation Studies of a Robust Diimide-Based Microporous Organic Polymer. *Chem. Mater.* **2009**, 21, (14), 3033-3035.

104. Farha, O. K.; Bae, Y.-S.; Hauser, B. G.; Spokoyny, A. M.; Snurr, R. Q.; Mirkin, C. A.; Hupp, J. T., Chemical reduction of a diimide based porous polymer for selective uptake of carbon dioxide versus methane. *Chem. Commun.* **2010**, 46, (7), 1056-1058.

105. Dawson, R.; Adams, D. J.; Cooper, A. I., Chemical tuning of CO<sub>2</sub> sorption in robust nanoporous organic polymers. *Chem Sci* **2011**, *2*, (6), 1173-1177.
106. Kahveci, Z.; Islamoglu, T.; Shar, G. A.; Ding, R.; El-Kaderi, H. M., Targeted synthesis of a mesoporous triptycene-derived covalent organic framework. *CrystEngComm* **2013**, *15*, (8), 1524-1527.
107. An, J.; Geib, S. J.; Rosi, N. L., High and Selective CO<sub>2</sub> Uptake in a Cobalt Adeninate Metal–Organic Framework Exhibiting Pyrimidine- and Amino-Decorated Pores. *J. Am. Chem. Soc.* **2009**, *132*, (1), 38-39.
108. Li, B.; Duan, Y.; Luebke, D.; Morreale, B., Advances in CO<sub>2</sub> capture technology: A patent review. *Applied Energy* **2013**, *102*, (0), 1439-1447.
109. Gasteiger, H. A.; Marković, N. M., Just a Dream—or Future Reality? *Science* **2009**, *324*, (5923), 48-49.
110. Thomas, A.; Kuhn, P.; Weber, J.; Titirici, M.-M.; Antonietti, M., Porous Polymers: Enabling Solutions for Energy Applications. *Macromolecular Rapid Communications* **2009**, *30*, (4-5), 221-236.
111. Mohanty, P.; Kull, L. D.; Landskron, K., Porous covalent electron-rich organonitridic frameworks as highly selective sorbents for methane and carbon dioxide. *Nat. Commun.* **2011**, *2*.
112. Laybourn, A.; Dawson, R.; Clowes, R.; Iggo, J. A.; Cooper, A. I.; Khimyak, Y. Z.; Adams, D. J., Branching out with aminated: microporous organic polymers from difunctional monomers. *Polym. Chem.* **2012**, *3*, (2), 533-537.
113. Samanta, A.; Zhao, A.; Shimizu, G. K. H.; Sarkar, P.; Gupta, R., Post-Combustion CO<sub>2</sub> Capture Using Solid Sorbents: A Review. *Ind Eng Chem Res* **2011**, *51*, (4), 1438-1463.

114. Dawson, R.; Stockel, E.; Holst, J. R.; Adams, D. J.; Cooper, A. I., Microporous organic polymers for carbon dioxide capture. *Energy Environ. Sci.* **2011**, *4*, (10), 4239-4245.
115. Ben, T.; Ren, H.; Ma, S.; Cao, D.; Lan, J.; Jing, X.; Wang, W.; Xu, J.; Deng, F.; Simmons, J. M.; Qiu, S.; Zhu, G., Targeted Synthesis of a Porous Aromatic Framework with High Stability and Exceptionally High Surface Area. *Angew. Chem. Int. Ed.* **2009**, *48*, (50), 9457-9460.
116. Lu, W.; Yuan, D.; Zhao, D.; Schilling, C. I.; Plietzsch, O.; Muller, T.; Bräse, S.; Guenther, J.; Blümel, J.; Krishna, R.; Li, Z.; Zhou, H.-C., Porous Polymer Networks: Synthesis, Porosity, and Applications in Gas Storage/Separation. *Chem. Mater.* **2010**, *22*, (21), 5964-5972.
117. Katsoulidis, A. P.; Kanatzidis, M. G., Phloroglucinol Based Microporous Polymeric Organic Frameworks with –OH Functional Groups and High CO<sub>2</sub> Capture Capacity. *Chem. Mater.* **2011**, *23*, (7), 1818-1824.
118. Wilmer, C. E.; Farha, O. K.; Bae, Y.-S.; Hupp, J. T.; Snurr, R. Q., Structure-property relationships of porous materials for carbon dioxide separation and capture. *Energy Environ. Sci.* **2012**, *5*, (12), 9849-9856.
119. Nugent, P.; Belmabkhout, Y.; Burd, S. D.; Cairns, A. J.; Luebke, R.; Forrest, K.; Pham, T.; Ma, S. Q.; Space, B.; Wojtas, L.; Eddaoudi, M.; Zaworotko, M. J., Porous materials with optimal adsorption thermodynamics and kinetics for CO<sub>2</sub> separation. *Nature* **2013**, *495*, (7439), 80-84.
120. Li, P. Z.; Zhao, Y. L., Nitrogen-Rich Porous Adsorbents for CO<sub>2</sub> Capture and Storage. *Chem-Asian J* **2013**, *8*, (8), 1680-1691.
121. Xiang, Z.; Zhou, X.; Zhou, C.; Zhong, S.; He, X.; Qin, C.; Cao, D., Covalent-organic polymers for carbon dioxide capture. *J. Mater. Chem.* **2012**, *22*, (42), 22663-22669.



122. Islamoglu, T.; Gulam Rabbani, M.; El-Kaderi, H. M., Impact of post-synthesis modification of nanoporous organic frameworks on small gas uptake and selective CO<sub>2</sub> capture. *J. Mater. Chem. A* **2013**, *1*, (35), 10259-10266.
123. Furukawa, H.; Yaghi, O. M., *J. Am. Chem. Soc.* **2009**, *131*, 8875.
124. Reich, T. E.; El-Kaderi, H. M., Impact of tailored chemical and textural properties on the performance of nanoporous borazine-linked polymers in small gas uptake and selective binding. *J. Nanopart Res* **2013**, *15*, (1).
125. Zhao, Y.; Yao, K. X.; Teng, B.; Zhang, T.; Han, Y., A perfluorinated covalent triazine-based framework for highly selective and water-tolerant CO<sub>2</sub> capture. *Energy Environ. Sci.* **2013**, *6*, (12), 3684-3692.
126. Deria, P.; Mondloch, J. E.; Tylianakis, E.; Ghosh, P.; Bury, W.; Snurr, R. Q.; Hupp, J. T.; Farha, O. K., Perfluoroalkane Functionalization of NU-1000 via Solvent-Assisted Ligand Incorporation: Synthesis and CO<sub>2</sub> Adsorption Studies. *J. Am. Chem. Soc.* **2013**, *135*, (45), 16801-16804.
127. Bae, Y.-S.; Farha, O. K.; Hupp, J. T.; Snurr, R. Q., Enhancement of CO<sub>2</sub>/N<sub>2</sub> selectivity in a metal-organic framework by cavity modification. *J. Mater. Chem.* **2009**, *19*, (15), 2131-2134.
128. Yang, Z.-Z.; Zhao, Y.; Zhang, H.; Yu, B.; Ma, Z.; Ji, G.; Liu, Z., Fluorinated microporous organic polymers: design and applications in CO<sub>2</sub> adsorption and conversion. *Chem. Commun.* **2014**, *50*, (90), 13910-13913.
129. Zhang, D.-S.; Chang, Z.; Li, Y.-F.; Jiang, Z.-Y.; Xuan, Z.-H.; Zhang, Y.-H.; Li, J.-R.; Chen, Q.; Hu, T.-L.; Bu, X.-H., Fluorous Metal-Organic Frameworks with Enhanced Stability and High H<sub>2</sub>/CO<sub>2</sub> Storage Capacities. *Sci. Rep.* **2013**, *3*, 3312-3318.

130. Xue, D.-X.; Cairns, A. J.; Belmabkhout, Y.; Wojtas, L.; Liu, Y.; Alkordi, M. H.; Eddaoudi, M., Tunable Rare-Earth fcu-MOFs: A Platform for Systematic Enhancement of CO<sub>2</sub> Adsorption Energetics and Uptake. *J. Am. Chem. Soc.* **2013**, *135*, (20), 7660-7667.
131. Bloch, E. D.; Britt, D.; Lee, C.; Doonan, C. J.; Uribe-Romo, F. J.; Furukawa, H.; Long, J. R.; Yaghi, O. M., Metal Insertion in a Microporous Metal–Organic Framework Lined with 2,2'-Bipyridine. *J. Am. Chem. Soc.* **2010**, *132*, (41), 14382-14384.
132. Nugent, P.; Belmabkhout, Y.; Burd, S. D.; Cairns, A. J.; Luebke, R.; Forrest, K.; Pham, T.; Ma, S.; Space, B.; Wojtas, L.; Eddaoudi, M.; Zaworotko, M. J., Porous materials with optimal adsorption thermodynamics and kinetics for CO<sub>2</sub> separation. *Nature* **2013**, *495*, (7439), 80-84.
133. Altarawneh, S.; Nahar, L.; Arachchige, I. U.; El-Ballouli, A. a. O.; Hallal, K. M.; Kaafarani, B. R.; Rabbani, M. G.; Arvapally, R. K.; El-Kaderi, H. M., Highly porous and photoluminescent pyrene-quinoxaline-derived benzimidazole-linked polymers. *J. Mater. Chem. A* **2015**, *3*, (6), 3006-3010.
134. Levine, D. R.; Siegler, M. A.; Tovar, J. D., Thiophene-Fused Borepins As Directly Functionalizable Boron-Containing  $\pi$ -Electron Systems. *Journal of the American Chemical Society* **2014**, *136*, (19), 7132-7139.
135. Hu, R.; Feng, J.; Hu, D.; Wang, S.; Li, S.; Li, Y.; Yang, G., A Rapid Aqueous Fluoride Ion Sensor with Dual Output Modes. *Angewandte Chemie International Edition* **2010**, *49*, (29), 4915-4918.
136. Ke, B.; Chen, W.; Ni, N.; Cheng, Y.; Dai, C.; Dinh, H.; Wang, B., A fluorescent probe for rapid aqueous fluoride detection and cell imaging. *Chemical Communications* **2013**, *49*, (25), 2494-2496.

**Vita**  
Zafer Kahveci  
Department of Chemistry  
Virginia Commonwealth University  
1001 W. Main St.  
Richmond, VA 23284-2006  
Tel.: +1 (804) 503-8534  
E-mail: kahveciz@vcu.edu

### Professional Preparation

Hacettepe University (Turkey)	Chemistry	B.Sc., 2008
Virginia Commonwealth University, VA	Materials Chemistry	Ph.D. Candidate, 2011

### Appointments

Teaching Assistant: Department of Chemistry, Virginia C. University	01/2011-05/2012
Research Assistant: Department of Chemistry, Virginia C. University	05/2012-current

### Research Interest

Polymer science, Porous polymers, MOFs, Gas separation, Gas storage, Renewable energy

### Publications

- Sekizkardes, A. K.; Altarawneh, S.; Islamoglu T.; **Kahveci Z.**; El-Kaderi H. M. “Highly Selective CO<sub>2</sub> capture by Triazine-Based Benzimidazole-Linked Polymers” *Macromolecules*, DOI: 10.1021/ma502071w
- Sekizkardes, A. K.; Islamoglu T.; **Kahveci Z.**; El-Kaderi H. M.” Application of Pyrene-Derived Benzimidazole-Linked Polymers to CO<sub>2</sub> Separation under Pressure and Vacuum Swing Adsorption Settings” *J. Mater. Chem.* 2014, 2, 12492.
- Rabbani, M. G.; Sekizkardes, A. K.; **Kahveci, Z.**; Reich, T. E.; Ding, R.; El-Kaderi H. M. “A 2D Mesoporous Imine-Linked Covalent Organic Framework for High Pressure Gas Storage Application,” *J. Chem. Eur. J.* 2013, 19, 3324.
- **Kahveci, Z.**; Islamoglu, T.; Shar, G.A.; Ding R.; and El-Kaderi, H. M.\* “Targeted Synthesis of A Mesoporous Triptycene-Derived Covalent Organic Frameworks” *CrystEngComm* 2013.
- **Kahveci Z.**; Sekizkardes, A. K.; El-Kaderi H. M.” Synthesis and Characterization of Highly Porous Diazaborole Link Polymers” *in preparation*
- **Kahveci Z.**; Arvapally, R. ; El-Kaderi H. M. “Post-synthesis modification of diazaborole-linked polymers for enhanced chemical stability and CO<sub>2</sub> capture” *in preparation*

- Demir M., **Kahveci Z.**, Aksoy B., Palapati N., Subramanian A., Cullinan H.T., Hani M. El-Kaderi H. M. and Gupta R. B.” Graphitic bio-carbon from metal-catalyzed hydrothermal carbonization of lignin” (*Submitted*)

### Selected Oral Presentations

- **Kahveci, Zafer;** El-Kaderi H. M.\* “Synthesis and Characterization of Highly Porous Diazaborole Link Polymers” 248<sup>th</sup> National Meeting of the American Chemical Society. August 10-14, 2014, San Francisco, CA, Division of Energy and Fuels.
- Sekizkardes, A. K.; Altarawneh, S.; Islamoglu T.; **Kahveci Z.**; El-Kaderi H. M. “Highly Selective CO<sub>2</sub> capture by Triazine-Based Benzimidazole-Linked Polymers” ACS CERM, Pittsburg, PA, October 2014.
- **Kahveci, Zafer;** El-Kaderi H. M.\* “Li-Air Batteries Types, Applications, and Challenges” Virginia Commonwealth University, October 2013.

### Selected Poster Presentations

- Sekizkardes, A. K.; Arab, P.; Alyson V.; **Kahveci Z.**; El-Kaderi H. M. “Exceptionally Porous Covalent Organic Frameworks As Catalyst Support for Use in Heterogeneous Catalysis” SCU, Columbia, SC, June 2014.
- Sekizkardes, A. K.; Rabbani, M. G.; **Kahveci Z.**; El-Kaderi H. M. “Selective Gas Uptake and Storage in Porous Organic Framework” 246<sup>th</sup> ACS Meeting Indianapolis, September 2013.
- **Kahveci, Z.**; Rabbani, M. G.; Sekizkardes, A. K.; El-Kaderi H. M. “Synthesis of Diazaborole-Linked Porous Organic Polymers” Virginia Commonwealth University (Richmond, VA), October 2011.
- **Kahveci, Z.**; El-Kaderi H. M. “Triptycene Derived Covalent organic frameworks: designed synthesis and application to gas storage” Virginia Commonwealth University (Richmond, VA), October 2012.

### Expertise

Synthesis and characterization of porous organic polymers (POPs)

Boronic acid-condensation polymerization

Materials Studio (Forcite) and building porous structures

Crystal Maker

Air-free synthesis technique (Schlenk line, Glove box)

Schiff-base imine-condensation polymerization

Scanning electron microscope (SEM)

X-ray diffraction (XRD)

Low-pressure gas analyzer (Quanta chrome 1C and IQ2)  
High-pressure volumetric analysis (HPVA)  
Fourier transform infrared spectroscopy (FT-IR)  
Nuclear magnetic resonance (NMR)

### **Awards, Scholarships, and Honors**

2011 Teaching and Research Assistant Scholarship at Virginia Commonwealth University  
2012 VCU Chemistry Department Kapp Award  
2013 Commonwealth Graduate Studies Award

### **Graduate Advisor**

Ph.D. Advisor: Associate Prof. Hani M. El-Kaderi, Virginia Commonwealth University, Richmond, VA

### **PERSONAL AFFILIATIONS**

American Chemical Society